HOMOGENIZATION OF COMPOSITE MATERIALS WITH NON-ELLIPSOIDAL INHOMOGENEITIES USING THE PROPERTY CONTRIBUTION TENSOR APPROACH

BY

ANTON SERGEYEVICH TROFIMOV, M.S.

A dissertation submitted to the Graduate School

in partial fulfillment of the requirements

for the degree

Doctor of Philosophy, Engineering

Specialization in Mechanical Engineering

New Mexico State University

Las Cruces, New Mexico

May 2017

"Homogenization of Composite Materials with Non-Ellipsoidal Inhomogeneities using the Property Contribution Tensor Approach," a dissertation prepared by Anton Sergeyevich Trofimov in partial fulfillment of the requirements for the degree Doctor of Philosophy, Engineering, has been approved and accepted by the following:

_____

Loui Reyes
Dean of the Graduate School

_____

Borys Drach
Chair of the Examining Committee

_____

Date

Committee in charge:

     Dr. Borys Drach, Chair

     Dr. Douglas D. Cortes

     Dr. Igor Sevostianov

     Dr. Krishna Kota Venekata

DEDICATION

I dedicate this work to my dear parents Sergey Leonidovich Trofimov and Larisa Georgiyevna Trofimova who have always been supportive and filled my life far away from home with love. I dedicate this work to my lovely wife Kseniia Trofimova who has always stayed on my side, kept patience and sacrificed her career to be with me. I also want to dedicate this work to my sister Anna Trofimova and my grandmothers Ekaterina Alekseevna Trofimova and Valentina Markovna Spiridonova who supported my education from the very beginning of my life.

VITA

October 3, 1990	Born in Moscow, Russia
2007	Graduated from Gymnasium No. 470, Saint Petersburg, Russia
2011	B.S. in Applied Mechanics, Saint Petersburg State Polytechnic University, Saint Petersburg, Russia
2013	M.S. in Applied Physics, Saint Petersburg State Polytechnic University, Saint Petersburg, Russia
2016	M.S. in Mechanical Engineering, New Mexico State University, Las Cruces, New Mexico
2013-2017	Research and Teaching Assistant, Department of Mechanical and Aerospace Engineering, New Mexico State University, Las Cruces, New Mexico

PUBLICATIONS

B.Drach, A.Drach, I.Tsukrov, A.Trofimov, 2017. "Modeling of progressive damage during cooling after curing of 3D woven composites". Composite Structures

A.Trofimov, B.Drach, I.Sevostianov, 2017. "Effect of polyhedral particle shapes on overall elastic properties of particle-reinforced composites". International Journal of Solids and Structures, Submitted

A.Trofimov, B.Drach, M.Kachanov, I.Sevostianov, 2017. "Effect of a partial contact between the crack faces on its contribution to overall material compliance and resistivity", International Journal of Solids and Structures 108, 289–297. DOI: 10.1016/j.ijsolstr.2016.12.028

B.Drach, I.Tsukrov, A.Trofimov, 2016. "Comparison of full field and single pore approaches to homogenization of linearly elastic materials with pores of regular and irregular shapes", International Journal of Solids and Structures 96, 48-63. DOI: 10.1016/j.ijsolstr.2016.06.023

I. Tsukrov, B.Drach, A.Trofimov, K. Vasylevskyi, 2016. "Homogenization of Linearly Elastic Materials with Pores of Irregular Shapes via Direct FEA and Single Pore Approaches", Proceedings of the 31st ASC Technical Conference and ASTM D30 meeting, Williamsburg, VA, USA

A.Trofimov, B.Drach, I.Tsukrov, 2015. "Elastic Homogenization via Single Inclusion and Full Field Approaches, and Modeling of Progressive Failure in Porous RTM6 Epoxy", Presentation at the 52nd Annual Technical Meeting of the Society of Engineering Science, Texas A&M University, College Station, TX, USA

I.Tsukrov, B.Drach, A.Trofimov, 2014. "Comparison of Full Field and Single Inclusion Approaches to Homogenization of Composites with Non-Ellipsoidal Pores". Key Engineering Materials (Advances in Fracture and Damage mechanics XIII), 627, 309-312. DOI: 10.4028/www.scientific.net/KEM.627.309

FIELD OF STUDY

Specialization in Mechanical Engineering

ABSTRACT

HOMOGENIZATION OF COMPOSITE MATERIALS WITH NON-
ELLIPSOIDAL INHOMOGENEITIES USING THE PROPERTY
CONTRIBUTION TENSOR APPROACH

BY

ANTON SERGEYEVICH TROFIMOV, M.S.

Doctor of Philosophy, Engineering

Specialization in Mechanical Engineering

New Mexico State University

Las Cruces, New Mexico, 2017

Dr. Borys Drach, Chair

Many composite materials contain inhomogeneities of irregular shapes for which no analytical solutions exist. This thesis focuses on effective properties of composites with irregularly shaped pores, polyhedral inhomogeneities and penny-shaped cracks with "islands" of partial contact. The problem of homogenization is solved using direct finite element analysis of periodic representative volume elements and using non-interaction, Mori-Tanaka and Maxwell micromechanical schemes. A novel efficient numerical procedure is developed to generate and analyze the representative volume elements with volume fraction up to 30% for the former approach. The latter approach utilizes numerical solutions for individual inhomogeneity contribution tensors in micromechanical schemes. It is observed that

Mori-Tanka and Maxwell approximations are in good correspondence with the direct finite element results in the cases of materials containing inhomogeneities of the same shape as well as mixtures of different shapes.

Stiffness and compliance contribution tensors of the considered polyhedral shapes are presented for the first time. Ways of extending the results beyond the material combinations used in this thesis are discussed in terms of applicability of the replacement relations and the semi-empirical relations addressing the effect of matrix Poisson's ratio. In addition, analytical solutions for compliance and resistivity tensors of penny-shaped cracks with islands of partial contact are given. For the cases of materials with multiple cracks, an approach to calculation of the adjusted crack density parameter is proposed. With this parameter, all available schemes for the effective elastic properties of cracked solids as functions of crack density can be applied to penny-shaped cracks with islands.

TABLE OF CONTENTS

LIST OF TABLES

LIST OF FIGURES

1.0   INTRODUCTION

The problem of the effective properties of heterogeneous materials plays a key role in material characterization. The ability to predict overall material properties provides the tools for analysis of both naturally occurring and man-made materials, which supports the growing needs in Materials Science. This problem was first considered in the nineteenth century by Maxwell (1873) and received a significant attention in the twentieth century after the important works of Hill (1952, 1963), Eshelby (1957, 1959, 1961), Kröner (1958), Hashin and Shtrikman (1963) and Walpole (1969), who built the foundation for quantitative modeling of effective properties of heterogeneous media. In this chapter, the basic principles of modeling of the overall properties of microstructures containing inhomogenities are presented.

In heterogeneous materials, effective properties are the constants that interrelate volume averages of the microscale physical fields (e.g. stress, strain, temperature and heat flux). These constants can be found using the homogenization procedure based on the concept of Representative Volume Element (RVE, Hill (1963)). RVE of a composite is a volume large enough to be statistically representative of the material, i.e. contain a representative sampling of all microstructural inhomogeneities present in the composite. A commonly accepted criterion to control the size of RVE is Hill's condition (Hill, 1963)) that requires homogeneous boundary conditions

$$\langle \boldsymbol{\sigma} : \boldsymbol{\varepsilon} \rangle = \langle \boldsymbol{\sigma} \rangle : \langle \boldsymbol{\varepsilon} \rangle, \tag{1}$$

1

where $\boldsymbol{\sigma}$ and $\boldsymbol{\varepsilon}$ are stresses and strains, $\langle...\rangle$ denotes averaging over the RVE of volume V. In the case of elastic properties, boundary conditions in displacements $\mathbf{u}|_{\partial V} = \boldsymbol{\varepsilon}^0 \cdot \mathbf{x}$ or tractions $\mathbf{t}|_{\partial V} = \boldsymbol{\sigma}^0 \cdot \mathbf{n}$ corresponding to the remotely applied strain $\boldsymbol{\varepsilon}^0$ and stress $\boldsymbol{\sigma}^0$ fields satisfy Hill's condition. In these expressions, ∂V is the boundary of the RVE, $\mathbf{x}$ is the position-vector of a point on the RVE boundary and $\mathbf{n}$ is the outward unit normal on ∂V. Similar considerations apply to other physical properties, such as thermal, in case of which homogeneous boundary conditions can be applied in terms of temperatures or heat flux. Periodic boundary conditions automatically satisfy Hill's condition. Thus, a properly chosen RVE and correctly applied boundary conditions are two important initial steps in the problem of effective properties of the heterogeneous materials.

Another essential concept in characterization of the overall material properties is identification of the microstructure parameters. Microstructure parameters must adequately represent individual inhomogeneities in accordance with their actual contributions to the physical property of interest (volumes, shapes, and orientations). Volume fraction is one of the most widely used parameter. It was introduced for the case of identical ellipsoidal inhomogeneities by Hill (1965). However, this parameter is not always the most appropriate choice. For example, following the review in (Sevostianov and Kachanov (2013), in the case of a material with multiple cracks, the crack density parameter $\rho = (1/V) \sum a^{(k)3}$ introduced by Bristow (1960) relates the

2

contribution of k-th crack with its radius cubed and does not depend on crack aspect ratio γ ($\gamma < 0.1$).

For materials containing inhomogeneities, which are the subject of this dissertation, effective properties can be expressed in terms of the property contribution tensors of an individual inhomogeneity. Such tensors were first introduced in the context of contributions of pores and cracks to elastic properties by Horii and Nemat-Nasser (1983).

In the context of effective elastic properties, we consider a volume V containing matrix material and an isolated inhomogeneity of volume V_1 and subjected to uniform traction boundary conditions on ∂V: $\mathbf{t}|_{\partial V} = \boldsymbol{\sigma}^0 \cdot \mathbf{n}$. Following the works of Kachanov et al. (1994), Sevostianov and Kachanov (2002), Tsukrov and Novak (2002), Kachanov et al. (2003), Eroshkin and Tsukrov (2005) the volume-averaged strain can be represented as follows

$$\langle \boldsymbol{\varepsilon} \rangle = \mathbf{S}^0 : \boldsymbol{\sigma}^0 + \Delta \boldsymbol{\varepsilon}, \tag{2}$$

where $\mathbf{S}^0$ is the compliance tensor of the matrix. Since the material is assumed to be linearly elastic, the extra strain due to the inhomogeneity $\Delta \boldsymbol{\varepsilon}$ can be expressed as a function of $\boldsymbol{\sigma}^0$:

$$\Delta \boldsymbol{\varepsilon} = \frac{V_1}{V} \mathbf{H} : \boldsymbol{\sigma}^0, \tag{3}$$

where $\mathbf{H}$ is the fourth-rank compliance contribution tensor of the inhomogeneity normalized by its volume fraction. Alternatively, following Sevostianov and Kachanov

3

(1999) one can consider a volume subjected to displacement boundary conditions on ∂V $\mathbf{u}|_{\partial V} = \boldsymbol{\varepsilon}^0 \cdot \mathbf{x}$. In that case, the volume-averaged stress can be represented as a sum:

$$\langle \boldsymbol{\sigma} \rangle = \mathbf{C}^0 : \boldsymbol{\varepsilon}^0 + \Delta \boldsymbol{\sigma}, \tag{4}$$

where $\mathbf{C}^0$ is the stiffness tensor of the matrix. The extra stress due to the presence of the inhomogeneity can be expressed as follows:

$$\Delta \boldsymbol{\sigma} = \frac{V_1}{V} \mathbf{N} : \boldsymbol{\varepsilon}^0, \tag{5}$$

where $\mathbf{N}$ is the fourth-rank stiffness contribution tensor of the inhomogeneity normalized by its volume fraction. The tensor characterizes the far-field asymptotic of the elastic fields generated by the inhomogeneity and determines its contribution to the effective elastic properties Igor Sevostianov and Kachanov (2011).

Similarly, in the context of conductivity (thermal or electric), analogues of the $\mathbf{H}$ and $\mathbf{N}$ tensors are the resistivity $\mathbf{R}$ and conductivity $\mathbf{K}$ contribution tensors. For instance, let us consider a thermal conductivity problem with uniform temperature boundary conditions applied to the external surfaces of a volume V containing an inhomogeneity of volume V_1. Following the Fourier's law of heat conduction, the volume-averaged heat flux can be represented as follows:

$$\langle \mathbf{U} \rangle = -k^0 \cdot \mathbf{G}^0 + \Delta \mathbf{U}, \tag{6}$$

where k^0 is the matrix conductivity and $\mathbf{G}^0$ is the prescribed temperature gradient. Extra heat flux $\Delta \mathbf{U}$ due to the presence of the inhomogeneity can be written as a function of $\mathbf{G}^0$:

$$\Delta \mathbf{U} = \frac{V}{V_1} \mathbf{K} \cdot \mathbf{G^0}, \tag{7}$$

where contribution tensor $\mathbf{K}$ interrelates extra heat flux $\Delta \mathbf{U}$ and applied uniform temperature gradient $\mathbf{G^0}$. Alternatively, this relation can be written in a dual form, where resistivity $\mathbf{R}$ contribution tensor interrelates extra temperature gradient $\Delta \mathbf{G}$ due to the presence of the inhomogeneity and applied uniform heat flux $\mathbf{U^0}$:

$$\Delta \mathbf{G} = \frac{V}{V_1} \mathbf{R} \cdot \mathbf{U^0}. \tag{8}$$

Thus, to evaluate the contribution of an inhomogeneity to the overall response of a material, the corresponding individual property contribution tensor needs to be defined. The tensor can be calculated analytically (in some special cases) or numerically. The analytical approach is traditionally described in the framework of the classic theory of Eshelby (1957, 1961), assuming that the inhomogeneity is ellipsoidal. According to the solutions provided in Kunin and Sosnina (1971) and Sevostianov and Kachanov (2002), the inhomogeneity stiffness $\mathbf{N}$ and compliance $\mathbf{H}$ contribution tensors can be calculated as follows:

$$\mathbf{N} = \frac{V}{V_1} [(\mathbf{C^1} - \mathbf{C^0})^{-1} + \mathbf{P}]^{-1},$$

$$\mathbf{H} = \frac{V}{V_1} [(\mathbf{S^1} - \mathbf{S^0})^{-1} + \mathbf{Q}]^{-1}, \tag{9}$$

where tensors $\mathbf{C^1}$ and $\mathbf{S^1}$ are stiffness and compliance tensors of inhomogeneity correspondingly, and tensors $\mathbf{P}$ and $\mathbf{Q}$ can be expressed in terms of Eshelby's tensor $\mathbf{s}$:

$$\mathbf{P} = \mathbf{s} : \mathbf{S^0},$$

$$\mathbf{Q} = \mathbf{C^0} : (\mathbf{J} - \mathbf{S}), \tag{10}$$

5

where **J** is the fourth rank unit tensor. The components of **s** are expressed in terms of elliptical integrals; in the special case of a spheroidal inclusion, representation in terms of elementary functions is available.

In the case of "irregular" (non-ellipsoidal) shapes, only a limited number of analytical solutions are available due to the complexity of the boundary value problem. Most of the results have been obtained for 2-D shapes using complex variable approach. Zimmerman (1986) discussed the compressibility of 2-D solids containing pores of various shape. Jasiuk et al. (1994) considered the effect of polygonal pores on the elastic moduli. Kachanov et al. (1994) considered a more general case that includes 2-D pores of both concave and convex shapes. Jasiuk (1995) compared the effects of polygonal pores and rigid inhomogeneities on the effective elastic properties. General cases of pores and inhomogeneities of arbitrary 2-D shapes were discussed in two works of Tsukrov and Novak (2002, 2004). In 3-D, some results have been obtained for cracks of irregular shapes (see Section 8 of the review in Sevostianov and Kachanov, 2013). The toroidal shape was studied by Argatov and Sevostianov (2011) who approximated the contribution of a thin rigid toroidal inhomogeneity to the overall stiffness. The problem of the effective conductivity (thermal or electric) of a material containing toroidal insulating inhomogeneities was addressed by Radi and Sevostianov (2016). Garboczi & Douglas (2012) developed numerical approximations for intrinsic bulk and shear moduli in the case of randomly oriented block-like particles based on finite element calculations and corrected analytical solution for an ellipsoid.

6

Only numerical results exist for other 3-D shapes. Drach et al. (2011) used finite element calculations to obtain the compliance contribution tensors for several 3-D pores of irregular shapes typical for carbon-carbon composites. Drach et al. (2014) used response surface methodology to derive a statistical model correlating geometric parameters of pores with their compliance contribution tensor components. Rasool and Böhm (2012) analyzed the effects of spherical, cubic, tetrahedral and octahedral particle shapes on the effective thermoelastic properties of materials with matrix-inclusion topology. Concave superspherical pores were discussed in Sevostianov et al. (2008) who used finite element analysis and in Sevostianov and Giraud (2012) who gave an analytical approximation of the numerical results. Chen et al. (2015) corrected some inaccuracies in these papers and showed the dependence of the compliance contribution tensor of a superspherical pore on the concavity parameter p. Another concave shape – supersphere of revolution – was considered by Sevostianov et al (2016).

Two types of homogenization approaches are used to predict effective properties of the materials containing multiple inhomogeneities – direct finite element analysis (FEA) simulations of RVEs and micromechanical modeling based on the solutions for individual inhomogeneities. The simplest micromechanical scheme is the non-interaction approximation (NIA), in which inhomogeneities are treated as isolated ones and interactions with neighbors are neglected. In this case, the property contribution tensor of the RVE containing multiple inhomogeneities is obtained by

7

direct summation of the individual property contribution tensors. Most of the other schemes are based on the NIA − the non-interacting inhomogeneities are assumed to be placed into some sort of effective environment (effective matrix or effective field).

In this work, we address the problem for which only a limited number of solutions exist − estimation of effective properties of materials containing 3-D irregularly shaped inhomogeneities. Two approaches are studied − direct FEA simulations and homogenization using several commonly used micromechanical schemes. For the direct FEA approach, a novel numerical procedure for generation of periodic RVEs containing arrangements of irregular shapes is presented in Chapter 2. In the same chapter, compliance contribution tensors of individual regular and irregular pores are obtained and used to approximate effective elastic properties of porous materials with different volume fractions via micromechanical modeling. Stiffness contribution tensors of polyhedral inhomogeneities are calculated and effective elastic properties of materials with polyhedral particles are estimated using direct FEA and micromechanical approaches in Chapter 3. Compliance and resistivity contribution tensors of a penny-shaped crack having a partial area of contact are calculated numerically and approximated analytically in Chapter 4. The implications for multiple cracks are also discussed. Conclusions of the research and suggestions for future work are given in Chapter 5.

2.0 HOMOGENIZATION OF LINEARLY ELASTIC MATERIALS WITH PORES OF REGULAR AND IRREGULAR SHAPES

Abstract. Two approaches to predict the overall elastic properties of solids with regularly and irregularly shaped pores are compared. The first approach involves direct finite element simulations of periodic representative volume elements containing arrangements of pores. A simplified algorithm of collective rearrangement type is developed for generating microstructures with the desired density of randomly distributed pores of regular and irregular shapes. Homogeneity and isotropy (where appropriate) of the microstructures are confirmed by generating two-point statistics functions. The second approach utilizes Mori-Tanaka and Maxwell micromechanical models implemented via the cavity compliance contribution tensor (**H**-tensor) formalism. The effects of pore shape and matrix Poisson's ratio on compliance contribution parameters of different shapes are discussed. H-tensors of cubical, octahedral and tetrahedral pores for several values of matrix Poisson's ratio are published in explicit form for the first time. Good correspondence between the direct finite element simulations and micromechanical homogenization is observed for randomly oriented and parallel pores of the same shape, as well as mixtures of pores of various shapes up to 25% pore volume fractions.

2.1 Introduction

For many applications it is important to be able to determine how defects, and in particular pores, reduce the effective elastic properties of materials. There are several

approaches to homogenization of porous solids including direct finite element analysis (FEA) simulations of representative volume elements (RVEs) of the material, micromechanical modeling schemes based on the solutions for individual defects, and establishment of variational bounds of Hashin-Shtrikman type, see, for example, discussion in Böhm et al. (2004). However, most of the existing literature is limited to the ellipsoidal shapes of defects since these shapes allow for convenient analytical solutions provided by Eshelby (1957, 1959). Meanwhile non-ellipsoidal pores are not only present in many natural and man-made materials (see examples in Sevostianov and Kachanov (2012)) but are also considered in design of additively manufactured end use components with deliberately engineered porosity (Choren et al. (2013)).

In this chapter, we describe a numerical procedure to generate and analyze RVEs with non-intersecting pores of regular (ellipsoidal and polyhedral) and irregular shapes. We compare the results of direct FEA simulations with the predictions of two popular micromechanical schemes, Mori-Tanaka (Benveniste (1987); Mori and Tanaka (1973); Weng (1990)) and Maxwell (Maxwell (1873); McCartney and Kelly (2008); Sevostianov (2014)). The approach is illustrated by considering spherical, spheroidal, octahedral, cubical and irregular pore shapes. The latter was selected from microcomputed tomography (μCT) data obtained for a sample of 3D woven carbon/epoxy composite provided by Albany Engineered Composites (Rochester, NH USA). The pore shape is shown in Figure 1.

Most of the published work on comparison of analytical micromechanical models with direct numerical simulations deals with the inhomogeneities of regular

shapes such as spheres, spheroids and long fibers of circular cross-section. (Segurado and Llorca (2002)) numerically generated multiple RVEs with 30 spherical inhomogeneities utilizing the Random Sequential Adsorption (RSA) algorithm (Widom (1966)). They performed numerical simulations using FEA and compared their predictions of the effective elastic properties with several analytical homogenization models. The best correspondence was observed for the third order estimates of Torquato (1998). Later publications of that research group focused on nonlinear (elasto-plastic) behavior of composites with spherical and ellipsoidal inclusions, see for example (González et al. (2004); Pierard et al. (2007)).

Ghossein and Lévesque (2012, 2014) performed a comprehensive comparison of analytical and numerical homogenization results for random composites reinforced by spherical and spheroidal particles. They utilized an efficient, molecular dynamics based algorithm to generate random microstructures reaching significant particle volume fractions (up to volume fraction of 0.74 for monodisperse spheres, which is close to the theoretical limit of hexagonal close packing). The effective elastic properties were computed by applying a technique based on Fast Fourier Transforms (FFT) introduced in Moulinec and Suquet (1994) and Moulinec and Suquet (1998). The technique was shown to produce predictions very close to FEA – less than 1% difference for spherical particle reinforced composite with considered material properties. Note that recent findings by Gusev (2016a) indicate that the FFT-based method requires substantial computational resources for accurate predictions when composites with high material property contrasts are considered. In their two

publications, Ghossein and Lévesque compared popular analytical homogenization schemes with numerical predictions for a wide range of material property contrasts, aspect ratios of the particles and their volume fraction. The authors limited their studies to microstructures with random orientation distribution of inhomogeneities of the same type, so the overall composite properties were isotropic.

El Moumen et al. (2015) addressed the influence of inhomogeneity shape on the effective bulk and shear moduli in the case of simulated microstructures containing randomly oriented non-overlapping particles. The authors focused on stiff particles of spherical and two spheroidal shapes (one oblate and one prolate) and used "multi-phase element" FEA to determine the effective elastic moduli of microstructures containing particles of the same shape. They compared their numerical results with the Hashin-Shtrikman bounds and Generalized Self Consistent scheme. In addition, they investigated the choice of the appropriate size of an RVE as a function of particle shape, material property contrast and volume fraction. The investigation was based on the statistical analysis involving microstructure covariograms and variations of effective properties between random realizations.

For composites with irregularly shaped inhomogeneities, several significant results are available in 2D. The solutions based on conformal mapping were utilized by (Ekneligoda and Zimmerman (2006, 2008); Jasiuk et al. (1994); Kachanovet al. (1994); Mogilevskaya and Nikolskiy (2015); Tsukrov and Novak (2002); Zimmerman (1986, 1991); Zou et al. (2010)). In 3D, (Garboczi and Douglas (2012)) presented a procedure to approximate bulk and shear elastic contribution parameters in the case of randomly

12

oriented inhomogeneities shaped as blocks. The approximation is based on the solution for an ellipsoid with the additional correction factors derived by fitting analytical expressions to tabulated data from FEA results. Good correspondence between FEA results and the proposed approximation was found for a wide range of aspect ratios, matrix/inhomogeneity elastic contrasts and Poisson's ratios.

Rasool and Böhm (2012) analyzed the effects of particle shape on the effective thermoelastic properties of composites reinforced with particles of spherical, cubical, tetrahedral and octahedral shapes. The authors performed FEA on five realizations of periodic structures with 20 particles of the same shape per RVE generated using a variation of RSA algorithm. Their results, however, were limited to a single stiffness contrast of 10 (particles stiffer than the matrix) and a single volume fraction value of 0.2. We compared our predictions obtained using Mori-Tanaka scheme based on the stiffness contribution tensor with the numerical results presented in (Rasool & Böhm, 2012) in a separate study (Böhm, personal communication) and obtained good correspondence (error within 1.2%). Recently, Böhm and Rasool (2016) extended the approach by considering elasto-plastic behavior of the matrix material.

Analytical micromechanical predictions of effective elastic properties are limited by the available elasticity solutions for an inclusion (portion of the matrix material with some prescribed eigenstrain) or inhomogeneity (portion of a different material inserted into the matrix material). In addition to the famous Eshelby solution for ellipsoidal inclusions (Eshelby (1957)), the analytical results for 3D inclusions and inhomogeneities of cubical (Chen and Young (1977); Faivre (1969)), cylindrical (Wu

and Du (1995)), superspherical (Onaka (2001)), toroidal (Onaka et.al, (2002)) and general polyhedral shapes (Nozaki and Taya (2001); Rodin (1996)) have been presented in the literature. However, not all of the solutions obtained for non-ellipsoidal shapes are convenient or appropriate for evaluation of contribution of the inhomogeneities to effective elastic properties. For materials with polyhedral inhomogeneities, the effective stiffness was predicted in (Nozaki and Taya (2001)); for convex superspherical inhomogeneities – in (Hashemi et al. (2009)). Both of these publications utilized analytical solutions in the framework of Mori-Tanaka scheme.

Numerical evaluation of contribution of individual inhomogeneity shapes also provides good basis for micromechanical modeling of effective properties. (Sevostianov et al. (2008); Sevostianov and Giraud (2012)) calculated contributions of superspherical pores; the accuracy of the calculations for concave superspherical pores was later improved by the authors in (Chen et al. (2015)). (Drach et al. (2011); Drach et al. (2014)) used FEA to evaluate compliance contribution tensors for several irregular pore shapes relevant for carbon-carbon and 3D woven carbon-epoxy composites.

In this chapter, we utilize the compliance contribution tensor formalism to produce analytical micromechanical predictions of effective elastic properties as discussed in Section 2.2. Our approach to numerical homogenization using FEA of RVEs with synthetically generated microstructures is presented in Section 2.3. The section also describes how we utilize two-point statistics functions to evaluate the homogeneity and isotropy of the generated microstructures. Predictions of the effective

14

elastic properties for materials with pores of spherical, spheroidal, cubical, octahedral and an irregular shape are provided in Section 2.4. The results obtained by numerical modeling are compared with the estimates given by the Mori-Tanaka and Maxwell micromechanical models. Both parallel and random orientations of defects of the same shape are considered. The applicability of the method to mixtures of defects of different shapes is illustrated by modeling the material with spheroidal and irregularly-shaped pores. We also discuss the effects of shape and matrix Poisson's ratio on the pore compliance contribution parameters of the considered shapes. Section 2.5 presents conclusions from the research. Lastly, all components of the compliance contribution tensors for pores of cubical, octahedral and tetrahedral shapes for several values of matrix Poisson's ratio are provided in Appendix A.
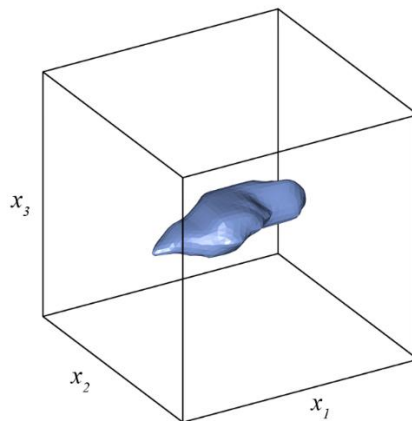
Figure 1. Irregularly shaped pore obtained from μCT of carbon/epoxy composite sample

2.2 Homogenization based on single pore problem

Contribution of an individual pore to the effective material response can be evaluated using the pore compliance contribution tensor – $\mathbf{H}$-tensor, as described in Horii and Nemat-Nasser (1983) and Kachanov et al. (1994), see also (Eroshkin and Tsukrov (2005); Sevostianov et al. (2014); Zohdi (2012)). The effective compliance tensor of the material with pores is presented as

$$\mathbf{S} = \mathbf{S_0} + \mathbf{H_{RVE}}, \tag{11}$$

where $\mathbf{S_0}$ is the compliance tensor of the matrix material and $\mathbf{H_{RVE}}$ is the contribution from all pores present in the representative volume element (RVE). For dilute distribution of pores, the non-interaction approximation can be used, and $\mathbf{H_{RVE}}$ is found by direct summation of contributions from all individual pores in the RVE:

$$\mathbf{H_{RVE}^{NI}} = \sum_i \mathbf{H}_{(i)}, \tag{12}$$

where $\mathbf{H}_{(i)}$ is the compliance contribution tensor of the i-th pore. This tensor is defined as a set of the proportionality coefficients between the additional strain $\Delta\boldsymbol{\varepsilon}$ in a reference volume due to the presence of the pore and the remotely applied stress $\boldsymbol{\sigma}_0$ (see Mark Kachanov et al. (1994)):

$$\Delta\boldsymbol{\varepsilon} = \mathbf{H}_{(i)} : \boldsymbol{\sigma}_0,, \tag{13}$$

where colon denotes contraction over two indices. For higher porosities when the non-interaction approximation is no longer applicable, more advanced micromechanical schemes can be used. One of the most popular first order micromechanical schemes is the Mori-Tanaka scheme, see (Benveniste, 1987b; Mori and Tanaka (1973); Weng

16

(1990). When reformulated in terms of the compliance contribution tensor, this scheme

provides the following simple estimate for tensor H (Kachanov et al. (1994)):

$$\mathbf{H}_{\text{RVE}}^{\text{MT}} = \frac{\mathbf{H}_{\text{RVE}}^{\text{NI}}}{(1-p)},\qquad(14)$$

where p is the volume fraction of pores.

Alternatively, H-tensor of the RVE may be found using Maxwell's

homogenization scheme (Maxwell (1873); McCartney and Kelly (2008); Sevostianov,

(2014)):

$$\mathbf{H}_{\text{RVE}}^{\text{Maxwell}} = \left\{\left[\mathbf{H}_{\text{RVE}}^{\text{NI}}\right]^{-1} - \mathbf{Q}_{\Omega}\right\}^{-1},\qquad(15)$$

where $\mathbf{Q}_{\Omega}$ is Hill's tensor ((Hill, 1965; Walpole, 1969)) for the "effective inclusion" of

shape Ω. In the case of aligned ellipsoidal inhomogeneities of the same shape, the

effective inclusion shape is the same as the shape of the individual ellipsoids. When

the homogenized composite is isotropic, e.g. randomly oriented ellipsoidal

inhomogeneities of the same shape, the effective inclusion is of spherical shape. In all

other cases, the effective inclusion is an ellipsoid with aspect ratios given by the ratios

of the sums $\sum_i p_i Q_{jjjj}^{(i)}$ (no summation over j, $j = 1,2,3$), where p_i is the volume

fraction of the i-th family of inhomogeneities, and $Q_{jjjj}^{(i)}$ is the component $jjjj$ of the

Hill's tensor of inhomogeneity belonging to the family i. Additional details on the

choice of the shape Ω can be found in Sevostianov (2014).

In this paper, we consider pores in linearly elastic isotropic material. Note that

any value of the matrix Young's modulus E_0 can be used because all results presented

here are normalized by E_0. To find the compliance contribution tensor of a pore to be used in the single pore approach, we perform a set of six FEA simulations (three uniaxial tension and three shear loadcases) for the pore placed in a large reference volume and subjected to individual components of macroscopic strain given in Table 1. The simulation results are then processed using the procedure described in (Drach et al. (2011, 2014)). To validate the procedure, we calculated the H-tensors for a sphere and prolate spheroid (aspect ratio $\frac{a_2}{a_1} = 0.5$) for matrix Poisson's ratio $\nu_0 = 0.3$ and compared the results with analytical solutions presented in (Kachanov et al. (2003)) (corrected for misprint in David and Zimmerman (2011)). The maximum relative errors in the components were 0.5% and 0.3% for the sphere and spheroid, correspondingly. For the pore shown in Figure 1, the following components of $\mathbf{H}$-tensor are obtained:

$$
\begin{bmatrix}
\bar{H}_{1111} & \bar{H}_{1122} & \bar{H}_{1133} & \bar{H}_{1112} & \bar{H}_{1123} & \bar{H}_{1131} \\
\bar{H}_{2211} & \bar{H}_{2222} & \bar{H}_{2233} & \bar{H}_{2212} & \bar{H}_{2223} & \bar{H}_{2231} \\
\bar{H}_{3311} & \bar{H}_{3322} & \bar{H}_{3333} & \bar{H}_{3312} & \bar{H}_{3323} & \bar{H}_{3331} \\
\bar{H}_{1211} & \bar{H}_{1222} & \bar{H}_{1233} & \bar{H}_{1212} & \bar{H}_{1223} & \bar{H}_{1231} \\
\bar{H}_{2311} & \bar{H}_{2322} & \bar{H}_{2333} & \bar{H}_{2312} & \bar{H}_{2323} & \bar{H}_{2331} \\
\bar{H}_{3111} & \bar{H}_{3122} & \bar{H}_{3133} & \bar{H}_{3112} & \bar{H}_{3123} & \bar{H}_{3131}
\end{bmatrix}
=
\begin{bmatrix}
1.408 & -0.383 & 0.433 & -0.073 & 0.014 & 0.018 \\
-0.383 & 2.065 & -0.635 & -0.065 & -0.013 & -0.010 \\
-0.433 & -0.635 & 3.260 & 0.042 & -0.038 & -0.079 \\
-0.073 & -0.065 & 0.042 & 1.072 & -0.035 & -0.006 \\
0.014 & -0.013 & -0.038 & -0.035 & 1.689 & -0.021 \\
0.018 & -0.010 & -0.079 & -0.006 & -0.021 & 1.478
\end{bmatrix}
\tag{16}
$$

where the normalized components of $\mathbf{H}$ are defined as

$$
\bar{H}_{ijkl} = E_0 \left(\frac{V}{V_p} \right) H_{ijkl}, \tag{17}
$$

where $\frac{V_p}{V}$ is the volume fraction of the pore in the reference volume, E_0 is the Young's modulus of the matrix material, and the value $\nu_0 = 0.3$ is used. H-tensors for pores of

cubical, octahedral and tetrahedral shapes for several values of Poisson's ratio are provided in Appendix A.

Contribution of parallel pores of the same shape to the effective Young's moduli can be calculated using the following relationship:

$$\frac{E_i}{E_0} = \frac{1}{1+p\tilde{E}_i},$$

(18)

where $\tilde{E}_i$ $(i = 1,2,3)$ is a dimensionless parameter characterizing change in the Young's modulus in x_i-direction induced by the pores. Similar relationships are introduced for effective bulk and shear moduli in the case of randomly oriented pores:

$$\frac{K}{K_0} = \frac{1}{1+p\tilde{K}}, \quad \frac{G}{G_0} = \frac{1}{1+p\tilde{G}},$$

(19)

where $\tilde{K}$ and $\tilde{G}$ are dimensionless pore compressibility and shear compliance parameters representing change in bulk and shear moduli produced by the pores. All five parameters $(\tilde{E}_1, \tilde{E}_2, \tilde{E}_3, \tilde{K}$ and $\tilde{G})$ can be expressed in terms of the normalized H-tensor (see Equation (17)) as follows:

$$\tilde{E}_i = \bar{H}_{iiii} \quad \text{(no summation over } i)$$

$$\tilde{K} = \frac{T_{iijj}}{3}, \quad \tilde{G} = \frac{3T_{ijij} - T_{iijj}}{15} \quad \text{(summation over } i,j = 1,2,3)$$

(20)

where **T** is the Wu's strain concentration tensor, related to H-tensor and compliance tensor of the matrix material $\mathbf{S_0}$ as $\mathbf{H} = \mathbf{T}:\mathbf{S_0}$ (David and Zimmerman (2011)). Explicit expressions for parameters $\tilde{K}$ and $\tilde{G}$ in the case of spherical and randomly oriented spheroidal pores are given in (David and Zimmerman (2011)).

2.3 Homogenization based on direct FEA of periodic RVEs

2.3.1 Microstructure generation

To generate RVEs containing multiple pores for the full field approach, the pore shapes must be packed in a constrained volume without interpenetrations. The task is non-trivial and the solution approach depends on the existence of a robust algorithm to detect and prevent interpenetration or collision between pores.

Two types of approaches exist for regular shapes (including spheres, ellipsoids and long fibers): RSA and collective rearrangement methods (CRM). The former are based on the approach presented in (Widom (1966)), according to which a new particle is added to the arrangement only if it does not intersect any of the already existing particles, otherwise the new particle is placed in a different (randomly chosen) position and the check is repeated (see for example Lind (2009)). While RSA algorithms are relatively easy to implement, the number of iterations to achieve a microstructure free of interpenetrations increases exponentially with the increase of the target volume fraction. Random close packing (volume fraction of 0.64 in the case of monodisperse spheres, see, for example, (Song et al. (2008)) is virtually impossible to achieve with RSA methods. In the latter type, the final number of particles is generated simultaneously at the beginning of the procedure and then the particles are repositioned to obtain the interpenetration-free microstructure using, for example, molecular dynamics approaches (e.g. Donev et al. (2004), Lubachevsky (1991), Ghossein and Lévesque (2012)). While such techniques allow to achieve high density packings (up

to the theoretical hexagonal close packing volume fraction of 74% in the case of monodisperse spheres), they are more difficult to implement than the RSA methods. Packing of irregular shapes is usually performed by replacing them with assemblies of regular shapes (e.g. spheres, see Bertei et al. (2014)) or converting them to voxel representations, which significantly simplifies the collision/penetration detection (e.g. Byholm et al. (2009)) but requires more computational resources.

In the algorithm developed for this paper, irregular pore shapes are replaced with circumscribing ellipsoids, which are then packed using a simplified implementation of the CRM method based on Altendorf and Jeulin (2011). When compared to more advanced variations of the CRM (e.g. Ghossein and Lévesque (2012)), in the current approach the particles are not "grown" (or alternatively, the unit cell does not shrink) and they are not given velocities – they are moved instantaneously by the prescribed distance to remove interpenetrations. The process is repeated if new interpenetrations occur. Such simplifications result in easier implementation of the packing algorithm while still allowing for dense packing, however, come at a cost of increased computation time. Once the interpenetration-free packing of ellipsoids is attained, the original shapes are placed in the new positions of their ellipsoidal approximations. The choice of minimum volume circumscribing ellipsoid is described in Khachiyan (1996) and the procedure is implemented as a MATLAB function "lowner". The description and the function itself are available on the official MATLABCentral website.

The algorithm for packing ellipsoids in this paper is as follows. In the beginning, the desired number of ellipsoids with given aspect ratios and orientations is generated within a cubical volume. At this stage, the arrangement may contain interpenetrations. The ellipsoids intersecting the faces of the cubical volume are duplicated to the corresponding opposite faces of the volume to preserve periodicity. Next, pairs of potentially interpenetrating ellipsoids are considered to determine the amount of overlap and the shortest displacement vector to separate the ellipsoids (for geometrical aspects of this step see Perram and Wertheim (1985)). Once displacement vectors are calculated for all overlapping pairs, they are applied to all corresponding ellipsoids at once. New interpenetrations might occur, and in this case the process is repeated. The iterative procedure is carried on until interpenetration-free arrangement is obtained. Figure 2 illustrates the final arrangements of parallel and randomly oriented pores with porosity $p = 0.2$. The results presented in Section 2.4 were obtained for RVEs with 50 pores unless specified, see (El Moumen et al. (2015); Gusev (1997); Kanit et al. (2003)) for discussion on the appropriate choice of RVE for random composites.
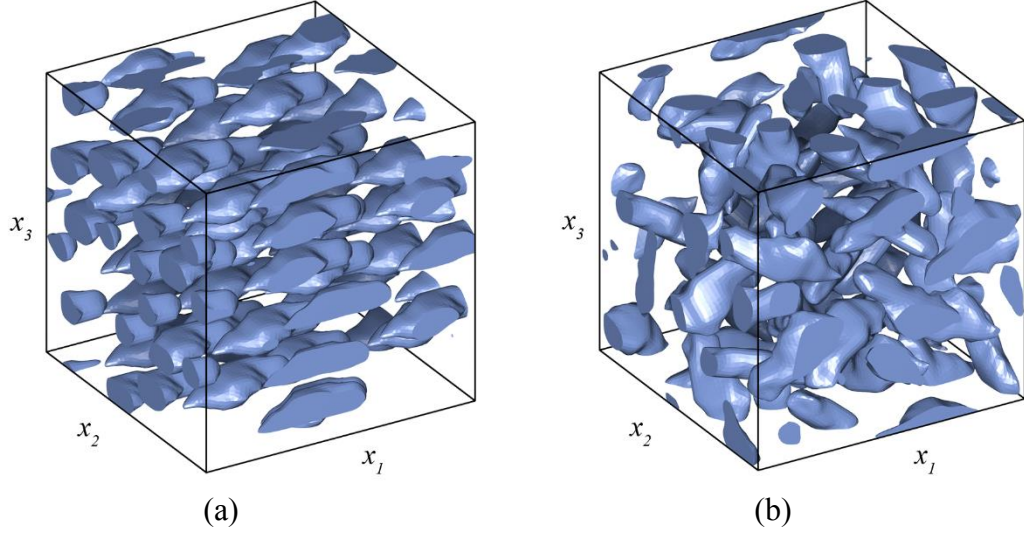
Figure 2. Examples of RVEs with porosity $p = 0.2$: (a) parallel pores; (b) randomly oriented pores

2.3.2 Characterization of the generated microstructures: homogeneity and isotropy

In this part, we focus on spatially homogeneous microstructures and non-uniform distributions such as clusters are not considered. In addition, for the cases of randomly oriented pores, the RVEs are expected to be isotropic. Both homogeneity and isotropy of a microstructure can be tested by analyzing the following two-point covariance function (also known as covariogram), see (El Moumen et al. (2015); Okabe and Blunt (2005); Smith and Torquato (1988); Torquato and Stell (1982)):

$$S_2(\mathbf{r_1}, \mathbf{r_2}) = <I(\mathbf{r_1}) \cdot I(\mathbf{r_2})>, \tag{21}$$

where $\mathbf{r_1}, \mathbf{r_2}$ are position vectors of two points within microstructure, angular brackets denote an ensemble average, and

$$I(\mathbf{r}) = \begin{cases} 1, & \text{if a point defined by } \mathbf{r} \text{ is in the pore phase} \\ 0, & \text{if a point defined by } \mathbf{r} \text{ is in the matrix phase} \end{cases}. \tag{22}$$

For statistically homogeneous medium S_2 is defined by the relative position vector $\mathbf{r} = \mathbf{r_2} - \mathbf{r_1}$ of the two studied points. If the medium is also isotropic, S_2 is a function of the relative distance $r = |\mathbf{r}|$ only. For such media it has the following limits

$$S_2(r = 0) = p,$$
$$\lim_{r \to \infty} S_2(r) = p^2, \tag{23}$$

where p is the volume fraction of the pore phase.

To test the isotropy of a microstructure, we compare three (one in each of the orthogonal directions) directional functions based on the *relative position*, while homogeneity test is based on the function of *relative distance* in all three directions. We start by converting RVE microstructures to voxel representations, each 700x700x700 voxels in size. In the isotropy test, we select a relative position vector $\mathbf{r}$ in one of the orthogonal directions (x_1, x_2 or x_3), and find every pair of voxels in the microstructure separated by $\mathbf{r}$ to calculate the corresponding directional function ($S_{2x_1}(\mathbf{r}), S_{2x_2}(\mathbf{r})$ or $S_{2x_3}(\mathbf{r})$) using Equation (11). To test the homogeneity, for every voxel in the volume we find all voxels that are located at the specified distance $r = |\mathbf{r}|$ from it in *all* three directions, and then calculate the distance function $S_2(r)$. We implemented the procedures for isotropy and homogeneity tests in MATLAB.

Figure 3a and Figure 3b illustrate two-point functions calculated using relative position for the RVEs containing 50 randomly oriented pores of irregular shape shown in Figure 1 with $p = 0.05$ and $p = 0.25$, respectively. The horizontal line in each

24

figure corresponds to the value p^2. In both plots $S_{2x_1}(\mathbf{r}), S_{2x_2}(\mathbf{r})$ or $S_{2x_3}(\mathbf{r})$ curves are very close to each other which is what we expect to see in isotropic microstructures. Figure 4a and Figure 4b depict two-point functions calculated using relative distance for the same RVEs. In both plots $S_2(r)$ follow the limits given in Equation (23). Hence, the microstructures are isotropic and homogenous.
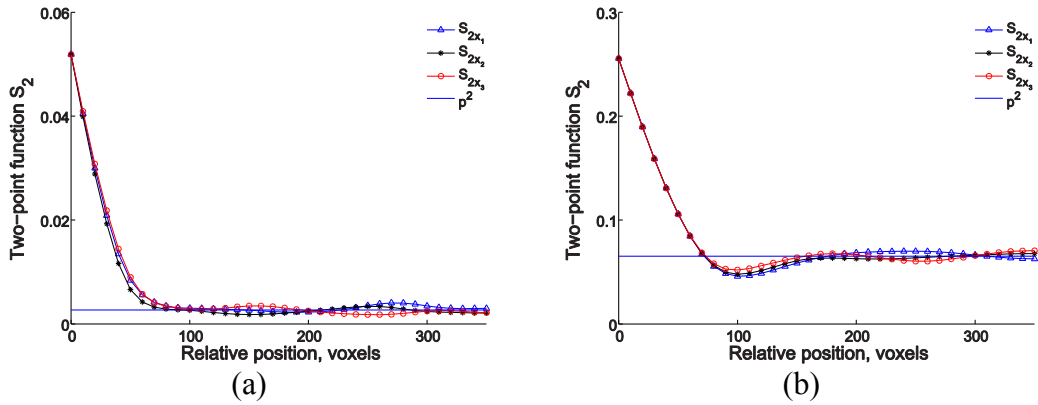
Figure 3. Two-point functions calculated for microstructures containing randomly oriented pores shown in Figure 1 using relative position along global coordinate axes with (a) $p = 0.05$ and (b) $p = 0.25$

For comparison, Figure 5a shows $S_2(r)$ functions generated for the following microstructure configurations: (1) 50 spheres randomly generated within RVE (interpenetrations allowed); (2) 50 spheres packed in RVE with maximum interpenetrations equal to one sphere radius; and (3) 50 spheres with no interpenetrations allowed. One can see that when full interpenetrations are allowed (case 1), the $S_2(r)$ function starts at p and monotonically decreases to the long-range value of p^2. When restrictions on the amount of interpenetration are imposed (case 2), $S_2(r)$ function

25
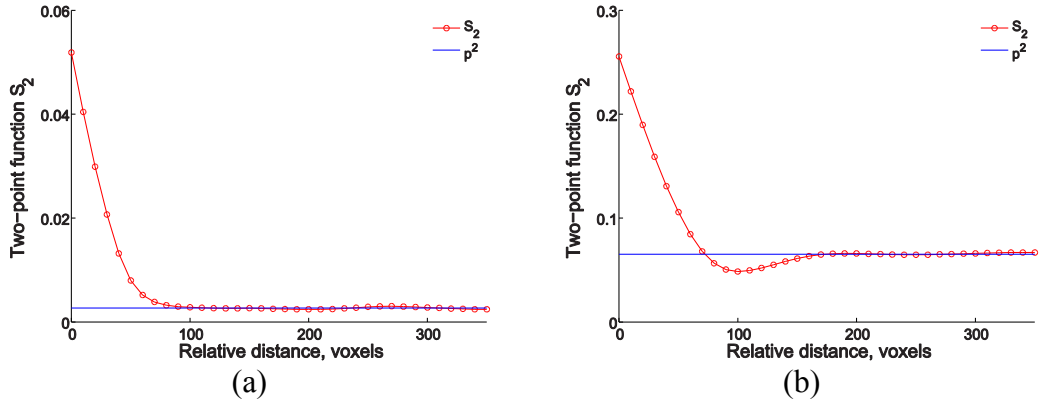
Figure 4. Two-point functions calculated for microstructures containing randomly oriented pores shown in Figure 1 using relative distance with (a) $p = 0.05$ and (b) $p = 0.25$

One can see that when full interpenetrations are allowed (case 1), the $S_2(r)$ function starts at p and monotonically decreases to the long-range value of p^2. When restrictions on the amount of interpenetration are imposed (case 2), $S_2(r)$ function starts oscillating about the limit p^2. For the microstructure with no interpenetrations (case 3), $S_2(r)$ function curve contains a characteristic dip (also observed in Figure 4b) as well as oscillations about p^2 It follows from these observations that introduction of some order in the immediate vicinity of the particle (also called the short-range order, in this case – restriction placed on particle interpenetrations) results in oscillations about the long-range limit of p^2. (Smith and Torquato (1988)) reported a similar observation and noted that the amplitude of oscillations depends on particle volume fraction and becomes negligible at greater relative distances.

Figure 5b shows $S_2(r)$ function for 50 spherical pores packed without interpenetrations into a single spherical cluster in a large RVE. The function goes to

26

zero at distances greater than the diameter of the cluster as expected. The short-range

order dip due to pore impenetrability as discussed above is also present in the plot.
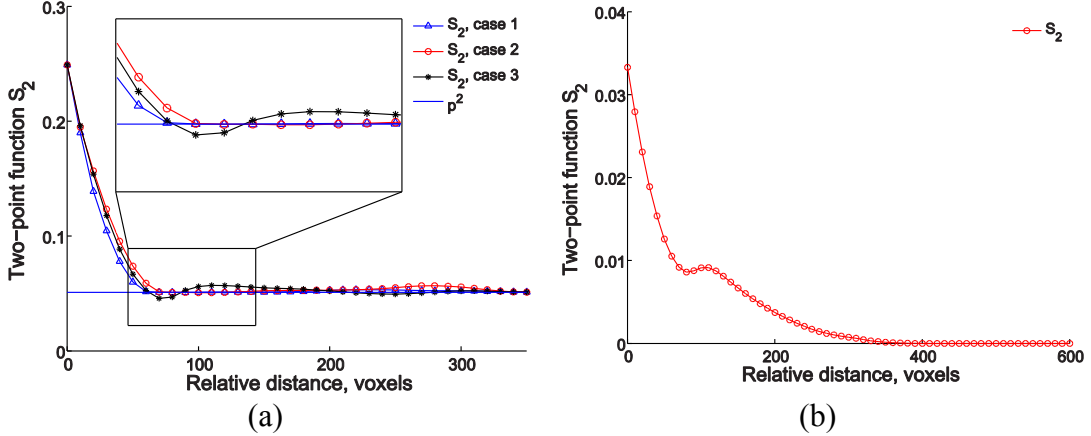
Figure 5. Two-point functions calculated using relative distance for (a) microstructures with spherical pores $p = 0.25$ and three cases of interpenetration conditions; (b) spherical cluster of spherical pores

The RVEs of the second type considered in this paper contain parallel pores. As before, we start with the isotropy test. Figure 6a,b illustrate two-point functions calculated using relative position for RVEs containing 50 parallel pores of irregular shape shown in Figure 1 with $p = 0.05$ and $p = 0.25$, respectively. Based on the plots we can conclude that there is no isotropy in the RVEs because of the difference in two-point functions $S_{2x_1}(\mathbf{r}), S_{2x_2}(\mathbf{r})$ and $S_{2x_3}(\mathbf{r})$. This can be explained by the shape of the pore, which has different cross-sectional areas normal to the three orthogonal directions. Figure 7a,b show two-point functions calculated using relative distance for the same RVEs. The functions are in good agreement with the limits postulated before, so we can claim homogeneity of the RVEs containing parallel pores. Note that the

27

isotropy of a structure can also be evaluated when the effective properties are known, see for example, (Sevostianov and Kachanov (2008)) and (Gusev (2016b)).
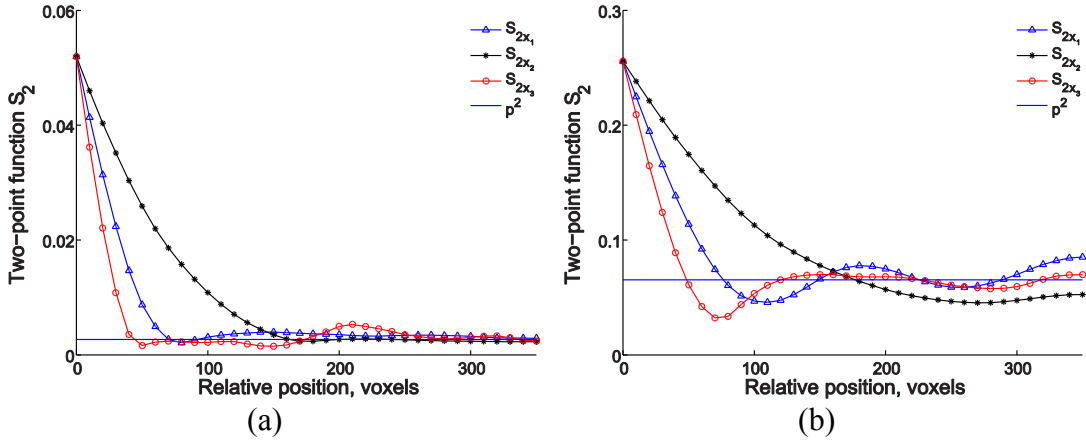
Figure 6. Two-point functions calculated for microstructures containing parallel pores of the shape shown in Figure 1 using relative position along global coordinate axes with (a) $p = 0.05$ and (b) $p = 0.25$
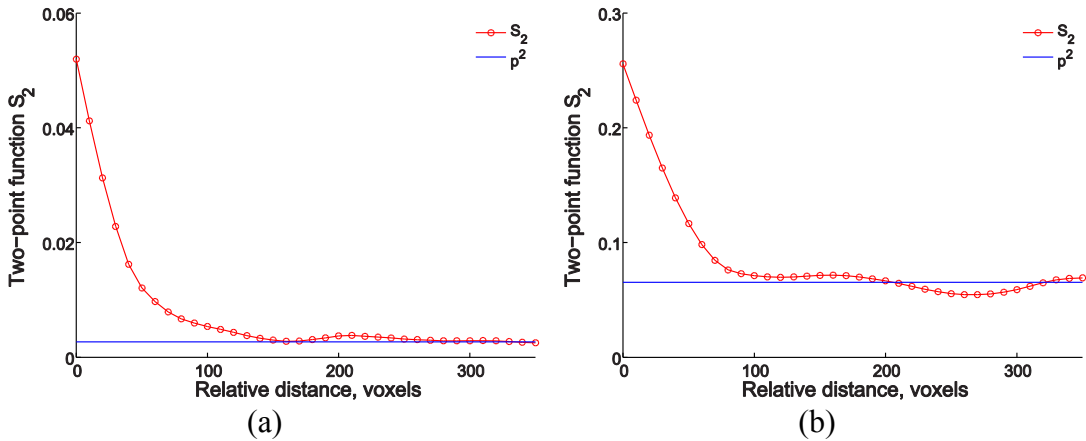
Figure 7. Two-point functions calculated for microstructures containing parallel pores of the shape shown in Figure 1 using relative distance with (a) $p = 0.05$ and (b) $p = 0.25$

28

2.3.3 Calculation of effective elastic properties of materials with simulated microstructures using FEA

The output of the microstructure generation code (RVE surface mesh) is imported into a commercial FEA software MSC Marc/Mentat for model preparation and subsequent analysis. All further preparation steps are performed automatically using a custom script that provides a ready-to-run model upon completion. Use of an automation script streamlines the process of model preparation and assures uniformity of the simulation results. This, in turn, simplifies the post-processing of data from various loadcases and architectures. The RVE is auto meshed with linear tetrahedral 3D elements (#134 using Marc classification). Note that linear tetrahedral elements are known to be stiffer than nonlinear due to constant strain within the elements (see, for example, (Benzleye et al. (1995); Cifuentes and Kalbag (1992)). For our analysis, we compared predictions obtained from models meshed with linear (tetra4) and quadratic tetrahedral (tetra10) elements. The resulting difference was on the order of 1% for the given discretization with maximum difference of 2.5% for one of the Young's moduli in the case of aligned pores of irregular shape shown in Figure 1. Due to the reasonably accurate predictions by linear elements and considerably higher computational demands of the simulations based on quadratic elements, tetra4 elements were used. Two typical RVE FEA meshes with the number of elements on the order of $2 \cdot 10^6$ are illustrated in Figure 8a,b.

In this chapter, the RVEs are treated as unit cells subjected to periodic boundary conditions.

<div style="text-align:center">(a)   (b)</div>
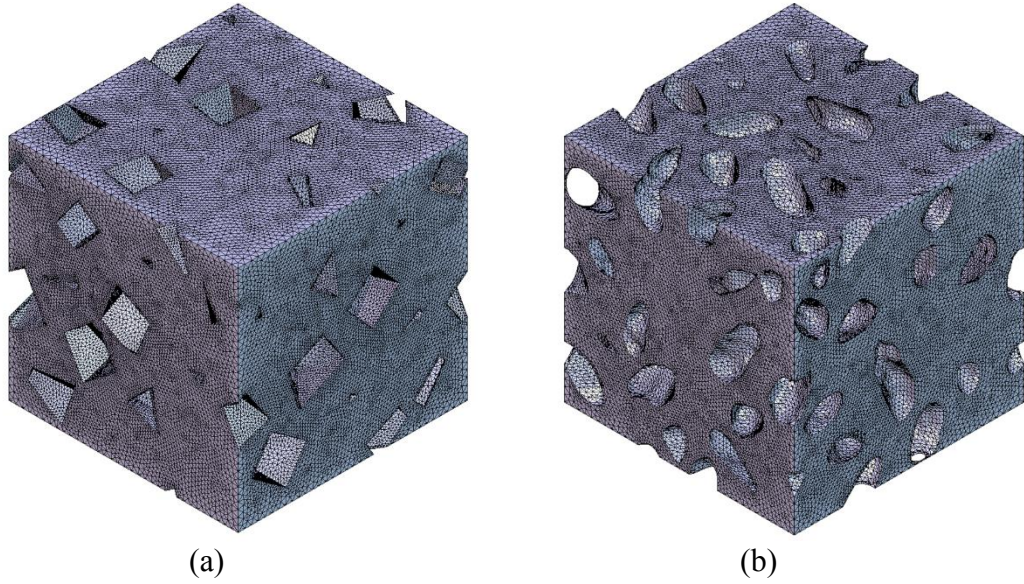
Figure 8. RVEs meshed with 3D elements in MSC Marc/Mentat containing randomly oriented: (a) octahedral pores, porosity $p = 0.2$; (b) irregular pores, porosity $p = 0.25$

The alternative approaches would be to prescribe either uniform displacements or uniform tractions on the RVE boundaries. It has been shown, however, that the effective elastic properties obtained with periodic boundary conditions are bounded by the results from the prescribed tractions and displacements, see (Hazanov and Huet (1994); Huet (1990); Suquet (1987)). The finite element meshes are generated to have the same surface mesh on the opposite faces of RVE. Periodic boundary conditions for two corresponding nodes on the opposite (positive and negative) faces are introduced similarly to Segurado and Llorca (2002):

$$u_j^{(i+)} = u_j^{(i-)} + \delta_j, \quad (j = 1,2,3) \tag{24}$$

where $u_j^{(i+)}$ and $u_j^{(i-)}$ are displacements in x_j direction of the i-th node on the positive and negative faces respectively; and δ_j is the average displacement in the x_j direction.

The periodic boundary conditions are applied in MSC Marc/Mentat using the "servo-link" feature (see, for example, (Drach et al. (2014); MSC Software (2012)). Servo-links allow prescription of multi-point boundary conditions for nodal displacements in the form of linear functions with constant coefficients. In this formulation, δ_j-s are implemented as translational degrees as translational degrees of freedom of control nodes, which are linked to the nodes on the corresponding opposite faces of an RVE (see Figure 9). Note that servo-link connection of two opposite faces requires congruent meshes on the faces.

To allow use of static FEA solution procedure, rigid body motion of an RVE needs to be restrained in a way that does not impose artificial strains. To eliminate rigid body displacements, a node inside the RVE is fixed. Any node can be used for the constraint as long as it is not on the surface of the RVE, because all surface nodes are tied in periodic boundary conditions equations. Rigid body rotations are not allowed by the periodic boundary conditions. Note that the applied strains corresponding to each loadcase are set to 0.001 to restrict element deformations to small values so that the initial element volumes could be used in the volume averaging procedure presented below. Once the numerical simulations are performed, the result files are processed using a custom Python script to calculate effective elastic properties of the RVE as follows. The script starts with calculating the average stress components within the RVE for each loadcase:

$$\langle \sigma_{ij} \rangle_m = \frac{1}{V} \sum_{l=1}^{N} \left(\sigma_{ij}^{(l)} \right)_m \cdot V^{(l)}, \quad (i,j = 1,2,3; \quad m = 1,2,\dots,6) \qquad (25)$$

where $\langle\sigma_{ij}\rangle_m$ is the volume average of the stress component ij calculated from the results of the m-th loadcase, V is the total volume of the RVE, $\left(\sigma_{ij}^{(l)}\right)_m$ is the stress component ij at the centroid of the finite element l calculated from the m-th loadcase, $V^{(l)}$ is the volume of the element l, and N is the total number of elements in the model.

Given the average stress components and applied strain, the effective stiffness tensor can be calculated from Hooke's law $\langle\sigma_{ij}\rangle_m = C_{ijkl}^{eff}(\varepsilon_{kl}^0)_m$ (summation over $k, l = 1,2,3$). For example, from the first loadcase all components C_{ij11}^{eff} are found:

$$C_{ij11}^{eff} = \frac{\langle\sigma_{ij}\rangle_1}{(\varepsilon_{11}^0)_1} \tag{26}$$

The values of engineering constants reported in Figure 10, Figure 11, Figure 12, Figure 13, Figure 15 and Figure 16 are then extracted from the effective stiffness components.
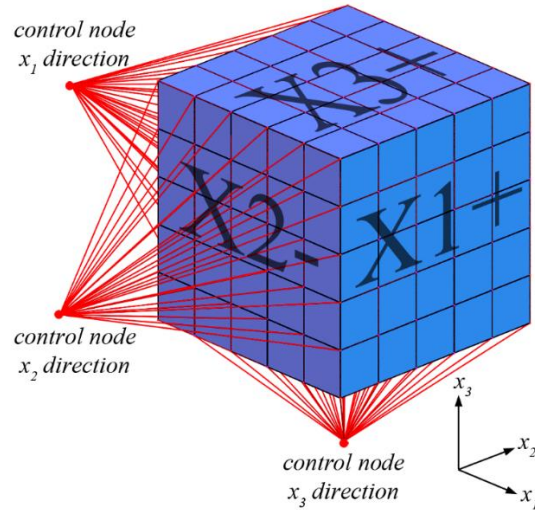
Figure 9. Illustration of periodic boundary conditions implementation in x_1, x_2 and x_3 directions using servo-links in MSC Marc/Mentat. Links (shown in red) connect opposite faces (positive and negative) of the RVE with corresponding control nodes

Table 1. Prescribed strains corresponding to the six loadcases used for calculation of an individual pore compliance contribution and effective elastic properties of RVEs

Prescribed average strain	Loadcase					
	1	**2**	**3**	**4**	**5**	**6**
ε_{11}^0	0.001	0	0	0	0	0
ε_{22}^0	0	0.001	0	0	0	0
ε_{33}^0	0	0	0.001	0	0	0
ε_{12}^0	0	0	0	0.001	0	0
ε_{23}^0	0	0	0	0	0.001	0
ε_{31}^0	0	0	0	0	0	0.001

2.4   Results

2.4.1 Regular shapes

Effective Young's (E_1, E_2, E_3), bulk (K) and shear (G) moduli of materials containing pores of "regular" shapes (sphere, oblate spheroid, cube and octahedron) were estimated via single pore solution (see Section 2.2) using non-interaction, Mori-Tanaka and Maxwell homogenization schemes based on numerically calculated H-tensors, see Figure 10, Figure 11, Figure 12 and Figure 13. Matrix Poisson's ratio $\nu_0 = 0.3$ was assumed in all cases considered in Section IV unless otherwise specified. The results were compared to direct FEA simulations (see Section III) with porosity levels $p = 0.10, 0.15, 0.20$. Note that each microstructure contained pores of the same shape. FEA results for three microstructure realizations are presented for each porosity value.

33

Each realization is shown as a separate data point, however some of them are very close to each other and thus indistinguishable.

Good correspondence between FEA results and Mori-Tanaka scheme predictions for spherical and spheroidal pores in the porosity range of 0-0.25 was previously reported in the literature, see for example (Segurado and Llorca (2002)). From the examination of Figure 10 and Figure 11a it can also be seen that Maxwell and Mori-Tanaka schemes produce identical predictions in the cases of spherical and aligned spheroidal pores. This observation coincides with the conclusions obtained for all aligned ellipsoidal inhomogeneities in Weng (2010). In the case of randomly oriented spheroidal, cubical and octahedral pores, the difference between Maxwell and Mori-Tanaka schemes is rather small. In the Maxwell scheme, the spherical shape of the effective inclusion was chosen for the microstructures with aligned and randomly oriented cubical as well as randomly oriented octahedral pores. For aligned octahedral pores, the effective inclusion was an oblate spheroid with aspect ratio of 0.95 (see discussion in Section 2.2). Note that the predictions for effective elastic properties of materials containing cubical pores can be found in (Hashemi et al. (2009)), however, we were not able to reproduce the results reported in that paper so they are not compared with our results. In addition, the conclusion in (Hashemi et al. (2009)) about effective bulk modulus being independent of the inhomogeneity shape directly contradicts our results, see Table 2.
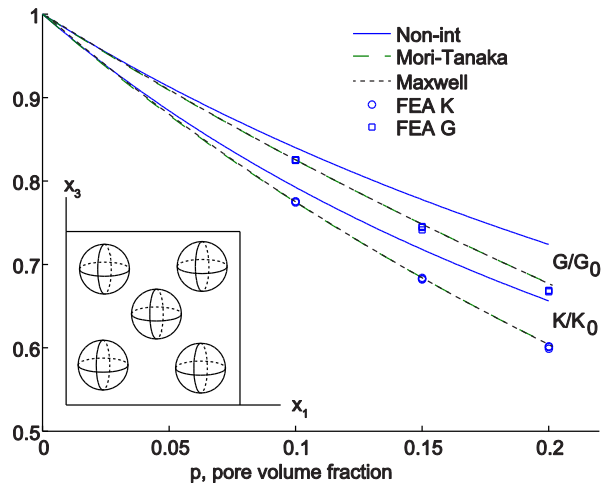
Figure 10. Effective bulk and shear moduli of a material with spherical pores

(a)   (b)
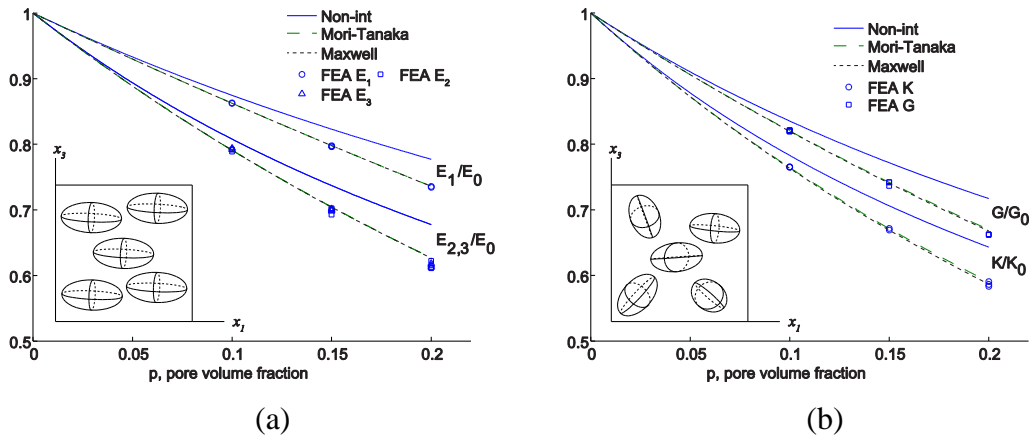
Figure 11. Effective elastic properties of a material containing prolate spheroidal $(\frac{a_2}{a_1} = 0.5)$ pores:(a) parallel orientations; (b) random orientations

35
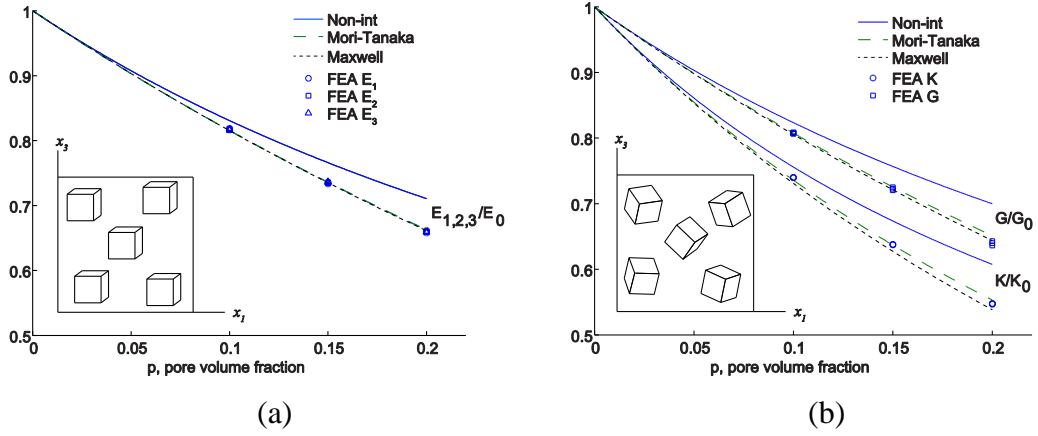
Figure 12. Effective elastic properties of a material containing cubical pores: (a) parallel orientations; (b) random orientations
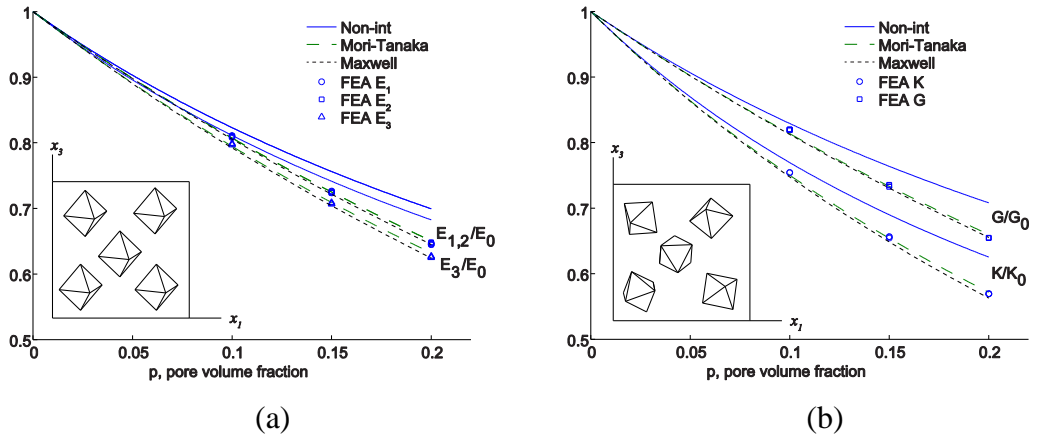
Figure 13. Effective elastic properties of a material containing octahedral pores: (a) parallel orientations; (b) random orientations

Given all components of **H**-tensor of a pore in one coordinate system, we can calculate the pore compliance contribution tensor in any other rotated coordinate system using the following coordinate transformation relationship:

$$H'_{mnop} = Q_{mi}Q_{nj}Q_{ok}Q_{pl}H_{ijkl}, \tag{27}$$

36

where $\mathbf{H}$ and $\mathbf{H}'$ are H-tensors in the original and transformed coordinate systems correspondingly, and $\mathbf{Q}$ is the transformation matrix. In the case of coordinate system rotation about x_3-axis only, the transformation matrix $\mathbf{Q}$ is

$$\mathbf{Q} = \begin{bmatrix} \cos(\theta) & \sin(\theta) & 0 \\ -\sin(\theta) & \cos(\theta) & 0 \\ 0 & 0 & 1 \end{bmatrix} \tag{28}$$

Thus, H-tensors of individual pore shapes can be used to analytically evaluate anisotropy of a material with parallel defects of the same type. Figure 14a and Figure 14b show dependence of the effective Young's moduli on the angle of the coordinate system in the case of a microstructure containing parallel cubical and octahedral pores respectively. Notice that with increase of porosity the degree of anisotropy of the cubical pores in the coordinate system oriented at and of the octahedral pores in the original coordinate system increases.

(a)   (b)
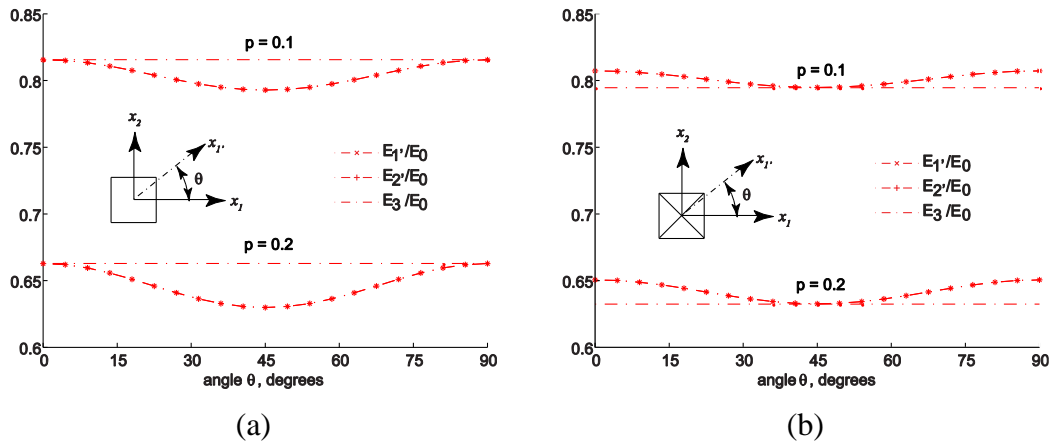
Figure 14. Variation of normalized effective Young's moduli with in-plane orientation of the coordinate system for microstructures containing (a) parallel cubical pores; (b) parallel octahedral pores. The results are obtained using Mori-Tanaka scheme and presented for porosities $p = 0.1$ and $p = 0.2$

2.4.2 Irregular shape

The approach used for calculation of effective elastic properties for regular shapes was applied to the irregular pore shown in Figure 1. Direct FEA calculations are compared with Mori-Tanaka and Maxwell scheme predictions for porosity levels levels $p = 0.10, 0.15, 0.20, 0.25$, see Figure 15. For the single pore solution, the H-tensor given in Equation (6) was used. FEA results for five microstructure realizations are presented for each porosity value. The effective inclusions in Maxwell scheme were found to be an ellipsoid (aspect ratios $\frac{a_2}{a_1} = 0.70$ and $\frac{a_3}{a_1} = 0.44$) and a sphere for the aligned and randomly oriented cases, respectively. Based on Figure 15, Maxwell scheme provides a slightly better fit for the direct FEA results for microstructures with aligned inhomogeneities, while Mori-Tanaka seems to provide a better fit for the randomly oriented pores.
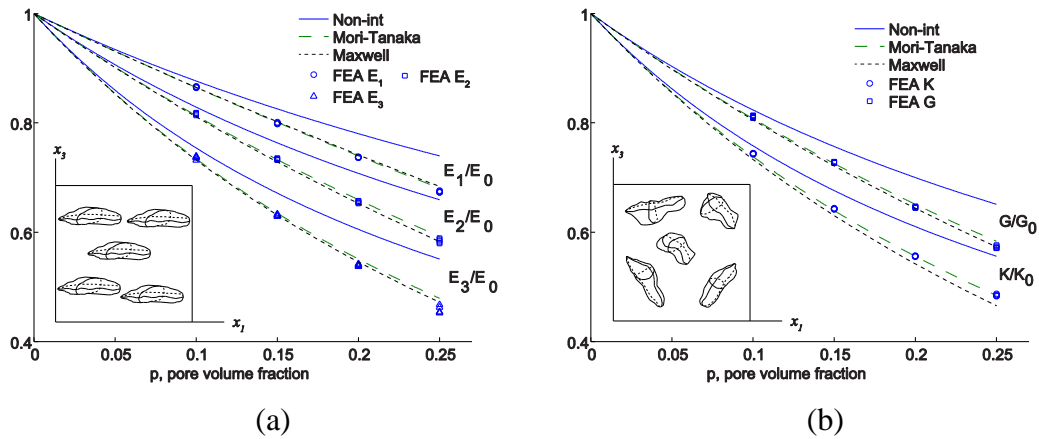
Figure 15. Effective elastic properties of a material containing irregular pores of the same shape shown in Figure 1: (a) parallel orientations; (b) random orientations

2.4.3 Mixture of regular and irregular pore shapes

Following the procedure established above we obtained the effective elastic properties of microstructures containing a mixture of two pore shapes (with equal volume fractions) – irregular pores shown in Figure 1 and prolate spheroidal pores with aspect ratio $\frac{a_2}{a_1} = 0.5$. Direct FEA calculations are compared with Mori-Tanaka and Maxwell scheme predictions for porosity levels $p = 0.10, 0.15, 0.20, 0.25$, see Figure 16. FEA results for three microstructure realizations are presented for each porosity value. The effective inclusions in Maxwell scheme were found to be an ellipsoid (aspect ratios $\frac{a_2}{a_1} = 0.65$ and $\frac{a_3}{a_1} = 0.52$) and a sphere for aligned and randomly oriented cases respectively. Overall, Maxwell scheme seems to fit the direct FEA simulations slightly better than Mori-Tanaka scheme for these microstructures.

(a) (b)
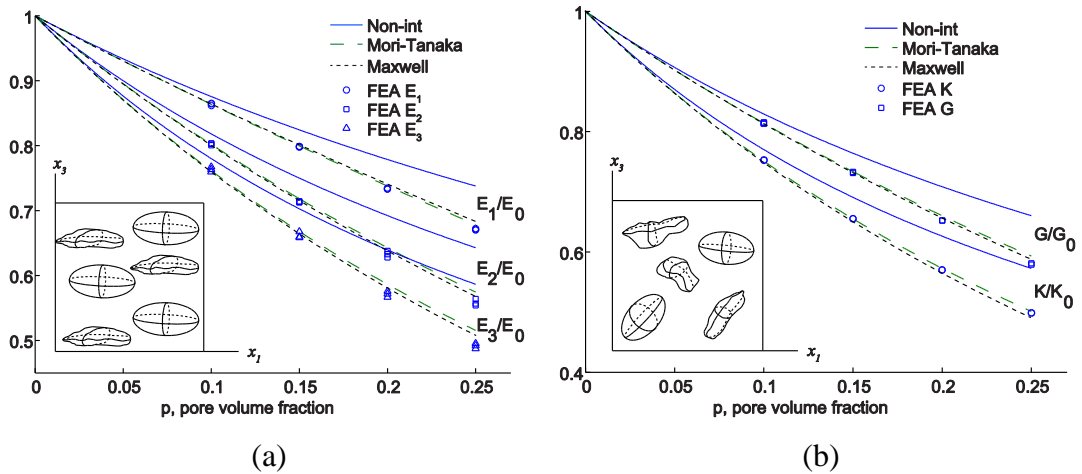
Figure 16. Effective elastic properties of a material containing a mixture of prolate spheroidal ($\frac{a_2}{a_1} = 0.5$) pores and irregular pores shown in Figure 1: (a) parallel orientations; (b) random orientations

2.4.4 Effect of pore shape

Table 2 provides a comparison of pore compliance contribution parameters with $\tilde{E}_1, \tilde{E}_2, \tilde{E}_3, \tilde{K}$ and $\tilde{G}$ (introduced in Section 2.2) for a sphere, oblate spheroid, cube, octahedron and irregular shape (shown in Figure 1). The results are presented in the coordinate axes shown in Appendix A. It is clear from the table that pore shape has a significant influence on the effective elastic properties of porous materials. In the case of randomly oriented pores, a tetrahedron is the most compliant of all considered shapes. Our results are consistent with previous observations and indicate that sphere is the stiffest pore shape. Comparing the contributions of parallel regular polyhedra, the greatest reduction in effective Young's moduli E_1, E_2 and E_3 is caused by tetrahedral pores.

Table 2. Summary of pore compliance contribution parameters of different pore shapes

	$\tilde{E}_1$	$\tilde{E}_2$	$\tilde{E}_3$	$\tilde{K}$	$\tilde{G}$
Sphere	2.005	2.005	2.005	2.625	1.909
Spheroid	1.435	2.381	2.381	2.776	1.973
Cube	2.035	2.035	2.035	3.229	2.143
Octahedron	2.149	2.149	2.326	2.995	2.061
Tetrahedron	2.570	2.570	2.474	4.034	2.410
Irreg. shape	1.408	2.065	3.260	3.194	2.144

The significant difference between contributions to E_1 and E_3 from parallel spheroidal and irregular pores can be attributed to the eccentricity of their shapes and quantified based on their normalized projected areas, see Drach et al. (2014).

2.4.5 Effect of matrix Poisson's ratio

The compliance contribution parameters $\tilde{E}_1$, $\tilde{E}_2$, $\tilde{E}_3$, $\tilde{K}$ and $\tilde{G}$ considered in this paper are normalized with respect to the corresponding moduli of the matrix material, see Equations 8 and 9. However, they depend on the matrix Poisson's ratio ν_0. In this sub-section, we investigate the effect of ν_0 on pore compliance contribution parameters and components of the H-tensor.

<u>Random orientations</u>

Table 3 presents pore compressibility $\tilde{K}$ and shear compliance $\tilde{G}$ parameters in the case of randomly oriented pores of spherical, spheroidal, cubical, octahedral, tetrahedral and irregular shape shown in Figure 1 for matrix Poisson's ratios $\nu_0 = 0.1, 0.2, 0.3, 0.4$. It is evident that both parameters depend on ν_0 – pore compressibility increases while shear compliance decreases with increase of ν_0. It is desirable to normalize $\tilde{K}$ and $\tilde{G}$ with respect to the matrix Poisson's ratio so that $\tilde{K}$ and $\tilde{G}$ determined for one value of ν_0 could be used to estimate these parameters for a different value. We consider two approximate methods to perform such normalization and evaluate their accuracy for the considered shapes. In the first method, we introduce the ν_0-normalized pore compressibility $\tilde{K}' = (1 - 4\nu_0^2) \cdot \tilde{K}_{(\nu_0)}$ and shear compliance $\tilde{G}' = (1 + \nu_0^2) \cdot \tilde{G}_{(\nu_0)}$. If these parameters are known for one value of ν_0, the pore compressibility and

shear compliance for a different value $\nu_{0'}$ are given by $\widetilde{K}_{(\nu_{0'})} = \frac{1}{\left(1 - 4\nu_{0'}^2\right)} \cdot \widetilde{K}'$ and

$$\widetilde{G}_{(\nu_{0'})} = \frac{1}{\left(1 + \nu_{0'}^2\right)} \cdot \widetilde{G}'.$$

Table 3. Pore compressibility and shear compliance parameters for different values of matrix Poisson's ratio

ν_0	$\widetilde{K}$				$\widetilde{G}$			
	0.1	0.2	0.3	0.4	0.1	0.2	0.3	0.4
Sphere	1.688	2.000	2.625	4.500	2.077	2.000	1.909	1.800
Spheroid	1.754	2.095	2.776	4.815	2.170	2.078	1.973	1.852
Cube	2.042	2.460	3.229	5.699	2.374	2.273	2.143	2.028
Octahedron	1.892	2.270	2.995	5.247	2.278	2.181	2.061	1.945
Tetrahedron	2.440	2.981	4.034	7.135	2.696	2.559	2.410	2.246
Irreg. shape	1.955	2.370	3.194	5.640	2.400	2.277	2.144	1.998

To test the accuracy of this approximation, we estimated $\widetilde{K}$ and $\widetilde{G}$ for $\nu_{0'} = 0.1, 0.2, 0.4$ based on the ν_0-normalized parameters calculated for $\nu_0 = 0.3$ and compared them with the values obtained using FEA. The relative errors of the approximation are given in Table 4. It is seen that with the exclusion of pore compressibility of the tetrahedral and irregular pore shapes for $\nu_{0'} = 0.1$, the approximation errors for $\widetilde{K}$ are below 6%. The approximation errors for pore shear compliance estimates for the considered shapes are below 4%.

Table 4. Relative errors of approximation for pore compressibility and shear compliance parameters based on the first method of normalization, %

$\nu_{0'}$	$\widetilde{K}$				$\widetilde{G}$			
	0.1	**0.2**	**0.3**	**0.4**	**0.1**	**0.2**	**0.3**	**0.4**
Sphere	-3.7	0.0	0.0	-3.7	0.8	0.0	0.0	0.3
Spheroid	-5.5	-1.0	0.0	-2.5	1.9	0.5	0.0	-0.1
Cube	-5.4	0.0	0.0	-0.7	2.6	1.2	0.0	0.7
Octahedron	-5.5	-0.5	0.0	-1.5	2.3	1.0	0.0	0.4
Tetrahedron	-10.2	-3.1	0.0	-0.5	3.5	1.3	0.0	-0.8
Irreg. shape	-8.9	-2.7	0.0	-0.7	3.6	1.3	0.0	-0.8

In the second method, we propose to normalize $\widetilde{K}$ and $\tilde{G}$ of a non-spherical pore by the corresponding parameters calculated for a sphere: $\widetilde{K}' = \widetilde{K}_{(\nu_0)}/\widetilde{K}_{(\nu_0)}^{(sph)}$, $\tilde{G}' = \tilde{G}_{(\nu_0)}/\tilde{G}_{(\nu_0)}^{(sph)}$. Then the pore compressibility and shear compliance for a different value of matrix Poisson's ratio $\nu_{0'}$ are given by $\widetilde{K}_{(\nu_{0'})} = \widetilde{K}' \cdot \widetilde{K}_{(\nu_{0'})}^{(sph)}$ and $\tilde{G}_{(\nu_{0'})} = \tilde{G}' \cdot \tilde{G}_{(\nu_{0'})}^{(sph)}$. To test the accuracy of this approximation, we estimated $\widetilde{K}$ and $\tilde{G}$ for $\nu_{0'} = 0.1, 0.2, 0.4$ based on the normalized parameters $\widetilde{K}'$ and $\tilde{G}'$ calculated for $\nu_0 = 0.3$ and compared them with the values obtained using FEA. The relative errors of the approximation are given in Table 5. It can be seen that all but one approximation errors for $\widetilde{K}$ for the considered shapes are below 5%. Similarly to the results of the first method, the maximum error is observed in the case of the tetrahedral shape for $\nu_{0'} = 0.1$. The approximation errors for $\tilde{G}$ for the considered shapes are below 3%. Overall, the second method results in lower approximation errors compared to the first.

Table 5. Relative errors of approximation for pore compressibility and shear compliance parameters based on the second method of normalization, %

$\nu_{0'}$	$\widetilde{K}$				$\widetilde{G}$			
	0.1	0.2	0.3	0.4	0.1	0.2	0.3	0.4
Spheroid	-1.7	-1.0	0.0	1.2	1.1	0.5	0.0	-0.5
Cube	-1.7	0.0	0.0	2.9	1.8	1.2	0.0	0.4
Octahedron	-1.8	-0.5	0.0	2.1	1.6	1.0	0.0	0.1
Tetrahedron	-6.3	-3.1	0.0	3.1	2.8	1.3	0.0	-1.2
Irreg. shape	-5.0	-2.7	0.0	2.9	2.8	1.4	0.0	-1.2

Parallel orientations

The H-tensor components of cubical, octahedral and tetrahedral pores are presented in Appendix A for matrix Poisson's ratio values $\nu_0 = 0.1, 0.2, 0.3, 0.4$. We analyze the dependence of three groups of components on ν_0: (a) $\bar{H}_{1111}, \bar{H}_{2222}, \bar{H}_{3333}$; (b) $\bar{H}_{1122}, \bar{H}_{2233}, \bar{H}_{3311}$; (c) $\bar{H}_{1212}, \bar{H}_{2323}, \bar{H}_{3131}$. It can be seen that components in group (a) exhibit little dependence on ν_0 − the maximum relative difference of 6.8% between $\nu_0 = 0.1$ and $\nu_0 = 0.4$ is observed for the irregular pore.

The components in groups (b) and (c) exhibit greater dependence on ν_0. We propose to normalize these components using the approximating ellipsoid found for each shape based on its projected areas along principal directions (see (Borys Drach et al., 2014)). The normalization is performed by dividing the H-tensor components of a considered shape by the corresponding components of the ellipsoid. As with

normalization in the case of random orientations, this allows to separate Poisson's ratio and pore shape effects, and use the parameters calculated for one value of ν_0 to estimate them for a different Poisson's ratio. For example, to estimate $\bar{H}_{1122}$ for $\nu_{0'}$ based on $\bar{H}_{1122}$ for ν_0 the following expression can be used

$$\bar{H}_{1122}^{(\nu_{0'})} = \frac{\left(\bar{H}_{1122}^{(\nu_{0'})}\right)_{ell}}{\left(\bar{H}_{1122}^{(\nu_0)}\right)_{ell}} \bar{H}_{1122}^{(\nu_0)}$$

where $\left(\bar{H}_{1122}^{(\nu_0)}\right)_{ell}$ and $\left(\bar{H}_{1122}^{(\nu_{0'})}\right)_{ell}$ are components 1122 of the H-tensors of the approximating ellipsoid calculated for ν_0 and $\nu_{0'}$ correspondingly. To test the accuracy of this approximation, we estimated H-tensor components in groups (b) and (c) for $\nu_{0'} = 0.1, 0.2, 0.4$ based on the components calculated for $\nu_0 = 0.3$ and compared them with the values obtained using FEA. The relative errors of the approximation are presented in Table 6 and Table 7.

Table 6. Relative errors of approximation for H-tensor components $\bar{H}_{1122}, \bar{H}_{2233}$ and $\bar{H}_{3311}$ based on the normalization by corresponding components of approximating ellipsoids, %

	$\bar{H}_{1122}$				$\bar{H}_{2233}$				$\bar{H}_{3311}$			
$\nu_{0'}$	0.1	0.2	0.3	0.4	0.1	0.2	0.3	0.4	0.1	0.2	0.3	0.4
Cube	-4.6	-1.9	0.0	0.8	-4.6	-1.9	0.0	0.8	-4.6	-1.9	0.0	0.8
Octahedron	6.2	2.5	0.0	-4.5	0.1	0.0	0.0	2.1	0.1	0.0	0.0	2.1
Tetrahedron	1.5	0.3	0.0	0.2	4.2	1.8	0.0	-1.1	4.2	1.8	0.0	-1.1
Irreg. shape	-0.3	-0.3	0.0	0.3	4.1	2.0	0.0	-2.2	1.7	0.5	0.0	-0.4

Table 7. Relative errors of approximation for H-tensor components $\bar{H}_{1212}, \bar{H}_{2323}$ and $\bar{H}_{1313}$ based on the normalization by corresponding components of approximating ellipsoids, %

$\nu_{0'}$	$\bar{H}_{1212}$				$\bar{H}_{2323}$				$\bar{H}_{1313}$			
	0.1	0.2	0.3	0.4	0.1	0.2	0.3	0.4	0.1	0.2	0.3	0.4
Cube	0.2	0.4	0.0	1.2	0.2	0.4	0.0	1.2	0.2	0.4	0.0	1.2
Octahedron	4.5	2.7	0.0	-1.2	-0.1	0.0	0.0	0.7	-0.1	0.0	0.0	0.7
Tetrahedron	3.4	1.7	0.0	-1.4	0.8	0.3	0.0	0.0	0.8	0.3	0.0	0.0
Irreg. shape	0.1	0.0	0.0	0.0	1.2	0.6	0.0	-0.4	0.3	0.1	0.0	0.0

Note, that in the case of the cube the approximating ellipsoid is a sphere. In the case of the octahedron, tetrahedron and considered irregular pore shape the approximating ellipsoids have aspect ratios $\left[\frac{a_2}{a_1} = 1.000, \frac{a_3}{a_1} = 0.708\right]$, $\left[\frac{a_2}{a_1} = 0.975, \frac{a_3}{a_1} = 1.004\right]$ and $\left[\frac{a_2}{a_1} = 0.475, \frac{a_3}{a_1} = 0.318\right]$, respectively. It can be seen from the tables that with the exclusion of component $\bar{H}_{1122}$ of the octahedral shape for $\nu_{0'} = 0.1$ the approximation errors in H-tensor components are within 5%.

2.5 Conclusions

The proposed simplified packing algorithm utilizing the collective rearrangement method is an efficient tool for generating RVEs containing pores of regular and irregular shapes as well as their mixtures. The resulting microstructures are homogeneous as confirmed by the analysis of their covariograms. In the case of randomly oriented pores, the microstructures are also isotropic.

Compliance contribution tensors (H-tensors) for pores of various shapes obtained by FEA of a reference volume with a single pore can be used to predict the overall effective elastic properties using the first-order micromechanical schemes such as Mori-Tanaka or Maxwell. The difference between the results of these two schemes is not very significant for the considered pore shapes and porosity ranges (up to 0.25 volume fraction of pores). As expected (see Sevostianov (2014); Weng (2010)), the predictions of Mori-Tanaka and Maxwell schemes coincide in the case of spherical pores and parallel spheroidal pores. H-tensors of cubical, octahedral and tetrahedral pores for several values of matrix Poisson's ratio presented in Appendix are published in explicit form for the first time.

Good correspondence is observed between direct FEA simulations of periodic RVEs and analytical micromechanical predictions based on H-tensors for microstructures containing pores of the same shape. For mixtures of pores of two different shapes it appears that the properly implemented Maxwell scheme (with the choice of the effective ellipsoid as recommended in (Sevostianov (2014)) provides a slightly better fit of the numerical simulation data. Note that these observations are limited to the considered range of pore volume fractions (0-25%). For higher volume fractions, the Mori-Tanaka scheme, for example, will not remain as accurate, see results of Segurado and Llorca (2002) for spherical pores.

The results of this paper clearly indicate that effective bulk modulus of porous solids depends on the pore shape. Similar conclusions have been made about 2D shapes, see for example, Ekneligoda and Zimmerman, (2006). This is in direct

contradiction with the controversial conclusions presented in Hashemi et al. (2009), which we believe need to be revisited.

We also present approximate methods to normalize pore compliance contribution parameters of the considered shapes with respect to matrix Poisson's ratio ν_0. This allows to separate Poisson's ratio and pore shape effects, so that the parameters calculated for one value of ν_0 can be used for other Poisson's ratios.

3.0   HOMOGENIZATION OF LINEARLY ELASTIC MATERIALS REINFORCED WITH PARTICLES OF POLYHEDRAL SHAPES

Abstract. Contributions of 15 convex polyhedral particle shapes to the overall elastic properties of particle-reinforced composites are predicted using micromechanical homogenization and direct finite element analysis approaches. The micromechanical approach is based on the combination of the stiffness contribution tensor (N-tensor) formalism with Mori-Tanaka and Maxwell homogenization schemes. The second approach involves FEA simulations performed on artificial periodic representative volume elements containing randomly oriented particles of the same shape. The results of the two approaches are in good agreement for volume fractions up to 30%. Applicability of the replacement relation interrelating N-tensors of the particles having the same shape but different elastic constants is investigated and a shape parameter correlated with the accuracy of the relation is proposed. It is concluded that combination of the N-tensor components of the 15 shapes presented for three values of matrix Poisson's ratios with the replacement relation allows extending the results of this paper to matrix/particle material combinations not discussed here.

3.1   Introduction

Regular polyhedra can be used to describe shapes of some crystalline metallic particles that are encountered as precipitates or synthesized as powders to be used as additives in particle-reinforced composites ((Menon & Martin, 1986; Miyazawa, Aratake, & Onaka, 2012; Niu et al., 2009; Onaka, Kobayashi, Fujii, & Kato, 2003;

49

Sundquist, 1964; Wang, 2000)). Table 8 presents microscopy images of particles having polyhedral shapes along with their idealized shapes.

In this chapter, we analyze the effect of shape of several representative convex polyhedral on the overall elastic properties of particle-reinforced composites. Traditionally, the effect of inhomogeneities on elastic properties of materials is described using the classical (Eshelby, 1957) and (Eshelby, 1961) results for an ellipsoidal inhomogeneity. It means that the shape of the inhomogeneities is explicitly or implicitly assumed to be ellipsoidal (in most cases – just spherical). Few results on inhomogeneities having irregular geometry have been published in literature. In 2D, general cases of pores and inhomogeneities of arbitrary irregular shape have been studied using conformal mapping approach, see for example (Ekneligoda & Zimmerman, 2006, 2008; I. Jasiuk et al., 1994; Mogilevskaya & Nikolskiy, 2015; Tsukrov & Novak, 2002, 2004; Zimmerman, 1986).
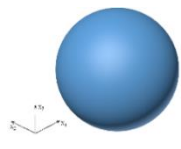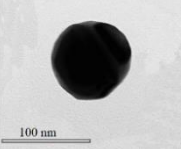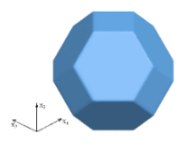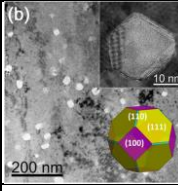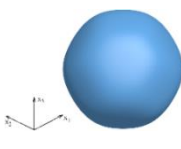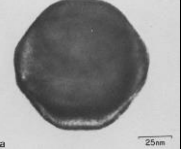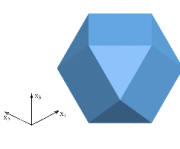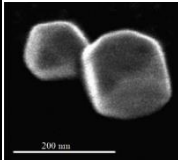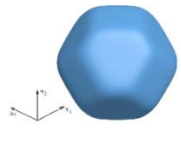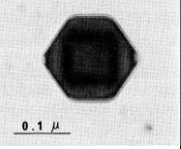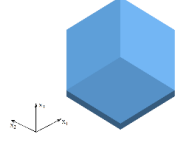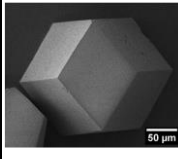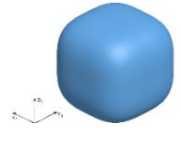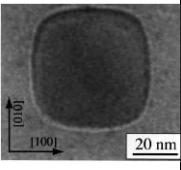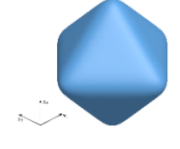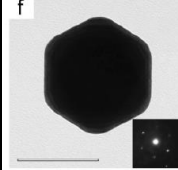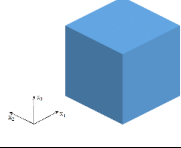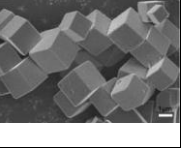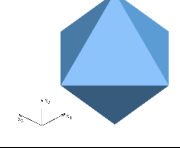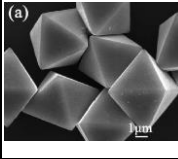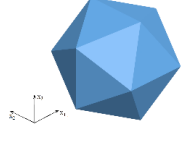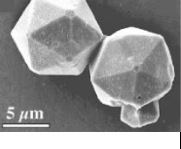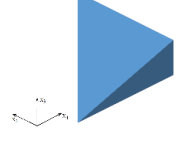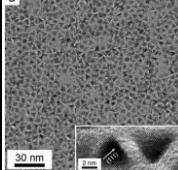
In 3D, several results for contributions of irregularly shaped inhomogeneities to effective elastic properties exist. Solutions for cracks having irregular shape are presented in (Mark Kachanov & Sevostianov, 2012). Effect of concavity factor of superspheres and axisymmetric concave pores has been analyzed in the works of (I. Sevostianov et al., 2008), (Igor Sevostianov & Giraud, 2012), (F. Chen et al., 2015) and (Igor Sevostianov et al., 2016). The authors supplemented finite element analysis (FEA) calculations with analytical approximations for compliance contribution tensors of pores of such shapes. The possibility to extend the results from pores to inhomogeneities with arbitrary properties has been discussed by Chen et al (2017). The

authors showed that replacement relations ((Igor Sevostianov & Kachanov, 2007)) that allow calculation of the compliance contribution tensor of an inhomogeneity from the one of a pore of the same shape are applicable to convex inhomogeneities only. Concave inhomogeneities require direct calculation of property contribution tensors. (Borys Drach et al., 2011) used FEA calculations to obtain compliance contribution tensors of several 3D irregularly shaped pores typical for carbon-carbon composites, and (Borys Drach, Tsukrov, & Trofimov, 2016) presented numerically obtained compliance contribution tensors of cubical, octahedral and tetrahedral pores. (Garboczi & Douglas, 2012) presented a procedure to approximate bulk and shear elastic contribution parameters in the case of randomly oriented inhomogeneities shaped as blocks.

The effect of shape of an irregular inhomogeneity can also be analyzed by considering representative volume elements (RVEs) containing periodic arrangements of randomly oriented inhomogeneities. (Rasool & Böhm, 2012) analyzed contributions of spherical, cubical, tetrahedral and octahedral inhomogeneities to the effective thermoelastic properties of particle-reinforced composites. The results were obtained for the material combination with the particles ten times stiffer than the matrix and for the volume fraction of 20%. Recently, (Helmut J. Böhm & Rasool, 2016) extended the approach by considering elasto-plastic behavior of the matrix material. In addition to the contribution tensors of individual pores, (Borys Drach et al., 2016) used FEA to study the shape effects of cubical, octahedral and tetrahedral pores on the overall elastic

properties of porous materials using periodic RVEs containing parallel and randomly

oriented pores.

Table 8. Examples of ipolyhedral shapes

Shape	Idealized	Microscopy	Shape	Idealized	Microscopy
Sphere [1]			Truncated Octahedron [6]		
Polyhedral Supersphere (smooth) [2]			Cuboctahedron [7]		
Polyhedral Supersphere (smooth) [2]			Rhombic Dodecahedron [8]		
Cube (smooth) [3]			Octahederon (smooth) [7]		
Cube [4]			Octahederon [9]		
Icosahedron [5]			Tetrahedron [10]		

[1] (Seo, Ji, & Song, 2006)
[2] (Menon & Martin, 1986)
[3] (Onaka et al., 2003)
[4] (Cao et al., 2010)
[5] (McMillan, 2003)

[6] (Zeon Han et al., 2015)
[7] (Seo et al., 2006)
[8] (Cravillon et al., 2012)
[9] (Sun & Yang, 2014)
[10] (Park, Jang, Kim, & Son, 2007)

The shapes in Table 8 can be described using the following general formula combining different types of polyhedra ((Miyazawa et al., 2012; Onaka, 2006, 2016)):

$$\left[A_1 h_{hexa} + \frac{A_2}{a^p} h_{octa} + \frac{A_3}{b^p} h_{dodeca}\right]^{1/p} + A_4 h_{icosa}{}^{1/p} + A_5 h_{tetra}{}^{1/p} = 1, \quad (29)$$

where $A_1, A_2, A_3, A_4, A_5, A_6$ are constants, p is a shape parameter, and h_{hexa}, h_{octa}, h_{dodeca}, h_{icosa} and h_{tetra} are functions that are given below:

$$h_{hexa} = |x|^p + |y|^p + |z|^p,$$

$$h_{octa} = |x + y + z|^p + |-x + y + z|^p + |x - y + z|^p + |x + y - z|^p,$$

$$h_{dodeca} = |x + y|^p + |x - y|^p + |y + z|^p + |y - z|^p + |x + z|^p + |x - z|^p,$$

$$h_{icosa} = |f(\gamma, \gamma, \gamma)|^p + |f(-\gamma, \gamma, \gamma)|^p + |f(\gamma, -\gamma, \gamma)|^p + |f(\gamma, \gamma, -\gamma)|^p +$$

$$|f(\xi, \eta, 0)|^p + |f(\xi, -\eta, 0)|^p + |f(0, \xi, \eta)|^p + |f(0, \xi, -\eta)|^p + |f(\eta, 0, \xi)|^p +$$

$$|f(\eta, 0, -\xi)|^p,$$

$$h_{tetra} = H(\gamma, \gamma, \gamma) + (1/p)^{(p-2)} H(-\gamma, -\gamma, -\gamma),$$

where

$$f(a, b, c) = |ax + by + cz|^p, \gamma = \frac{1}{\sqrt{3}}, \xi = \sqrt{\frac{3 - \sqrt{5}}{6}}, \eta = \sqrt{\frac{3 + \sqrt{5}}{6}},$$
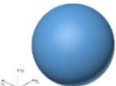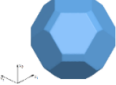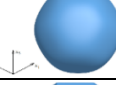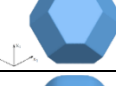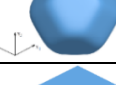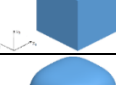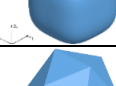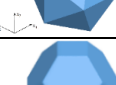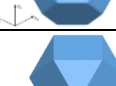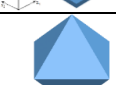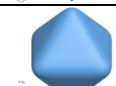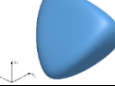
$$H(\gamma, \gamma, \gamma) = \{h(\gamma, \gamma, \gamma)\}^p + \{h(\gamma, -\gamma, -\gamma)\}^p + \{h(-\gamma, \gamma, -\gamma)\}^p + \{h(-\gamma, -\gamma, \gamma)\}^p,$$

$$h(a, b, c) = \{|f(a, b, c)| - f(a, b, c)\}/2.$$

Using formula (29) we obtained 15 polyhedral shapes that are analyzed in this paper, see Table 9. In the present work, we utilize stiffness contribution tensor formalism to estimate overall elastic properties of materials with polyhedral inhomogeneities and compare the results with direct finite element simulations of periodic RVEs. The

concept of the stiffness contribution tensor is introduced in section 3.2. The section also details our numerical approach to calculation of stiffness contribution tensors of individual inhomogeneities. In section 3.3, we present the components of stiffness contribution tensors of all shapes shown in Table 9. In addition, we investigate the applicability of replacement relations to the considered shapes and introduce a parameter correlating the accuracy of the relations with a shape's geometry. Predictions of the effective elastic properties for particle-reinforced materials with randomly oriented polyhedral inhomogeneities based on stiffness contribution tensors are presented in section 3.4. The predictions obtained using non-interaction, Mori-Tanaka and Maxwell micromechanical homogenization schemes are compared with direct finite element simulations of periodic RVEs. Section 3.6 presents the conclusions of the paper. Finally, stiffness contribution tensors of the considered polyhedral shapes for two Poisson's ratio values $\nu_0 = 0.2$ and $\nu_0 = 0.4$ of the matrix (in addition to the results for $\nu_0 = 0.3$ presented in section 3) are given in the Appendix B.

Table 9. Considered polyhedral shapes

#	Shape	Image	A_1	A_2	A_3	A_4	A_5	a	b	p
1	Sphere		1	0	0	0	0	1	1	2
2	Polyhedral Supersphere 1		1	1	1	0	0	1.69	1.58	$p \rightarrow \infty$
3	Polyhedral Supersphere 1 (smooth)		1	1	1	0	0	1.69	1.58	$p = 9$
4	Polyhedral Supersphere 2		1	1	1	0	0	1.67	1.72	$p \rightarrow \infty$
5	Polyhedral Supersphere 2 (smooth)		1	1	1	0	0	1.67	1.72	$p = 14.4$
6	Cube		1	0	0	0	0	1	1	$p \rightarrow \infty$
7	Cube (smooth)		1	0	0	0	0	1	1	$p = 3.3$
8	Icosahedron		0	0	0	1	0	1	1	$p \rightarrow \infty$
9	Truncated Octahedron		1	1	0	0	0	1.2	1	$p \rightarrow \infty$
10	Cuboctahedron		0	1	1	0	0	2	2	$p \rightarrow \infty$
11	Rhombic Dodecahedron		0	0	1	0	0	1	1	$p \rightarrow \infty$
12	Octahederon		0	1	0	0	0	1	1	$p \rightarrow \infty$
13	Octahederon (smooth)		0	1	0	0	0	1	1	$p = 6.44$
14	Tetrahedron		0	0	0	0	1	1	1	$p \rightarrow \infty$
15	Tetrahedron (smooth)		0	0	0	0	1	1	1	$p = 4$

3.2   Property contribution tensors

Property contribution tensors were first introduced as compliance contribution tensors in the context of pores and cracks by Horii and Nemat-Nasser (1983). Components of such tensors were calculated for 2D pores of various shape and 3D ellipsoidal pores in isotropic material by Kachanov et al. (1994). For the general case of an elastic ellipsoidal inhomogeneity, compliance contribution tensor and its counterpart − stiffness contribution tensor − were presented in Sevostianov and Kachanov (1999, 2002). (Kushch & Sevostianov, 2015) established the link between these tensors and dipole moments.

Following (Igor Sevostianov & Kachanov, 1999), we consider a homogeneous isotropic elastic material (matrix) with a stiffness tensor $\mathbf{C}_0$ containing an inhomogeneity of volume V_1 that has a different stiffness $\mathbf{C}_1$. Fourth-rank stiffness contribution tensor $\mathbf{N}$ of an inhomogeneity relates additional stress due to the presence of the inhomogeneity $\mathbf{\Delta\sigma}$ (per reference volume V of the elastic material including the inhomogeneity) with applied strain $\mathbf{\varepsilon}^0$:

$$\Delta\sigma_{ij} = N_{ijkl}\varepsilon_{kl}^0 \tag{30}$$

Strain distribution $\mathbf{\varepsilon}$ is assumed to be uniform inside V in the absence of the inhomogeneity. Thus, the stiffness contribution tensor, which characterizes the far-field asymptotic of the elastic fields generated by an inhomogeneity, determines its contribution to the effective elastic properties (Sevostianov and Kachanov, 2011). We calculate the stiffness contribution tensors (**N**-tensors) of individual particles using

FEA. In the procedure, for a given particle geometry we simulate a single inhomogeneity in a large volume subjected to remotely applied uniform displacement fields. To prepare the necessary 3D FEA mesh for the analysis, we begin by generating the surface mesh of the particle in a custom MATLAB script using formula (29) and built-in function "isosurface.m". Figure 17 shows the truncated octahedron and icosahedron surface meshes generated using our script. Each mesh is composed of approximately 50,000 elements. The generated surface mesh of a particle is then used in the numerical procedure to find components of the particle property contribution tensor as described below.

(a)   (b)
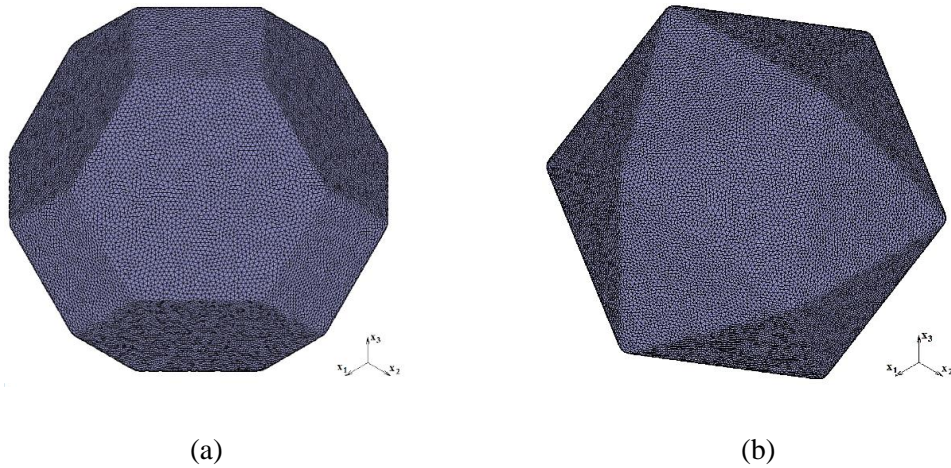
Figure 17. Example of a particle surface mesh: a) truncated octahedron; b) icosahedron

Particle surface mesh is placed in a large cubic-shaped reference volume with sides five times bigger than the largest linear dimension of the particle to reduce boundary effects and simulate remote loading (Drach et al.(2011). This setup is auto meshed with the

10-node non-linear tetrahedral 3D elements (tetra10) due to higher accuracy of the results compared to the 4-node linear elements (tetra4), see Figure 18.

<center>(a)</center>   <center>(b)</center>
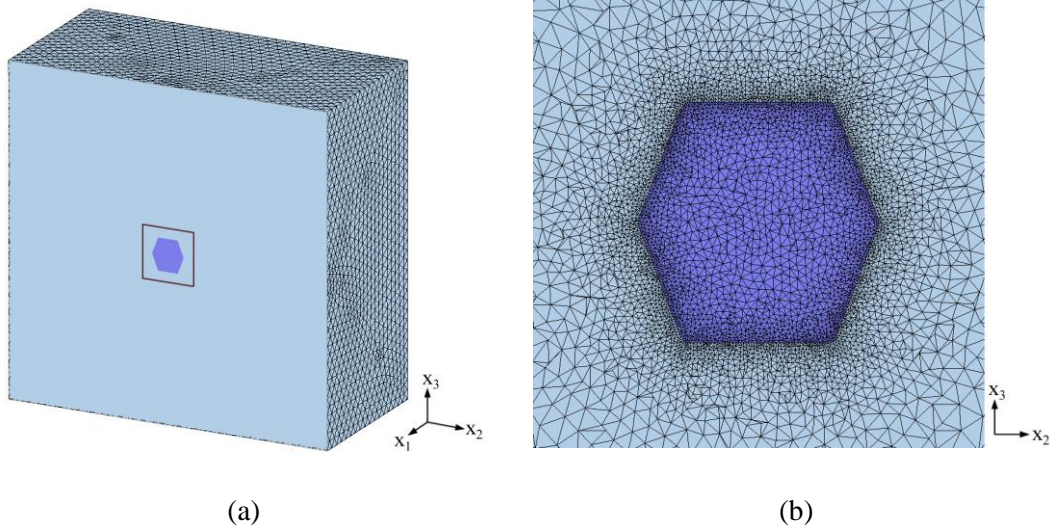
Figure 18. Illustration of the 3D mesh density of the matrix containing an icosahedral particle: a) general view of the reference volume; b) close-up view of the highlighted region

After the volume mesh is generated, the components of the **N**-tensor are found from the set of six load cases: three normal loadings (in the directions of three global coordinate axes) and three shear loadings. The boundary conditions for all six load cases are prescribed in terms of displacements on the faces of the reference volume. Once the six FEA simulations are run, the result files are processed using a custom Python script to determine **N-**tensor. The script starts with calculating the average stress components within the volume for each load case:

$$\langle\sigma_{ij}\rangle_m = \frac{1}{V}\sum_{l=1}^{N_e}\left(\sigma_{ij}^{(l)}\right)_m \cdot V^{(l)}, \quad (i,j = 1,2,3; \quad m = 1,2,\dots,6) \tag{31}$$

<center>58</center>

where $\langle\sigma_{ij}\rangle_m$ is the volume average of the stress component ij calculated from the m-th loadcase, V is the reference volume, $\left(\sigma_{ij}^{(l)}\right)_m$ is the stress component ij at the centroid of the finite element l calculated from the m-th loadcase, $V^{(l)}$ is the volume of the element l, and N_e is the total number of elements in the model. Given the average stress components we then calculate the stiffness contribution tensor from:

$$N_{ijkl}(\varepsilon_{kl}^0)_m = \langle\sigma_{ij}\rangle_m - \left(\sigma_{ij}^0\right)_m, \quad \text{(summation over } k, l = 1,2,3) \tag{32}$$

where $(\varepsilon_{kl}^0)_m$ are the components of the prescribed strain and $\left(\sigma_{ij}^0\right)_m$ are the stress components inside V in the absence of the inhomogeneity. For example, from the first load case all components N_{ij11} are found (note that all ε_{kl}^0 except ε_{11}^0 are zero):

$$N_{ij11} = \frac{\langle\sigma_{ij}\rangle_1 - \left(\sigma_{ij}^0\right)_1}{(\varepsilon_{11}^0)_1}. \tag{33}$$

Components of the stiffness contribution tensors normalized by particle volume fraction, $\overline{N}_{ijkl} = \left(\frac{V}{V_1}\right) N_{ijkl}$, are presented for different shapes in Table 10.

3.3 Stiffness contribution tensors of polyhedral particles

3.3.1 N-tensor components for considered shapes

Table 10 presents non-zero components of the stiffness contribution tensors calculated following the procedure described in section 3.2 for the shapes presented in Table 9. Young's moduli and Poisson's ratios of the matrix and particle materials used in calculations are $E_0 = 1GPa, v_0 = 0.3, \ E_1 = 3GPa, \ v_1 = 0.4$, respectively.

Only three components of the normalized stiffness contribution tensors are

presented for the shapes in the first part of Table 10 because the tensors have equal

components in three directions: $\bar{N}_{1111}^{FEA} = \bar{N}_{2222}^{FEA} = \bar{N}_{3333}^{FEA}$, $\bar{N}_{1122}^{FEA} = \bar{N}_{2233}^{FEA} = \bar{N}_{3311}^{FEA}$ and

$\bar{N}_{1212}^{FEA} = \bar{N}_{2323}^{FEA} = \bar{N}_{3131}^{FEA}$.

Table 10. Stiffness contribution tensor components of the considered shapes

Shape	$\bar{N}_{1111}^{FEA}$	$\bar{N}_{1122}^{FEA}$	$\bar{N}_{1212}^{FEA}$
Sphere	1.5127	0.7701	0.3712
Polyhedral Supersphere 1	1.5216	0.7751	0.3746
Polyhedral Supersphere 1 (smooth)	1.5125	0.7710	0.3720
Polyhedral Supersphere 2	1.5243	0.7769	0.3757
Polyhedral Supersphere 2 (smooth)	1.5161	0.7730	0.3733
Cube	1.5828	0.7837	0.3719
Cube (smooth)	1.5302	0.7685	0.3681
Icosahedron	1.5229	0.7745	0.3739
Truncated Octahedron	1.5230	0.7803	0.3784
Cuboctahedron	1.5393	0.7746	0.3720
Rhombic Dodecahedron	1.5241	0.7815	0.3791
Octahedron	1.5402	0.7934	0.3850
Octahedron (smooth)	1.5217	0.7846	0.3813

Shape	$\bar{N}_{1111}^{FEA}$	$\bar{N}_{1122}^{FEA}$	$\bar{N}_{1212}^{FEA}$	$\bar{N}_{3333}^{FEA}$	$\bar{N}_{1133}^{FEA}$	$\bar{N}_{1313}^{FEA}$
Tetrahedron	1.6222	0.8034	0.3698	1.5829	0.8427	0.4091
Tetrahedron (smooth)	1.5513	0.7780	0.3693	1.5344	0.7948	0.3862

3.3.2 Replacement relations

Replacement relations play an important role in geomechanics in the context of the effect of saturation on seismic properties of rock. This problem was first addressed by Gassmann (1951) who proposed the following relation expressing bulk modulus K of fully saturated rock in terms of the elastic properties of dry rock (see Mavko et al. (2009), Jaeger et al. (2007) for application of these relation in rock mechanics and geophysics):

$$K = K_{dry} + \frac{K_0\left(1 - K_{dry}/K_0\right)^2}{1 - \varphi - K_{dry}/K_0 + \varphi K_0/K_1}, \tag{34}$$

where subscripts "0" and "1" denote elastic constants of the matrix material and material filling the pores, respectively; φ is the volume fraction of the inhomogeneities (porosity for the material with unfilled pores); K_{dry} is the bulk modulus of the porous material of the same morphology. This approach was further developed in the works of Ciz and Shapiro (2007) who obtained relation similar to (34) for shear modulus and (Saxena & Mavko, 2014) who derived replacement relations (they use term "substitution relations") for isotropic rocks containing inhomogeneities of the same shape, but different elastic constants. The latter were obtained under the assumption that strains and stresses inside inhomogeneities are uniform and overall properties and properties of the constituents are isotropic. Replacement relations for the most general case were obtained by (Igor Sevostianov & Kachanov, 2007) in terms of property contribution tensors of inhomogeneities having the same shape but different elastic constants and embedded in the same matrix:

$$\frac{V_1}{V}(\mathbf{N}_A^{-1} - \mathbf{N}_B^{-1}) = (\mathbf{C}_A - \mathbf{C_0})^{-1} - (\mathbf{C}_B - \mathbf{C_0})^{-1} \qquad (35)$$

where $\mathbf{N}_A$ and $\mathbf{N}_B$ are the stiffness contribution tensors of inhomogeneities with material properties A and B, respectively, $\mathbf{C}_A$ and $\mathbf{C}_B$ are the stiffness tensors of particles having material properties A and B, and $\mathbf{C_0}$ is the stiffness tensor of matrix material. (Chen et al., 2017) showed that these relations lead to the following one relating effective properties of a dry porous material and material containing inhomogeneities with material properties A having the same morphology:

$$\mathbf{S}^{NI} = \mathbf{S_0} + \varphi \left[(\mathbf{S}_A - \mathbf{S_0})^{-1} + \varphi (\mathbf{S}_{dry} - \mathbf{S_0})^{-1} \right]^{-1}, \qquad (36)$$

where $\mathbf{S}$ denotes compliance tensor of a material.

For isotropic mixture of the inhomogeneities, (36) yields the following expressions for effective bulk and shear moduli, K and G:

$$
\begin{aligned}
K &= K_0 \frac{\varphi K_{dry}(K_0 - K_A) + K_A(K_0 - K_{dry})}{\varphi K_0(K_0 - K_A) + K_A(K_0 - K_{dry})}, \\[2mm]
G &= G_0 \frac{\varphi G_{dry}(G_0 - G_A) + G_A(G_0 - G_{dry})}{\varphi G_0(G_0 - G_A) + G_A(G_0 - G_{dry})}.
\end{aligned}
\qquad (37)
$$

This relations coincide with ones obtained by Gassmann (1951), Ciz and Shapiro (2007), and Saxena and Mavko (2014). Moreover, relations (37) are independent of the homogenization method: non-interaction approximation, Mori-Tanaka scheme, Maxwell scheme, etc lead to the same results provided that properties of both porous material and composite are calculated by the same method. Chen et al (2017) also showed that replacement relations (35) and (36), being rigorous for inhomogeneities of ellipsoidal shape, can be used as an accurate approximation for non-ellipsoidal convex

superspheres. In this section, we investigate the applicability of the replacement relations to the polyhedral shapes presented in Table 9.

We start with an inhomogeneity A having elastic properties $E_A = 3GPa$, $\nu_A = 0.4$ (see Table 10) and calculate the stiffness contribution tensor for inhomogeneity B of the same shape having elastic properties $E_B = 20GPa$, $\nu_B = 0.2$ using replacement relations (34). Matrix material is the same in both cases with Young's modulus and Poisson's ratio equal to $E_0 = 1GPa$ and $\nu_0 = 0.3$, respectively. Table 11 presents the comparison between stiffness contribution tensors calculated via FEA ($\overline{N}_{ijkl}^{FEA}$) and obtained utilizing the replacement relation ($\overline{N}_{ijkl}^{repl.}$) as described above for all shapes presented in Table 9. The table also contains unsigned relative errors for individual components ($\Delta\overline{N}_{ijkl}$) and Euclidean norm of the absolute error ($\|\mathbf{N}^{FEA} - \mathbf{N}^{repl.}\|$). Additional results for $\nu_0 = 0.2$ and $\nu_0 = 0.4$ are presented in Appendix B. Sphere is a special case of an ellipsoid for which the replacement relation is exact. Therefore, there should be no difference between direct FEA results and $\mathbf{N}$-tensor values obtained via replacement relation in the case of a sphere. As expected relative errors as well as Euclidean norm of the absolute error are zero, see the first row in Table 10. Calculations for other shapes result in non-zero relative errors and error norms with the largest relative error and error norm observed in the case of a tetrahedron.

63

Table 11. Comparison between stiffness contribution tensors calculated FEA directly and obtained utilizing the replacement relation formula

Shape	$\overline{N}_{1111}^{FEA}$	$\overline{N}_{1122}^{FEA}$	$\overline{N}_{1212}^{FEA}$	$\overline{N}_{1111}^{repl.}$	$\overline{N}_{1122}^{repl.}$	$\overline{N}_{1212}^{repl.}$	$\Delta\overline{N}_{1111}$ (%)	$\Delta\overline{N}_{1122}$ (%)	$\Delta\overline{N}_{1212}$ (%)	$\left\|\mathbf{N}^{FEA}-\mathbf{N}^{repl.}\right\|$
Sphere	2.169	0.70	0.7331	2.169	0.701	0.733	0.00	0.00	0.00	0.000
Polyhedral Supersphere 1 (smooth)	2.168	0.704	0.737	2.174	0.705	0.742	0.08	0.01	0.11	0.009
Polyhedral Supersphere 1	2.210	0.704	0.757	2.188	0.705	0.747	1.03	0.20	1.35	0.024
Polyhedral Supersphere 2 (smooth)	2.185	0.704	0.747	2.174	0.705	0.742	0.50	0.08	0.65	0.012
Polyhedral Supersphere 2	2.224	0.705	0.766	2.193	0.707	0.751	1.38	0.26	1.92	0.033
Cube (smooth)	2.240	0.683	0.730	2.226	0.682	0.721	0.50	0.16	1.24	0.016
Cube	2.504	0.662	0.793	2.372	0.667	0.736	5.29	0.75	7.20	0.137
Icosahedron	2.216	0.701	0.756	2.193	0.703	0.744	1.07	0.17	1.65	0.025
Truncated Octahedron	2.213	0.717	0.782	2.183	0.715	0.762	1.34	0.19	2.52	0.033
Cuboctahedron	2.291	0.685	0.756	2.244	0.688	0.737	2.02	0.48	2.56	0.050
Rhombic Dodecahedron	2.218	0.719	0.790	2.184	0.717	0.765	1.54	0.31	3.23	0.039
Octahedron (smooth)	2.204	0.734	0.810	2.172	0.726	0.774	1.45	1.17	4.48	0.049
Octahedron	2.282	0.747	0.861	2.214	0.730	0.789	2.97	2.33	8.42	0.103

Shape	Tetrahedron (smooth)	Tetrahedron
$\overline{N}_{1111}^{FEA}$	2.339	2.754
$\overline{N}_{1122}^{FEA}$	0.694	0.702
$\overline{N}_{1212}^{FEA}$	0.791	0.914
$\overline{N}_{3333}^{FEA}$	2.310	2.644
$\overline{N}_{1133}^{FEA}$	0.723	0.813
$\overline{N}_{1313}^{FEA}$	0.821	1.024
$\overline{N}_{1111}^{repl.}$	2.262	2.432
$\overline{N}_{1122}^{repl.}$	0.670	0.634

Table 11. Continued

$\bar{N}_{1212}^{repl.}$	0.726	0.728
$\bar{N}_{3333}^{repl.}$	2.194	2.262
$\bar{N}_{1133}^{repl.}$	0.738	0.804
$\bar{N}_{1313}^{repl.}$	0.794	0.898
$\max\left(\Delta\bar{N}_{ijkl}(\%)\right)$	8.220	20.35
$\|\mathbf{N}^{FEA} - \mathbf{N}^{repl.}\|$	0.131	0.400

Based on Table 10, it can be concluded that the replacement relation can be applied to most of the considered shapes with very good accuracy (maximum error <5%) except for a cube, octahedron, tetrahedron and a smooth tetrahedron for which the maximum relative errors are higher – 7.2%, 8.4%, 20.4% and 8.2%, respectively. Note that the replacement relation works better for shapes with low values of the parameter p, which has the effect of smoothing of the edges and corners of a shape.

It appears that the errors in the replacement relation predictions are smaller for the shapes resembling a sphere (e.g. smooth polyhedral superspheres) and greater for the shapes different from the sphere (e.g. cube, tetrahedron). The parameter that can be used to measure the "sphericity" of a shape is the ratio $S^{3/2}/V$, where S is the surface area and V is the volume of the shape. Among all possible 3D shapes, a sphere has the minimum surface area for a given volume and the ratio $S^{3/2}/V = 10.63$. Figure 19a presents the Euclidean norm of the absolute error in replacement relation results for different shapes as a function of the surface area-to-volume parameter. Figure 19b presents the Euclidean norm of the absolute difference between the FEA calculated $\mathbf{N}$-

tensors of different shapes and **N**-tensor of a sphere. Two conclusions can be drawn from the figures: a) the error norm increases linearly with the parameter $S^{3/2}/V$; and b) the error norms in Figure 19b are almost half of the error norms in Figure 19a for the corresponding shapes. The latter conclusion indicates that the replacement relation (35) results in a better N-tensor approximation for a given inhomogeneity shape and elastic properties combination compared to a simple replacement of the shape with a sphere.
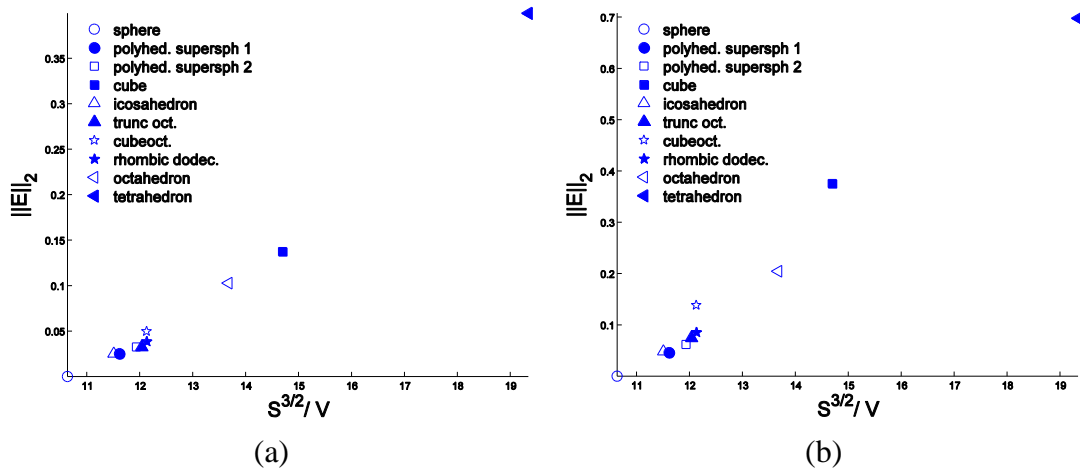
Figure 19. Effect of the surface area-to-volume ratio of a shape on the Euclidean norm of the absolute error: (a) between N-tensors of the polyhderal shapes from Table 9 calculated via FEA and replacement relations; (b) between N-tensors of the polyhedral shapes from Table 9 calculated via FEA and N-tensor of a sphere

3.4   Effective elastic properties

In this section, we use N-tensors of individual shapes to estimate effective elastic moduli of materials containing randomly oriented inhomogeneities of the same

shape. We focus on five shapes – polyhedral supersphere 1, rhombic dodecahedron, icosahedron, cuboctahedron and octahedron.

3.4.1 Analytical homogenization based on N-tensor

To characterize contribution of multiple particles to the effective elastic properties a homogenization procedure based on $\mathbf{N}$-tensor is used. The effective stiffness tensor of the material with particles is given by

$$\mathbf{C} = \mathbf{C_0} + \Delta \mathbf{C}_{\text{RVE}} \tag{38}$$

where $\mathbf{C_0}$ is the stiffness tensor of the matrix material and $\Delta \mathbf{C}_{\text{RVE}}$ is the collective contribution of all particles to the overall stiffness of the representative volume element.

The non-interaction scheme provides a reasonably good approximation for a dilute distribution of particles, and $\Delta \mathbf{C}_{\text{RVE}}$ in this case is obtained by direct summation of contributions from all individual particles in the RVE:

$$\Delta \mathbf{C}_{\text{RVE}}^{\text{NI}} = \sum_i \mathbf{N}_{(i)}, \tag{39}$$

where $\mathbf{N}_{(i)}$ is the stiffness contribution tensor of the i-th particle. The procedure for calculation of stiffness contribution tensors of individual particles is presented in section 3.2.

For higher volume fractions when interaction between particles is significant and the non-interaction approximation is no longer applicable, more advanced micromechanical schemes should be used. One of the most widely used is the Mori-Tanaka scheme, proposed in (Mori & Tanaka, 1973) and clarified in (Benveniste,

1987a). Following this approximation the combined contribution of all particles to the overall stiffness of the RVE is given by

$$\Delta \mathbf{C}_{RVE}^{MT} = \Delta \mathbf{C}_{RVE}^{NI} : \left[\varphi(\mathbf{C_1} - \mathbf{C_0}) + \Delta \mathbf{C}_{RVE}^{NI} \right]^{-1} : (\mathbf{C_1} - \mathbf{C_0}) \tag{40}$$

where φ is the volume fraction of particles and $\mathbf{C_1}$ is the stiffness tensor of the inhomogeneity material.

Alternatively, $\Delta \mathbf{C}_{RVE}$ may be found using Maxwell's homogenization scheme ((Maxwell, 1873; McCartney & Kelly, 2008; Igor Sevostianov, 2014)):

$$\Delta \mathbf{C}_{RVE}^{Maxwell} = \left\{ \left[\Delta \mathbf{C}_{RVE}^{NI} \right]^{-1} - \mathbf{P}_\Omega \right\}^{-1} \tag{41}$$

where $\mathbf{P}_\Omega$ is the Hill's tensor ((Hill, 1965; Walpole, 1969)) for the "effective inclusion" of shape Ω. In our study we consider randomly oriented inhomogeneities and therefore the effective inclusion is of spherical shape.

In the framework of non-interaction approximation, contributions from randomly oriented particles of the same shape to the effective bulk and shear moduli can be calculated using the relationship presented in (T. Te Wu, 1966):

$$\frac{K}{K_0} = 1 + \varphi \widetilde{K} \frac{K_0 - K_1}{K_0}, \quad \frac{G}{G_0} = 1 + \varphi \, \widetilde{G} \frac{G_0 - G_1}{G_0}, \tag{42}$$

$$\widetilde{K} = \frac{T_{iijj}}{3}, \quad \widetilde{G} = \frac{3T_{ijij} - T_{iijj}}{15} \quad \text{(summation over } i, j = 1,2,3), \tag{43}$$

where K_o and G_o are bulk and shear moduli of the matrix material, K_1 and G_1 are bulk and shear moduli of the inhomogeneity material, $\mathbf{T}$ is the Wu's strain concentration tensor related to $\mathbf{N}$-tensor and stiffness tensors $\mathbf{C_0}$ and $\mathbf{C_1}$ as $\mathbf{T} = (\mathbf{C_1} - \mathbf{C_0})^{-1} : \mathbf{N}$ ((Igor Sevostianov & Kachanov, 2007)).

Relations for the effective bulk and shear moduli following Mori-Tanaka scheme can be represented as follows (Benveniste (1987a)):

$$\frac{K}{K_0} = 1 + \varphi \widetilde{K} \frac{K_1 - K_0}{K_0[(1-\varphi)+\varphi \widetilde{K}]}, \quad \frac{G}{G_0} = 1 + \varphi \widetilde{G} \frac{G_1 - G_0}{G_0[(1-\varphi)+\varphi \widetilde{G}]}, \tag{44}$$

Finally, for the Maxwell scheme we have:

$$\frac{K}{K_0} = \frac{E}{3K_0(1-2\nu)}, \quad \frac{G}{G_0} = \frac{E}{2G_0(1+\nu)}, \tag{45}$$

where E and ν are the effective Young's modulus and Poisson's ratio that can be calculated from the effective stiffness tensor components, see (38).

3.4.2 FEA of periodic representative volume elements

To generate RVEs containing multiple non-intersecting particles we use a custom script utilizing a simplified implementation of the collective rearrangement method based on Altendorf and Jeulin (2011) and detailed in Drach et al. (2016). The script results in a fully periodic surface mesh of non-intersecting particles. The RVE surface mesh is imported into a MSC Marc/Mentat for further numerical analysis. All FEA model preparation steps at this stage are performed automatically using a custom script that provides a ready-to-run model upon completion. The final RVE is meshed with the 10-node tetrahedral 3D elements. Figure 20 illustrates two examples of generated microstructures.

Since RVEs generated to have a congruent mesh of the opposite faces we treat them as unit cells and subject them to periodic boundary conditions. The boundary

conditions for two corresponding nodes on the opposite (positive and negative) faces are introduced similarly to (Segurado and Llorca (2002)):

$$u_j^{(i+)} = u_j^{(i-)} + \delta_j, \quad (j = 1,2,3) \tag{46}$$

where $u_j^{(i+)}$ and $u_j^{(i-)}$ are displacements in x_j direction of the i-th node on the positive and negative faces respectively; and δ_j is the prescribed average displacement in the x_j direction.

(a)   (b)
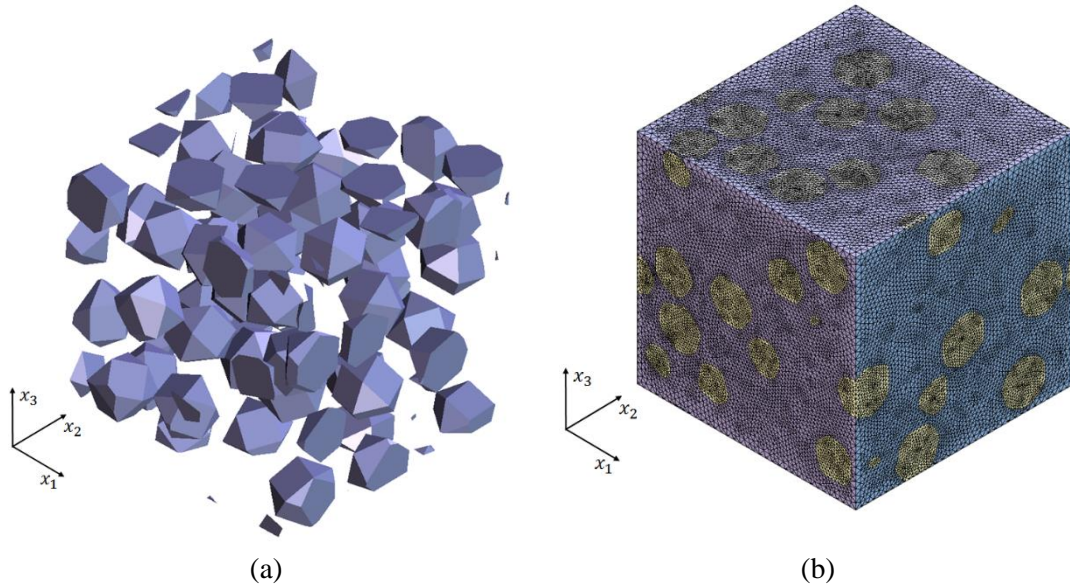
Figure 20. Illustration of generated RVEs: (a) packed cuboctahedral particles, volume fraction $\varphi = 0.2$: (b) final RVE with polyhedral particles, volume fraction $\varphi = 0.2$

Periodic boundary conditions were implemented in MSC Marc/Mentat using the "servo-link" feature (see, for example, (A. Drach et al., 2014; Borys Drach et al., 2016; MSC Software, 2012)). Servo-links allow to prescribe multi-point boundary conditions for nodal displacements in the form of a linear function with constant coefficients. In

this formulation, δ_j-s are implemented as translational degrees of freedom of control nodes, which are linked to the nodes on the corresponding opposite faces of an RVE. To constrain rigid body displacements, a node inside the RVE is fixed. Rigid body rotations are not allowed by the periodic boundary conditions, so additional constraints are not required.

Six sets of boundary conditions are applied in terms of displacements to simulate three uniaxial tension and three shear load cases. Note that the prescribed strains are set to 0.001 to ensure small deformations so that the initial element volumes could be used in the volume averaging procedure described below. Figure 21 presents the stress distribution within the RVE subjected to the uniaxial tension along one of the global coordinate axis. Once the numerical simulations are performed, the result files are processed using a custom Python script to calculate effective elastic properties of the RVE. First, volume-averaged stress components are calculated for each load case. Given the averaged stress components and applied strain, we calculate the effective stiffness tensor using Hooke's law:

$$C_{ijkl}^{eff}(\varepsilon_{kl}^0)_m = \langle\sigma_{ij}\rangle_m, \tag{47}$$

where $\langle\sigma_{ij}\rangle_m$ and $(\varepsilon_{kl}^0)_m$ are the volume-averaged stress and applied strain components, respectively, and m is the load case number. For example, from the second load case we can calculate all C_{ij22}^{eff} components:

$$C_{ij22}^{eff} = \frac{\langle\sigma_{ij}\rangle_2}{(\varepsilon_{22}^0)_2}. \tag{48}$$

71

Engineering constants are then obtained from the effective compliance tensor.
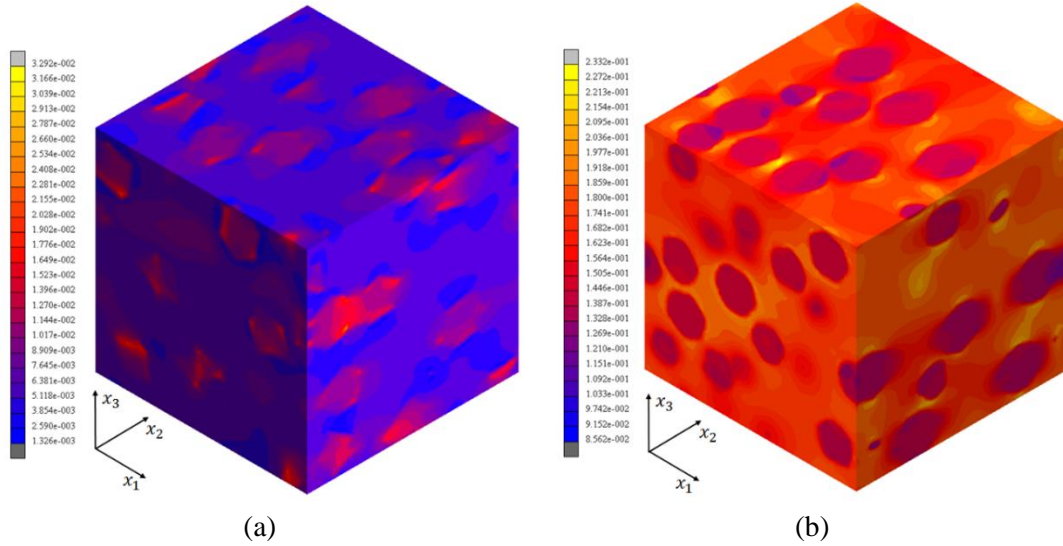
Figure 21. Distribution of σ_{11} stress component (GPa) within an RVE subjected to uniaxial tension along x_1 direction: (a) matrix material with $E_0 = 120\ GPa$ and $\nu_0 = 0.34$, polyhedral supersphere particles with $E_1 = 70\ GPa$ and $\nu_1 = 0.35$, volume fraction $\varphi = 0.2$; (b) matrix material with $E_0 = 2.89\ GPa$ and $\nu_0 = 0.35$, cuboctahedral particles with $E_1 = 79\ GPa$ and $\nu_1 = 0.4$, volume fraction $\varphi = 0.2$

3.5   Results

Effective bulk (K) and shear (G) moduli of materials containing five types of particles selected from Table 9 (polyhedral supersphere 1, rhombic dodecahedron, icosahedron, cuboctahedron and octahedron) were approximated using non-interaction, Mori-Tanaka and Maxwell homogenization schemes based on numerically calculated **N**-tensors for individual particles. Table 12 presents elastic properties of the matrix and inhomogeneity material that were used in homogenization. The results were compared to FEA simulations performed on RVEs containing 50 particles each (see section 3.4.2) with volume fractions of $\varphi = 0.10, 0.15, 0.20$ for the octahedral shape and

0.10, 0.20, 0.30 for all others. For each microstructure five RVE realizations were generated. Each realization is shown as a separate data point. All results are presented in Figure 22. Good correspondence between FEA simulations and Mori-Tanaka and Maxwell schemes is observed with the latter being a little closer to the direct FEA, see Figure 22a-e. From Figure 6a it can be concluded that Maxwell and Mori-Tanaka schemes produce almost identical predictions, since polyhedral supersphere 1 is very close to the spherical shape for which Maxwell and Mori-Tanka schemes coincide.

Table 12. Material properties of considered microstructures.

Particle shape	Matrix material		Particle material	
	E_0, GPa	ν_0	E_1, GPa	ν_1
polyhedral supersphere 1	120	0.34	70	0.35
rhombic dodecahedron	70	0.17	3.5	0.44
icosahedron	2.5	0.34	83	0.37
cuboctahedron	2.89	0.35	79	0.4
octahedron	2.89	0.35	1050	0.1

Note that with increasing elastic contrast between the matrix and the particles, correlation between homogenization schemes and direct FEA decreases. The greatest elastic contrast considered in this paper (~360) was used for the material with octahedral particles (Figure 22e). The maximum relative error between the Maxwell scheme and direct FEA in this case is observed in shear modulus predictions and is equal to 2.5%.

73
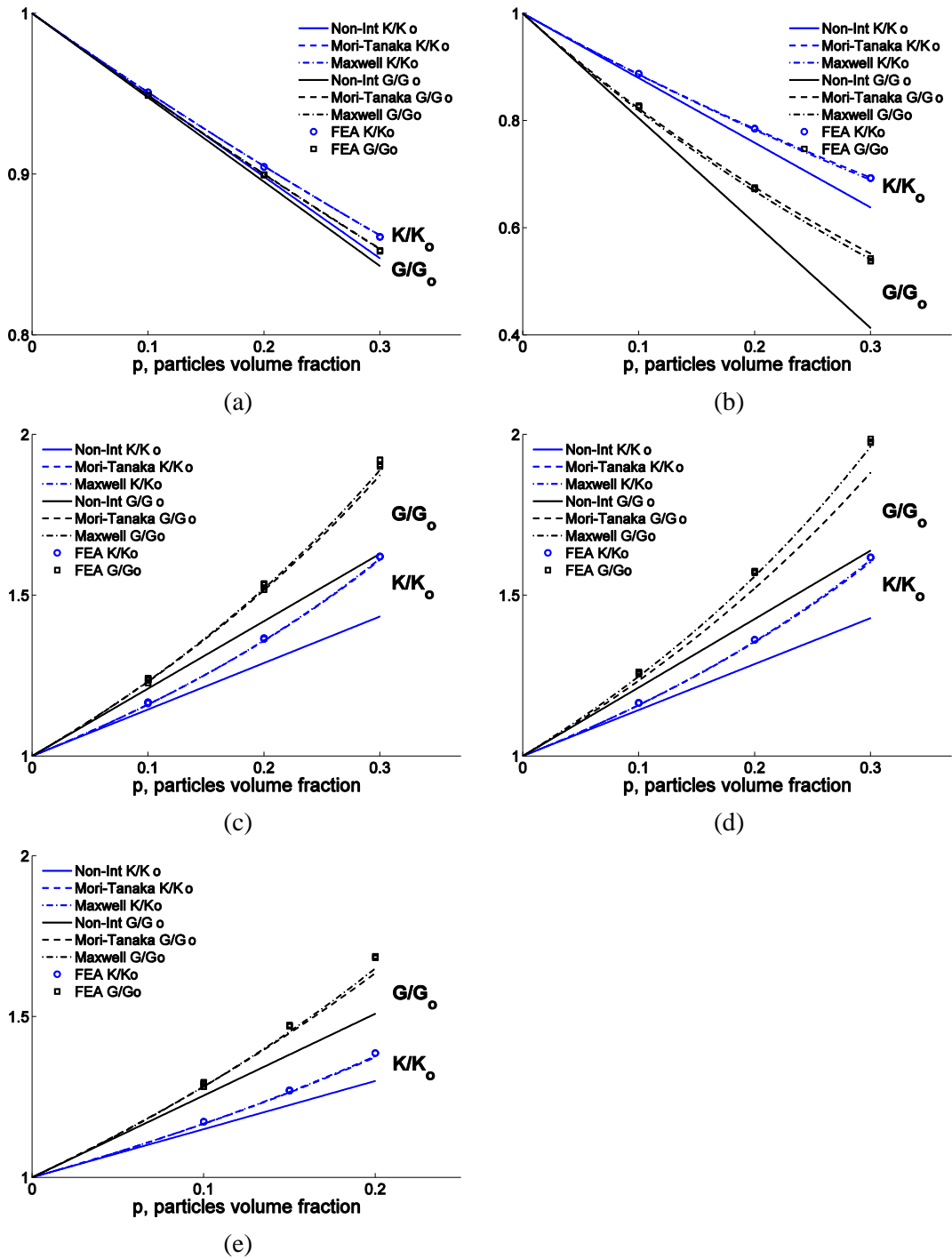
Figure 22. Effective elastic properties of materials containing randomly oriented particles of different shapes: a) polyhedral supersphere 1 (smooth); b) rhombic dodecahedron; c) icosahedron; d) cuboctahedron; e) octahedron

The replacement relationship discussed in section 3.3.2 interrelates contributions of inhomogeneities having the same shape but different elastic constants to the overall elastic properties. This allows extending results presented in section 3.3.1 and Appendix B to combinations of matrix/particle properties not discussed in the paper. Here we investigate the accuracy of K and G predictions based on the replacement relation for materials containing randomly oriented octahedral, cubical, and tetrahedral particles. The predictions were obtained using Maxwell homogenization scheme based on N-tensors of polyhedral particles estimated using the relation (35). First, we obtained N-tensor components of the individual shapes for $E_0 = 1, \nu_0 = 0.33, E_1 = 20$ and $\nu_1 = 0.2$ by interpolating the components for $\nu_0 = 0.3$ and $\nu_0 = 0.4$ presented in Table 4 and Appendix A, respectively. Then, we applied the replacement relation (35) to estimate the N-tensor components for $E_0 = 1, \nu_0 = 0.33, E_1 = 10$ and $\nu_1 = 0.1$, and used the result to predict effective bulk and shear moduli for $\varphi = 0.2$. The predictions are compared to the FEA results for periodic RVEs published in (Rasool & Böhm, 2012) and presented in Table 6. Note that the moduli K_{RB} were calculated based on the effective Young's moduli and Poisson's ratios from Table 3 in (Rasool & Böhm, 2012) because we believe the authors made a mistake in their calculations of the effective bulk moduli in the paper.

From the analysis of Table 13 we conclude that Maxwell scheme in combination with the replacement relation (3.2) provide very good estimates for the effective bulk

75

moduli of all three shapes (relative error <1%) and good predictions for the effective

shear moduli except for a cube (relative error of 6.14%).

Table 13. Comparison of effective bulk and shear moduli predictions for materials containing randomly oriented particles of octahedral, cubical and tetrahedral shapes ($\varphi = 0.2$) based on the replacement relation (35) with numerical calculations presented in (Rasool & Böhm, 2012)

Particle shape	(Rasool & Böhm, 2012)		Our predictions		Unsigned rel. error, %	
	K_{RB}	G_{RB}	K	G	$\Delta K\%$	$\Delta G\%$
Octahedron	1.2478	1.4790	1.2542	1.4504	0.51	1.93
Cube	1.2626	1.4660	1.2569	1.5620	0.45	6.14
Tetrahedron	1.2708	1.5290	1.2804	1.5897	0.75	3.82

In addition, we looked at the performance of the replacement relation in two

extreme cases – when **N**-tensors of elastic particles are estimated from **N**-tensors of

pores and from N-tensors of perfectly rigid particles. We began by calculating **N**-

tensors for pores ($E_1 = 0$) and perfectly rigid inhomogeneities ($E_1 \rightarrow \infty$) for the five

shapes discussed above (polyhedral supersphere 1, rhombic dodecahedron,

icosahedron, cuboctahedron and octahedron), then used the results to calculate **N**-

tensors for elastic properties from Table 12 via the replacement relation. Stiffness

contribution tensor components for the five particles having $E_1 = 0\ GPa$ and $E_1 = $

$10^6\ GPa$ are presented in Table 14.

Finally, we estimated the effective bulk (K) and shear (G) moduli using

Maxwell homogenization scheme. The results are compared with direct FEA

simulations and effective elastic properties of RVEs containing spheres, and presented

in Figure 22.

Table 14. Stiffness contribution tensor components for soft and rigid particles of the following shapes: polyhedral supersphere 1, rhombic dodecahedron, icosahedron, cuboctahedron and octahedron

Shape	Rigid, $E_1 = 10^6\ GPa$			Pore, $E_1 = 0\ GPa$		
	$\overline{N}_{1111}^{rigid}$	$\overline{N}_{1212}^{rigid}$	$\overline{N}_{1122}^{rigid}$	$\overline{N}_{1111}^{pore}$	$\overline{N}_{1212}^{pore}$	$\overline{N}_{1122}^{pore}$
polyhedral supersphere1, $E_0 = 120\ GPa, \nu_0 = 0.34$	315.380	98.331	120.661	-508.577	-84.157	-337.858
rhombic dodecahedron, $E_0 = 70\ GPa, \nu_0 = 0.17$	160.279	65.072	37.215	-157.868	-62.719	-28.168
icosahedron, $E_0 = 2.5\ GPa, \nu_0 = 0.34$	6.717	2.102	2.504	-10.772	-1.786	-7.207
cuboctahedron, $E_0 = 2.89\ GPa, \nu_0 = 0.35$	8.285	2.428	3.007	-13.994	-2.158	-10.051
octahedron, $E_0 = 2.89\ GPa, \nu_0 = 0.35$	8.177	3.292	2.977	-15.182	-2.326	-10.820

From the examination of the Figure 23a andFigure 23b it can be concluded that in the case

of soft inhomogeneities, Maxwell scheme in combination with **N**-tensor obtained from

the replacement relation based on a pore provides a good correlation with direct FEA

results. On the other hand, for stiff inhomogeneities, Maxwell scheme predictions with

N-tensor obtained from the replacement relation based on a perfectly rigid particle

result in a better agreement with direct FEA calculations, see Figure 23c-e. Comparing

the predictions for the effective moduli from spheres with direct FEA results indicates

that the effective shear modulus is more sensitive to the shape of inhomogeneitis than

the effective bulk modulus. In addition, the results show that predictions obtained from

the replacement relation work better than approximations by spheres.
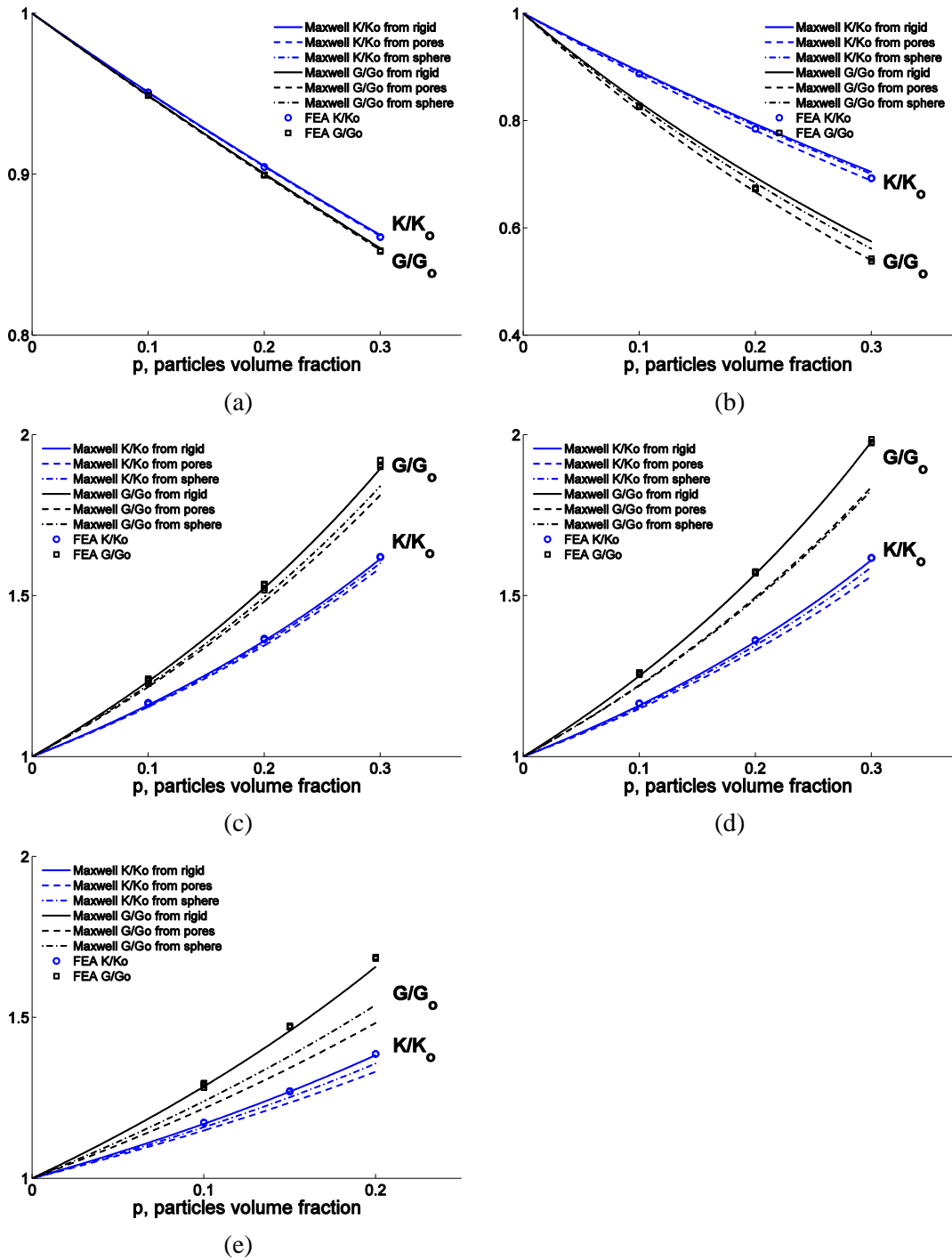
Figure 23. Effective elastic properties estimated via Maxwell scheme and N-tensors based on the replacement relation of materials containing randomly oriented particles of different shapes: a) polyhedral supersphere1; b) rhombic dodecahedron; c) icosahedron; d) cuboctahedron; e) octahedron

3.6 Discussions and conclusions

Stiffness contribution tensors (N-tensors) of 15 convex polyhedra were calculated using Finite Element Analysis and presented in this paper. The N-tensor components of these shapes were analyzed to determine whether the tensors were isotropic or exhibited cubic symmetry. As expected, a sphere was confirmed to be isotropic; polyhedral superspheres were found to be nearly isotropic; and a cube, truncated octahedron, cuboctahedron, rhombic dodecahedron and octahedron were concluded to have cubic symmetry. The applicability of the replacement relation that interrelates stiffness contribution tensors of inhomogeneities having the same shape but different elastic properties to the considered shapes was investigated. It was found that the replacement relation can be used with good accuracy (<5% maximum relative error) for most of the considered shapes except for a tetrahedron, octahedron, cube and smooth tetrahedron for which the maximum relative errors were considerably higher. Application of the replacement relation to a tetrahedron resulted in the largest relative error of 20.4% among all considered shapes. Note that the replacement relation works better for shapes with low values of the parameter p, which has the effect of smoothing of the edges and corners of a shape. We also observed a correlation between the accuracy of the replacement relation and the sphericity shape parameter – the Eucledian norm of the difference between N-tensor calculated via replacement relation and N-tensor obtained from direct FEA increases linearly with sphericity. Similar correlation was observed for the Eucledian norm of the difference between the N-tensor of a polyhedral particle and its approximation by a sphere.

79

We used N-tensors of individual polyhedra to calculate overall elastic properties of materials containing multiple randomly oriented polyhedral particles via micromechanical homogenization based on non-interaction approximation, Mori-Tanaka and Maxwell schemes. The results were compared with direct FEA calculations performed on periodic RVEs. Good correspondence between FEA simulations and Mori-Tanaka and Maxwell schemes up to volume fractions of 30% was observed with Maxwell scheme being a little closer to direct FEA. FEA results were also compared with effective properties calculated using Maxwell scheme and the replacement relation based on perfectly rigid particles and pores. We observed that in the cases when particle material is stiffer than the matrix, the replacement relation based on perfectly rigid particles results in good predictions for effective elastic properties. Conversely, in the cases when particles are softer than the matrix, the replacement relation based on pores produces better estimates for the overall elastic properties.

Combination of N-tensor components presented in this paper for different values of matrix Poisson's ratio (see Table 11 and Appendix B) with the replacement relation (35) can be used to estimate stiffness contribution tensors of polyhedral particles for any set of particle/matrix elastic properties. The estimate will have a particularly good accuracy in the cases when particles are stiffer than the matrix because Table 11 and Appendix B results were obtained for stiff particles. For a combination in which the particle material is softer than the matrix, approximation of the shape by a sphere might result in a better estimate than the one obtained from the replacement relation based on a stiff particle.

4.0   HOMOGENIZATION OF MATERIALS WITH CRACK WITH AN "ISLAND" OF A PARTIAL CONTACT

Abstract. Compliance and resistivity contribution tensors of a penny-shaped crack having a partial contact of arbitrary location along crack faces are found, in terms of contact size and its distance from the center. This result is a first step towards modeling of "rough" cracks having contacts between crack faces. Being applied to multiple cracks, our results yield the "adjusted", for the presence of contacts, value of crack density in terms of contact parameters. Similar results are obtained in the context of conductivity.

4.1   Introduction

Cracks having partial contacts between crack faces are common in various materials. Clarke, 1921 observed cracks of annular geometries in metal castings. Cai et al. (2011) reported formation of annular cracks in human femur cortical bone during radial fretting. Kudinov (1977) reported formation of the flat annular pores in plasma-spraying process and evaluated relative size of the island of contact. Bhowmick et al. (2007) observed cracks of similar geometry occurring in silicon subjected to fatigue contact loading. Figure 24 provides illustrations.

A partial contact between crack faces significantly "stiffens" the crack, even if the contact is small. This was discussed by Todoroki et al. (1988) in the context of fatigue cracks who noted that ignoring the contacts produces incorrect estimates of the fatigue life. Yet another aspect of the problem is that, due to the "stiffening" effect on

cracks, the presence of partial contacts makes detection of a crack more difficult, as experimentally observed by Buck et al. (1983).
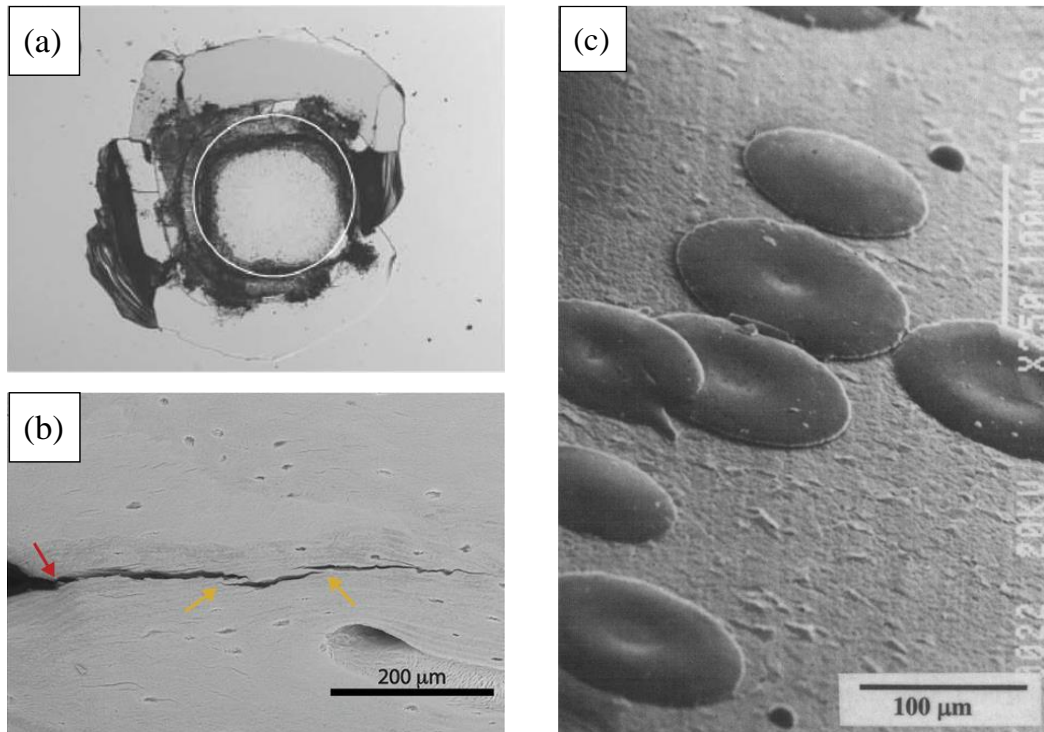
Figure 24. (a) Optical micrographs of contact damage in silicon (100) from cyclic loading of spherical indenter at P=250N, n=85x10^3 cycles (from Bhowmick et al., 2007); (b) SEM image of a crack in human cortical bone having uncracked segments ("islands" of uncracked material) indicated by arrows (from Zimmermann et al. (2015)); (c) Pancake-like splats observed in the process of plasma spraying of Al$_2$O$_3$ powder. The edge and the central part of splat are in contact with the lower layer while the ring-like area in-between forms a crack (from Fan et al. (1998))

The first step to analysis of cracks with contacts is to examine the effect of one contact; in other words, to analyze a crack of the annular geometry (with an "island" of partial contact). Most of the available quantitative results have dealt with the axisymmetric geometry (centrally located "island") under tension, and focused on calculation of the stress intensity factors (SIF). This problem can be reduced to integral

equations of various types. The first approximate solution for K_I was obtained by Grinchenko and Ulitko (1965) by the method of iterations. The analysis given by Smetanin (1968) for K_I at both external and internal edges uses an asymptotic method. Moss and Kobayashi (1971) used the technique proposed by Mossakovski and Rybka (1964) to develop iterative approximate solutions for elastic fields. The analysis of the annular crack problem presented by Shibuya et al. (1975) employs a technique whereby the governing integral equations are reduced to an infinite system of algebraic equations. Choi and Shield (1981) solved the axisymmetric problems of an annular crack subject to torsional and axial loads; they used Betti theorem to derive the governing integral equations and solved the problem in terms of Fredholm integral equation with kernel having the logarithmic singularity. They also estimated accuracy of the results of Smetanin (1968) and Moss and Kobayashi (1971). Selvadurai and Singh (1985) obtained series solution for a system of triple integral equations and calculated K_I at both edges of the annular crack. They also compared the SIFs derived by other methods. Nied (1981) and Nied and Erdogan (1983) formulated the problem in terms of a system of singular integral equations and solved it numerically. Clements and Ang (1988), solving the same problem, obtained a pair of uncoupled Fredholm integral equations with simple continuous and bounded kernels and solve them by the method of iterations. They also provided comparison of their results with ones of Selvadurai and Singh (1985) and Nied (1981). Korsunsky and Hills (2005) developed a technique employed a one-dimensional integral equation approach to calculate the

SIFs at the edges of an arbitrarily shaped crack lying on a surface of revolution and subject to an arbitrary axisymmetric stress field. They used this technique to calculate K_I at the inner and outer edges of the annular crack. Their result coincides with one of Smetanin (1968). Asadi et al. (2009) obtained K_I for the system of multiple coaxial annular cracks, with particular attention paid to the case of two cracks. Note that all these results produced by different methods are close to one another.

Beom and Earmme (1993) considered shear loading of the annular crack. Using Hankel transform to reduce the problem to a pair of triple integral equations, they solved them numerically and obtained results for K_{II} and K_{III} under four different distribution of the shear load: uniform radial shear, linearly varying radial shear, uniform shear and linearly varying shear. Note that under the uniform shear, the variation of K_{II} and K_{III} along the crack edges has the same angular dependence as the one for a penny-shaped crack.

Sevostianov (2003) numerically evaluated the effect of the annular crack on the effective resistivity (thermal or electrical). Recently, Glubokovskikh et al. (2016)used this approach, as well as the result on compliance of contacting rough surfaces (Sevostianov and Kachanov (2008a, b) to finding the effective normal compliance of finite cracks with contacting surfaces; they also provided comparison with experimental data.

All the above-mentioned works assumed that the partial contact is located at the center of the crack – an assumption that is overly restrictive for applications. The

present chapter, analyzes, numerically, arbitrarily located contacts, and evaluates their stiffening effect as a function of the contact size and location, under both normal and shear loads. The obtained numerical results are verified by comparison with the ones obtained analytically in the special case of centrally located island. The results are then applied to the case of multiple cracks to evaluate the "effective" crack density adjusted for the presence of contacts. Similar analyses are also given in the context of conductivity.

4.2   Hypothesis to be verified

As seen from photomicrographs of Figure 24, partial contacts between crack faces typically have irregular geometry and locations. For the possibility to extend the obtained results to irregular geometries, we formulate the following hypothesis, to be verified in the text to follow:

(A) The stiffening effect of a contact obviously increases for contacts located closer to the crack center. We hypothesize that this dependence is characterized by the function $\sqrt{1 - d^2/a^2}$ (Figure 25) where d is the distance of contact center from the center of the crack and a is the crack radius, i.e. the stiffening effect follows the elliptical profile of the crack in absence of the contact;

(B) In the problem of effective elastic properties of cracked materials, important role is played by closeness of the normal B_N and shear B_T compliances of a crack (the average normal and shear discontinuities induced by uniform unit normal and shear tractions, respectively): this allows one to characterize the

crack density by second-rank crack density tensor, implying orthotropy for an arbitrary orientation distribution of cracks Kachanov (1992). For a circular crack the two compliances differ by factor $1 - \nu/2$. We hypothesize that this ratio is approximately preserved for a crack with a partial contact. In the case of off-center location of the contact, the shear compliance of the crack depends on the direction of the shear in the crack plane. In this case, we hypothesize that the ratio B_T/B_N still holds provided B_T is replaced by the average, $\langle B_T \rangle$, over shear directions.
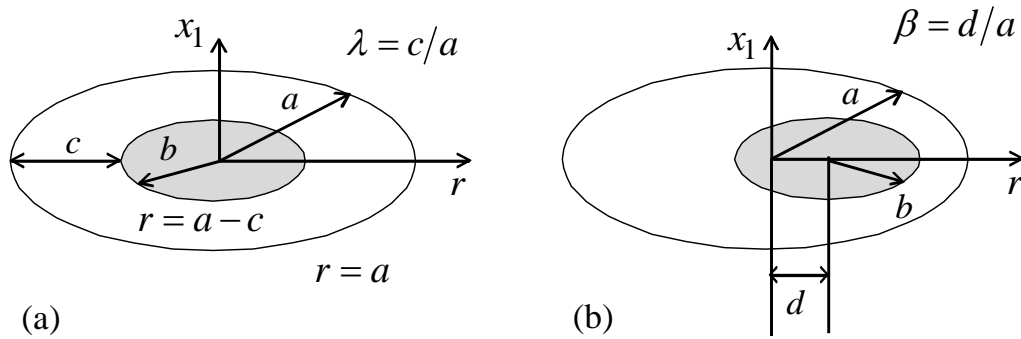
Figure 25. The configurations of a crack with an island of cohesion: (a) centrally located island; (b) off-center island

4.3   Background results: property contribution tensors

The compliance contribution tensors have been first introduced in the context of ellipsoidal pores and cracks in isotropic material by Horii and Nemat-Nasser (1983). For the general case of ellipsoidal inhomogeneities (isotropic and anisotropic)

embedded in an isotropic matrix, these tensors were defined and calculated by Sevostianov and Kachanov(1999, 2002); for other physical properties, the property contribution tensors were introduced by Kachanov and Sevostianov (2005).

We consider a homogeneous material (the matrix) having compliance tensor $\mathbf{S_0}$ and resistivity $\mathbf{r_0}$ and containing an inhomogeneity of volume V_1, of compliance $\mathbf{S_1}$ and resistivity $\mathbf{r_1}$. We assume that both materials satisfy are linearly elastic and linearly conductive, i.e. satisfy the Hooke's Hooke's law $\varepsilon_{ij} = S_{ijkl}\sigma_{kl}$ and Fourier's law $T_{,i} = r_{ij}q_j$, where ε_{ij} is (infinitesimal) elastic strain tensor, σ_{kl} is stress tensor, T is temperature and q_j is heat flux vector.

Remark. Instead of thermal conductivity problem, electric conductivity may be considered. Then, temperature has to be replaced by electric potential, heat flux density – by electric current density, and Fourier's law – by Ohm's law.

The compliance contribution tensor of an inhomogeneity is a fourth-rank tensor $\mathbf{H}$ that gives the extra strain (per reference volume V) due to its presence:

$$\Delta\boldsymbol{\varepsilon} = \frac{V_1}{V}\mathbf{H}{:}\boldsymbol{\sigma}^0, \qquad \text{or, in components, } \Delta\varepsilon_{ij} = \frac{V_1}{V}H_{ijkl}{:}\sigma_{kl}^0 \qquad (49)$$

where σ_{kl}^0 are remotely applied stresses that are assumed to be uniform within V in the absence of the inhomogeneity. For a circular crack, of radius a,

$$\frac{V_1}{V}H_{ijkl} = \frac{8(1-\nu_0)}{3G_0}\frac{a^3}{V}\left\{n_i n_j n_k n_l + \frac{\theta_{ik}n_l n_j + \theta_{il}n_k n_j + \theta_{jk}n_l n_i + \theta_{jl}n_k n_i}{2(2-\nu_0)}\right\} \qquad (50)$$

where n_i is the unit vector along the axis of spheroid symmetry and $\theta_{ik} = \delta_{ij} - n_i n_j$.

Similar approach can be applied for to the problem of conductivity (electrical or thermal) of a material containing an inhomogeneity. The change in ∇T required to maintain the same heat flux density if the inhomogeneity is introduced is:

$$\Delta(\nabla T) = \frac{V_1}{V} \mathbf{R} \cdot \mathbf{q} \tag{51}$$

where the symmetric second-rank tensor $\mathbf{R}$ is called the resistivity contribution tensor of an inhomogeneity. In the limit of strongly oblate perfectly insulating spheroid – the case relevant for a crack (provided the conductance across the crack through air is neglected),

$$\frac{V_1}{V} \mathbf{R} = \frac{1}{k_0} \frac{8a^3}{3V} \mathbf{nn} \tag{52}$$

4.4 Crack with a central contact: compliance and resistivity contribution tensors

The internal variable technique of Rice (1975) allows one to obtain compliance contributions H_{ijkl} of cracks of various geometries for which SIFs are available, by observing that the increment of the overall compliance dS_{ijkl} of volume V due to incremental propagation ΔA of crack front L is given by

$$dS_{ijkl} = \frac{1}{V} \frac{1}{4} \int_{\Delta A} \beta_{qr} \frac{\partial K_q}{\partial \sigma_{ij}} \frac{\partial K_r}{\partial \sigma_{kl}} dA \tag{53}$$

In the case of the isotropic matrix, there is no coupling between mode I, II and III at the crack tip so that

$$\beta_{ij} = \frac{8(1 - v^2)}{E} \begin{bmatrix} 1 & 0 & 0 \\ 0 & 1 & 0 \\ 0 & 0 & \frac{1}{1-v} \end{bmatrix} \tag{54}$$

We now treat the crack as having grown from an infinitesimal nucleus to its current geometry. Then components of the compliance contribution of the crack are given by integration over the growth path $\int dS_{ijkl} = \frac{V_1}{V} H_{ijkl}$ provided SIFs along the growth path are known; if they are available in numerical form, they can often be approximated by simple analytical expressions leading to approximate explicit formulas for the crack compliance contribution.

Results for SIFs K_I- K_{III} and heat flux intensity factor K_T (see, Sevostianov (2006)) at the outer edges of an annular crack are given in the form

$$K_I = \sigma_{11}\sqrt{\pi a}F_1(\lambda)$$

$$K_{II} = \sigma_{13}\sqrt{\pi a}F_2(\lambda)\sin(\theta)$$

$$K_{III} = \sigma_{13}\sqrt{\pi a}F_2(\lambda)(1 - v_0)\cos(\theta) \tag{55}$$

$$K_T = q_1\sqrt{\pi a}F_T(\lambda)$$

where σ_{ij} and q_i are components of stress tensor and heat flux vector, respectively, $\lambda = c/a$ and functions $F_{1,2}(\lambda)$, as taken from Choi and Shield (1981) and Beom and Earmme (1993), for the outer edge are shown in Figure 26a. Note that $F_2(\lambda)$ depends on the Poisson's ratio of the material. As seen in Figure 26b the following formula holds with good accuracy

89

$$F_2(\lambda) = \frac{2}{2 - \nu_0\sqrt{\lambda}} F_1(\lambda) \tag{56}$$

In the limiting case of a penny-shaped crack without the island ($\lambda = 1$), exact relation

between $F_1(\lambda)$ and $F_2(\lambda)$ is recovered (see, for example, Murakami, 1987).

Remark. Sevostianov and Kachanov (2001), considering normal compliance of

an axisymmetric crack used the SIFs at the outer edge of an annular crack provided by

Smetanin (1968). Later, they used SIF at the inner edge as well (Kachanov and

Sevostianov (2012). For normal compliance that uses K_I it indeed makes no difference.

However, the data on K_{II} and K_{III} provided by Choi and Shield (1981) and Beom and

Earmme (1993) for the outer edge are in much more suitable form than for the inner

one. Since both approaches are approximations and the preference is determined by the

accuracy of the available results on SIFs and convenience of their presentation, we use

here the data for the outer edge.

As far as heat flux intensity factor is concerned, it follows from the work of

Barber (2003) on the connection between the incremental elastic stiffness of a partial

contact between two half-spaces and conductance across it that $\frac{K_T}{q_1} = \frac{K_I}{\sigma_{11}}$ and, therefore,

$F_T(\lambda) = F_1(\lambda)$. At the outer edge, a square root function provides a good

approximation for $F_1(\lambda)$ (Figure 26c):

$$F_1(\lambda) \approx \frac{2\sqrt{\lambda}}{\pi} \tag{57}$$
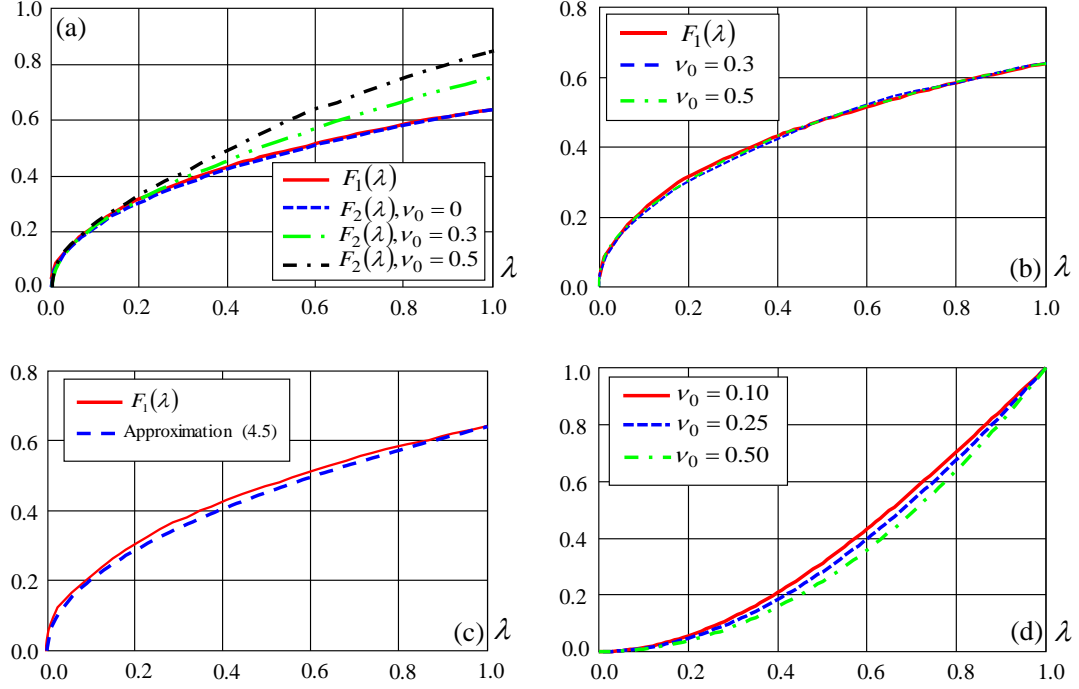
Figure 26. (a) Functions $F_1(\lambda)$ and $F_2(\lambda)$ entering (55) as taken from Choi and Shield (1981) and Beom and Earmme (1993); (b) Accuracy of the approximation (56) for $\nu_0 = 0.3$ and $\nu_0 = 0.5$; (c) Accuracy of the approximation (57); in the case of $\nu_0 = 0$, $F_1(\lambda) = F_2(\lambda)$; (d) Function $\Phi(\lambda, \nu_0)$ entering expression (59)

Using these approximations and treating the crack as having grown from the fixed inner boundary outwards, we obtain components of the compliance contribution of the annular crack (the x_1 axis is normal to the crack) as follows:

$$\frac{V_1}{V}H_{1111} = \frac{1}{V}\int_0^{2\pi}\int_b^a dS_{1111}rdrd\varphi = \frac{1}{V}\frac{1}{4}\int_0^{2\pi}\int_b^a \beta_{11}\left(\frac{\partial K_I}{\partial \sigma_{11}}\right)^2 rdrd\varphi$$

$$= \frac{1}{V}\frac{1}{4}\frac{8(1-\nu_0^2)}{E_0}\int_0^{2\pi}\int_b^a \frac{4r\lambda}{\pi}rdrd\varphi = \frac{1}{V}\frac{16(1-\nu_0^2)}{E_0}\int_b^a r(r-b)dr \qquad (58)$$

$$= \frac{1}{V}\frac{16(1-\nu_0^2)a^3}{3E_0}\frac{(3\lambda^2 - \lambda^2)}{2}$$

Similarly,

91

$$\frac{V_1}{V} H_{1212} = \frac{1}{V} \int_0^{2\pi} \int_b^a dS_{1212} r \, dr \, d\varphi = \frac{1}{V}\frac{1}{4} \int_0^{2\pi} \int_b^a \left[\beta_{22} \left(\frac{\partial K_{II}}{\partial \sigma_{12}} \right)^2 + \beta_{33} \left(\frac{\partial K_{III}}{\partial \sigma_{13}} \right)^2 \right] r \, dr \, d\varphi$$

$$= \frac{1}{V}\frac{32(1-\nu_0^2)}{\pi E_0} \int_0^{2\pi} \int_b^a [sin^2\varphi + cos^2\varphi(1-\nu_0)] \frac{r(r-b)}{(2 - \nu_0\sqrt{1-b/r})^2} \, dr \, d\varphi$$

$$= \frac{1}{V}\frac{32(1-\nu_0^2)(2-\nu_0)}{E_0} \int_b^a \frac{r(r-b)}{(2 - \nu_0\sqrt{1-b/r})^2} \, dr$$

$$= \frac{1}{V}\frac{32(1-\nu_0^2)}{3E_0(2-\nu_0)} a^3 \Phi(\lambda, \nu_0)$$

(59)

Integral in (59) cannot be evaluated in terms of elementary functions, but it converges in the entire interval of variation of the parameters. Function $\Phi(\lambda, \nu_0)$ is illustrated in Figure 25d. The resistivity contribution tensor of the crack is obtained in a similar way: analogously to (53), we have

$$d(k_{ij})^{-1} = \frac{1}{V} R_{ij} = \frac{1}{V}\frac{1}{4} \int_L \left(c \frac{\partial K_T}{\partial q_i} \frac{\partial K_T}{\partial q_j} dl \right) dL$$

(60)

where coefficient c relates the near tip temperature discontinuity to the heat flux intensity factor:

$$[T] = c K_T \sqrt{r/2\pi}$$

(61)

In the case of the isotropic matrix, $c = 4/k_0$ and, analogously to formulas (58) we have

$$\frac{1}{V} R_{11} = \frac{1}{V} \int_0^{2\pi} \int_b^a (dk_{11}) r \, dr \, d\varphi^{-1} = \frac{1}{V}\frac{1}{4} \int_0^{2\pi} \int_b^a c \left(\frac{\partial K_T}{\partial q_1} \right)^2 r \, dr \, d\varphi =$$

$$= \frac{1}{V}\frac{1}{k_0} \int_0^{2\pi} \int_b^a \frac{4r\lambda}{\pi} r \, dr \, d\varphi = \frac{1}{V}\frac{8}{k_0} \int_a^b r(r-b) \, dr$$

$$= \frac{1}{V}\frac{8}{3k_0}(3\lambda^2 - \lambda^3)$$

(62)

4.5 Computation of property contribution tensors for a crack with non-central location of a contact island

The geometry of a crack with an island is defined by two dimensionless parameters: the ratio $\lambda = c/a$ and eccentricity $\beta = d/a$. We calculated non-zero components of the compliance and resistivity contribution tensors - H_{1111}, H_{1212}, H_{1313}, and R_{11} - of individual annular cracks using Finite Element Method (FEM). To produce the 3D mesh, we start by generating the surface mesh of the crack in a custom MATLAB script as follows. First, the profiles (ellipses) of the crack cross-sections are created (Figure 27a) and coordinates of the outline points are stored. Since the crack profiles are stored as ordered lists of point coordinates, they can be easily connected into triangular elements to produce a continuous surface mesh of the crack (Drach et al. (2014); see Figure 27b. The generated surface mesh is then used in the numerical procedure to find components of the crack property contribution tensors as described below.

Crack surface mesh is placed in a large cubic-shaped reference volume with sides five times larger than the crack diameter, in order to reduce boundary effects and simulate remote loading. This setup is auto meshed with linear tetrahedral 3D elements. Note that linear tetrahedral elements are known to be stiffer than nonlinear ones, due to constancy of strain within the elements. We compared predictions of the compliance contribution tensors obtained from models meshed with four and ten nodes tetrahedral elements. The difference was of the order of 1%.
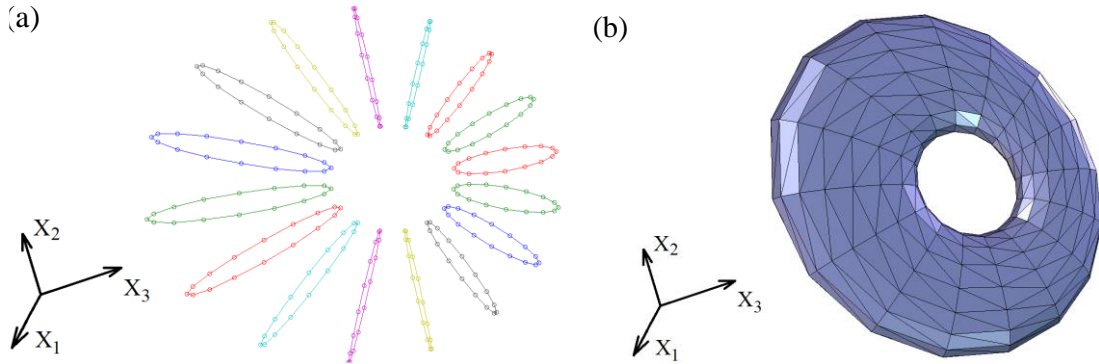
Figure 27. (a) Elliptic profiles of the crack cross-sections; (b) Surface mesh

Due to reasonably accurate predictions by linear elements and considerably higher computational demands of the simulations based on quadratic elements, four points tetrahedral elements were used.

After the volume mesh has been generated, two types of boundary conditions were used to find non-zero components of the property contribution tensors H_{ijkl} and R_{ij}: homogeneous tractions and temperature gradient on the faces of the reference volume, respectively. The non-zero components of the compliance contribution tensor are found from the set of three loading cases: normal loading σ_{11} and two shear loads σ_{12} and σ_{13}. Resistivity contribution tensor has only one non-zero component R_{11} along the crack's axis of symmetry, therefore we consider only the case when temperature gradient is applied along x_1 axis. Once the boundary conditions are prescribed, the FEM simulations are performed, and the result files are processed using a custom Python script to determine H_{ijkl} and R_{ij} tensors. To validate the procedure, we compared the analytic solution for the compliance contribution tensor of a penny

94

shaped crack with the one evaluated numerically (modeled as an oblate spheroid of the aspect ratio 0.01). The maximum error was below 1%.

4.6 Results and verification of the hypotheses

We calculated property contribution tensors for a crack with an island, as a function of two parameters: size of the island as characterized by $\lambda = c/a$ and the position of the island as characterized by $\beta = d/a$ (the configuration is shown in Figure 25). These parameters vary as $0 < \lambda < 1$ and $0 < \beta < \lambda$. Poisson's ratio in the calculation was taken as $\nu_0 = 0.3$. Figure 28 compares numerical results with analytical ones, given by formulas (58), (59), and (62), in the case of centrally located island. Figures Figure 29 and Figure 30 show the dependence of components of H_{ijkl} (normalized to $D = \frac{1}{V}\frac{2\pi^2(1-\nu_0^2)}{E_0}a^3$) and R_{ij} (normalized to $D_1 = \frac{1}{V}\frac{2\pi^2}{k_0}a^3$) on parameters λ and β. Two hypotheses, formulated in Section 4.2, have been validated by these calculations:

A. The effect of a contact as a function of its shift from the center decreases approximately as $\sqrt{1-\beta^2}$ (Figure 31a-c) – reflecting the profile of crack opening displacement in absence of the contact.

95
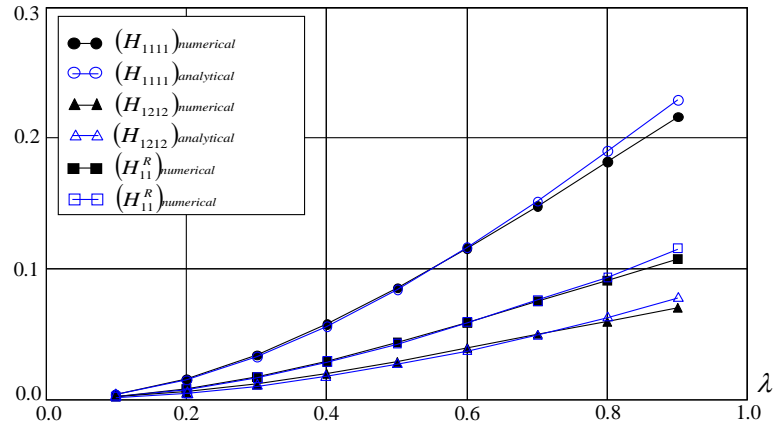
Figure 28. Components of the compliance and resistivity contribution tensors for an annular crack with centrally positioned island. Comparison of analytical results (formulas (58), (59) and (62)) with FEM computations.
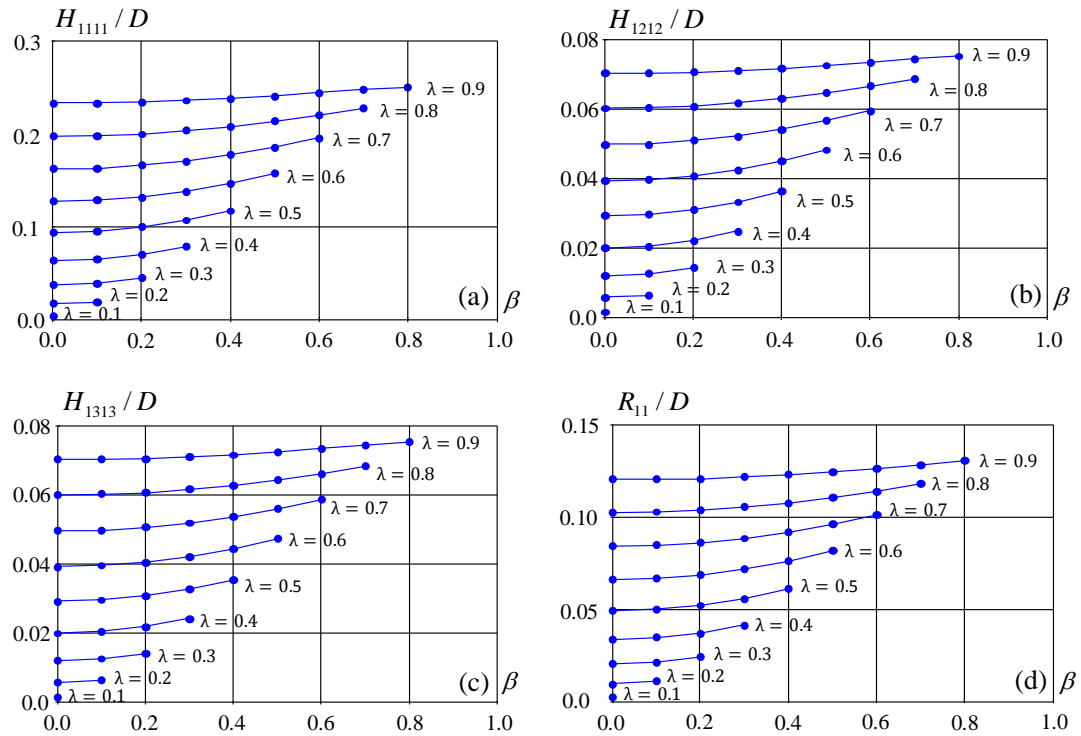
Figure 29. Normalized non-zero components of the compliance and resistivity contribution tensors as functions of the distance between the center of the island of contact and the crack center at different sizes of the island.

B. The ratio of the normal compliance of the crack to the average, over tangential directions, shear compliance, is approximately the same as its value $1 - \nu/2$ for the circular crack (without contact) (Figure 31d). This fact has two important implications:

- The usual parameter of crack density (scalar or tensor) can be retained for cracks with arbitrarily located partial contacts. The value of the crack density parameter needs to be adjusted according to Figure 32 that shows the radius $a_{eff}(\lambda, \beta)$ of a circular crack without contact that has the same compliance as considered crack of radius a with the contact characterized by parameters λ and β;

- Concerning the overall anisotropy of a material with multiple cracks, the said anisotropy has been found earlier to be approximately orthotropic; this fact is rooted in closeness of the two compliances. Our finding, therefore, that the presence of partial contacts does not violate the overall orthotropy.

C. Since effect of a contact is characterized by a function of two parameters

$$(a_{eff}/a)^3 = M(\lambda, \beta) \tag{63}$$

it is difficult to construct its approximate analytical representation. The following observation is useful in this regard: this function is well approximated by the following expression:

$$M(\lambda, \beta) \approx f_1(\lambda) + f_2(\lambda)f_3(\beta) \tag{64}$$

where functions f_1, f_2, and f_3 are given by

$$f_1 = (3\lambda^2 - \lambda^3)/2$$

$$f_2 = 60e^{-6\lambda}f_1(\lambda) \qquad\qquad (65)$$

$$f_3 = 1 - \sqrt{1 - \beta^2}$$

The accuracy of the representation (64) is illustrated in Figure 10.
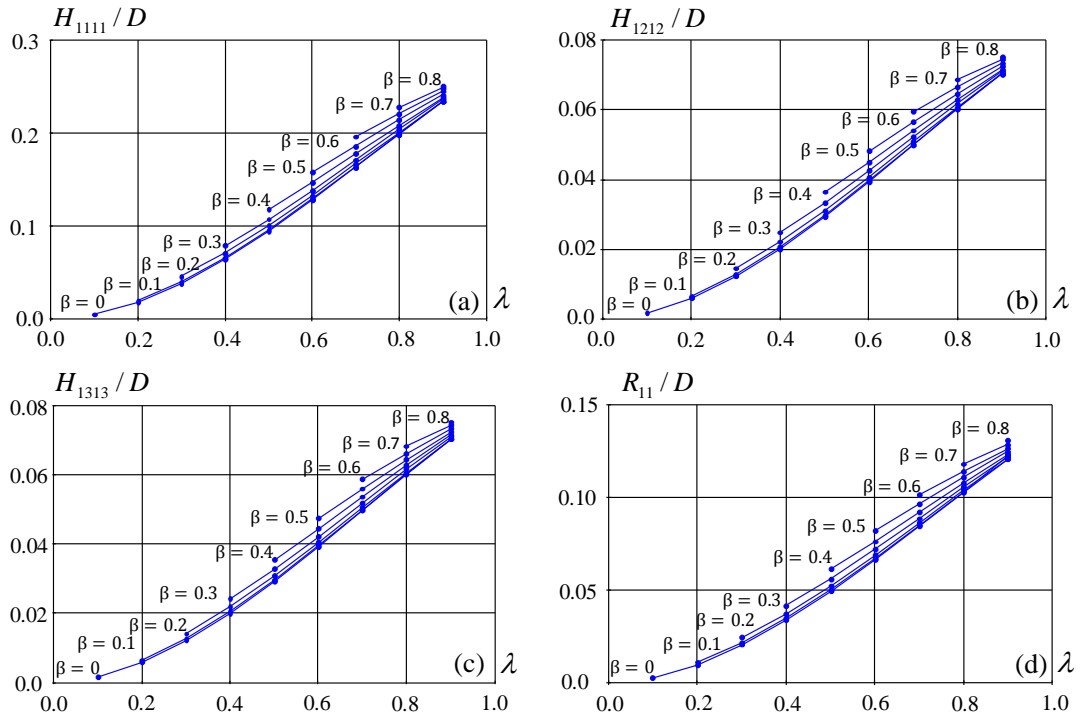
Figure 30. Normalized non-zero components of the compliance and resistivity contribution tensors as functions of the island size at different distances between the center of the island and the crack center
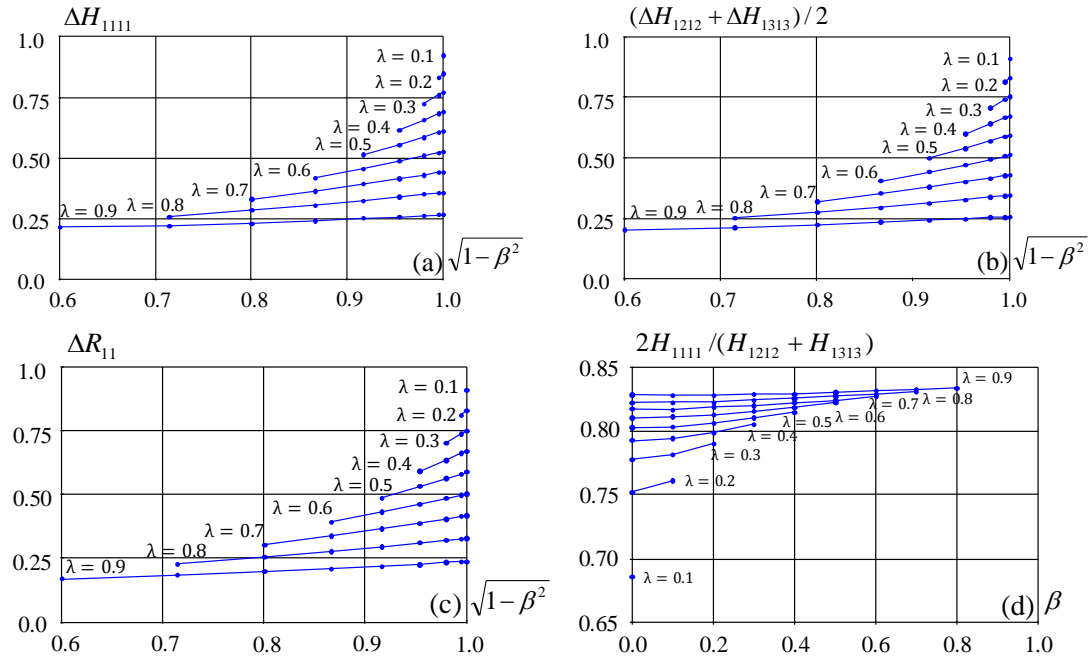
Figure 31. (a)-(c) The change of the compliance contribution tensor of a crack due to the presence of the contact island ($H_{ijkl}^{circular}$ and $R_{ij}^{circular}$ are compliance and resistivity contribution tensor of a circular crack without contact island). Confirmation of the hypothesis A corresponds to the lines being straight. (d) The ratio $2H_{1111}/(H_{1212} + H_{1313})$ (that equals $1 - \nu_0/2$ for a circular crack without contact island). Confirmation of the hypothesis B corresponds to the lines being horizontal and equal to $1 - \nu_0/2$. Poisson's ratio is $\nu_0 = 0.3$
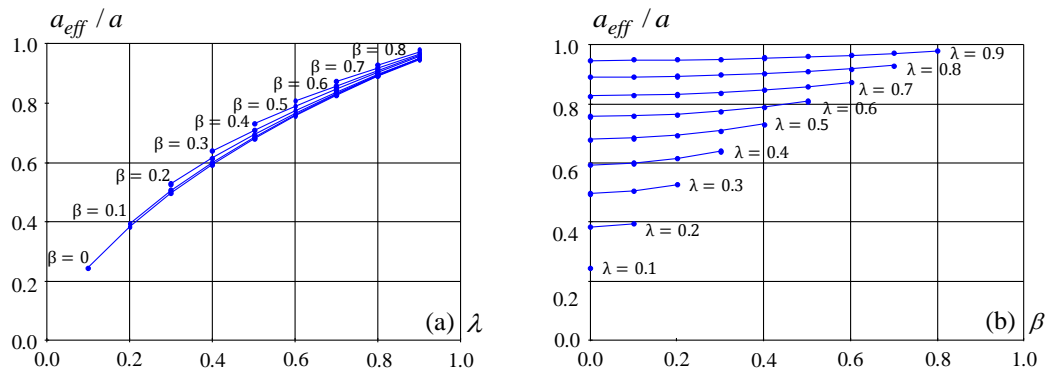
Figure 32. Radius of the "effective" penny shaped crack without island having the same compliance and resistivity contribution tensors as the crack with the island of partial contact as (a) function of the island size, at different distances between the center of the island and the crack center; (b) function of the distance between the center of the island of contact and the crack center at different sizes of the island
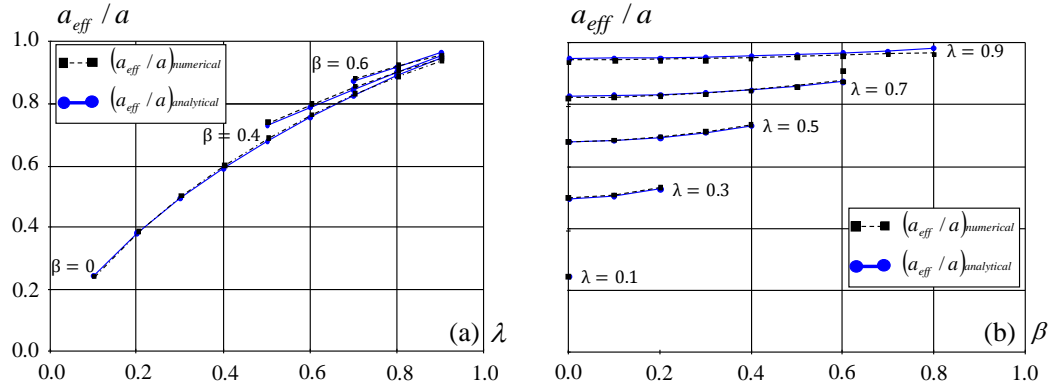
Figure 33. Accuracy of the approximation (64) of the effect of a contact island

4.7   Implications for multiple cracks. Adjusted crack density

As shown above, the normal compliance B_N of a crack with an "island" and its average over tangential directions shear compliance $\langle B_T \rangle$ are about as close as they are for a circular crack. Therefore, a set of multiple cracks with random locations of islands is equivalent – in its effect on the overall elastic properties – to a set of circular cracks, of reduced crack density. In other words, the presence of islands can be accounted for by appropriately reduced crack density.

The obtained results yield explicit expression for this reduction. Indeed, the usual parameter of crack density $\rho = (1/V) \sum a^{(k)3}$ introduced by Bristow (1960) takes the contribution of k-th crack proportionally to its radius cubed. If this crack has an island of partial contact, this contribution is reduced by the "island factor" (63) that reflects the position of the island and its size. Therefore, the adjusted value of the crack density is

$$\rho^* = (1/V) \sum \left(\frac{a^3}{M}\right)^3 \tag{66}$$

With this adjustment, all the available schemes for the effective elastic properties of cracked solids as functions of crack density (the non-interaction approximation, the differential scheme, etc.) can be applied to cracks with islands.

For non-randomly oriented cracks with islands, parameter (63) should be replaced by the tensor one – a similarly adjusted crack density tensor $\boldsymbol{\alpha} = (1/V) \sum (a^3 \mathbf{nn})^k$ (introduced by Kachanov (1980):

$$\boldsymbol{\alpha}^* = (1/V) \sum \left(\frac{a^3}{M} \mathbf{nn}\right)^{(k)} \tag{67}$$

Remark. Strictly speaking, the effective elastic compliances also contain the term dependent on the fourth-rank tensor $\boldsymbol{\alpha} = (1/V) \sum (a^3 \mathbf{nnnn})^k$ that can be similarly adjusted; however, the contribution of this term is usually relatively small; see Kachanov (1992) for discussion in detail.

If the distribution of parameter M is statistically independent of the distributions of crack radii $a^{(k)}$ and crack orientations, the adjusted crack density parameters can be written in the form

$$\rho^* = \left\langle\frac{1}{M}\right\rangle \rho \quad \text{and} \quad \boldsymbol{\alpha}^* = \left\langle\frac{1}{M}\right\rangle \boldsymbol{\alpha} \tag{68}$$

where ρ and $\boldsymbol{\alpha}$ are the usual parameters in absence of islands and angle brackets denote the average, over the crack set, value of the inverse of the "island factor".

4.8 Concluding remarks

A crack of annular geometry, with arbitrarily located "contact island" of the circular shape, has been analyzed, from the point of view of its compliance and resistivity contributions. Such cracks are common in a variety of materials, and their analysis is essential for finding the effective elastic and conductive properties of such materials.

The key points of our analysis can be summarized as follows:

- The stiffening effect of the "island" depends on two parameters: the island size and the distance between its center and the center of the crack. This dependence is investigated numerically, and the results are approximated by a simple analytical expression (64);

- The normal (B_N) compliance of a crack with an "island" and its average over tangential directions shear compliance $\langle B_T \rangle$ are about as close as they are for a circular crack. Hence a set of multiple cracks of this kind is equivalent to a set of circular cracks, of reduced crack density; the latter is explicitly expressed in terms of island parameters. Therefore, all the effective media theories for cracked materials can be used. Note that similar closeness of the two compliances for a variety of highly "irregular" cracks shapes was found by Grechka and Kachanov (2006).

5.0   CLOSING REMARKS

A novel efficient numerical procedure is developed to generate and analyze RVEs with non-ellipsoidal inhomogeneities with volume fraction up to 30%. In the case of porous materials with identical and mixture of voids, Mori-Tanka and Maxwell approximations are in good correspondence with direct FEA simulations for considered volume fractions (0-25%). Approximation methods that allow to separate shape effect and matrix Poisson's ratio are derived, providing an opportunity of extending obtained results to materials with different Poisson's ratio.

The applicability of the replacement relation that interrelates stiffness contribution tensors of inhomogeneities having the same shape but different elastic properties to the considered shapes is examined. Satisfactory approximation is obtained for most considered inhomogeneities of polyhedral shape, except for a tetrahedron, octahedron, cube and smooth tetrahedron for which the maximum relative errors were considerably higher. The error in replacement relation linearly increases with sphericity shape parameter, being zero for the case of spherical inhomogeneity.

Micromechanical homogenization using stiffness contribution tensors of individual polyhedra is performed to calculate overall elastic properties of materials containing multiple randomly oriented particles with volume fraction up to 30%. From comparison with direct FEA it is observed that accuracy of predictions for effective elastic properties using replacement relation depends on matrix and inhomogeneity mechanical properties. In the cases when particles are softer than the matrix, the

replacement relation based on pores produces better estimates for the overall elastic properties. On the other hand, replacement relation based on perfectly rigid particle results in more accurate approximations when particles are stiffer than the matrix.

Crack of annular geometry is considered and property contribution tensors are calculated utilizing Rice's formalism and using FEA. Good correlation between analytical and numerical approaches is obtained for crack with a central island of contact. Finite element calculations are extended to the case of a crack with non-central contact. The effect of the contact as a function of its shift from the center is proportional to $\sqrt{1 - \beta^2}$ – reflecting the profile of crack opening displacement in the absence of the contact. The ratio of the normal compliance of the crack with an island to the shear compliance averaged over the tangential directions is approximately the same as for the circular crack without contact. With the adjusted value of the crack density proposed in this work, all available schemes for the effective elastic properties of cracked solids as functions of crack density can be applied to cracks with islands.

The research in the field of effective properties of composite materials containing various types of defects should continue. The ability to solve complex boundary value problems will benefit the industry by providing new results for property contribution tenors and contribute to the development of a more comprehensive library of solutions. These solutions will be used for optimization of composite materials, which in turn will further stimulate the development of novel structures.

APPENDIX A: COMPLIANCE CONTRIBUTION TENSORS FOR

DIFFERENT PORE SHAPES

The **H**-tensors presented below are normalized by pore volume fraction and matrix Young's modulus as shown in Equation (17). The components for pores of cubical, octahedral and tetrahedral shapes were calculated using the procedure described in Section 2.2.

Sphere. The analytical expression for the H-tensor of a spherical pore obtained using Eshelby solution ((Eshelby, 1957, 1959)) can be found in (Mark Kachanov et al., 2003):

$$\bar{\mathbf{H}} = \frac{3(1-\nu)}{2(7-5\nu)}[10(1+\nu)\mathbf{J} - (1+5\nu)\mathbf{II}] \tag{A. 1}$$

where **J** is the fourth rank unit tensor with components $J_{ijkl} = \frac{(\delta_{ik}\delta_{lj}+\delta_{il}\delta_{kj})}{2}$, and **I** is the second rank unit tensor with components s $I_{ij} = \delta_{ij}$.

Spheroid. The **H**-tensors for oblate and prolate spheroids were presented in Kachanov et al. (2003) and corrected for a misprint in David and Zimmerman (2011).

Cube. Cubical shape can be considered as a special case of a supersphere $x^{2p} + y^{2p} + z^{2p} = 1$ when $p \to \infty$. The results for inhomogenities of this type were presented in Sevostianov et al. (2008) and Chen et al. (2015). However, the **H**-tensor for cubical pore was not provided in the explicit form in the above publications. The components calculated using FEA for matrix Poisson's ratio values $\nu_0 = 0.1, 0.2, 0.3, 0.4$ are given in Figure A.2.
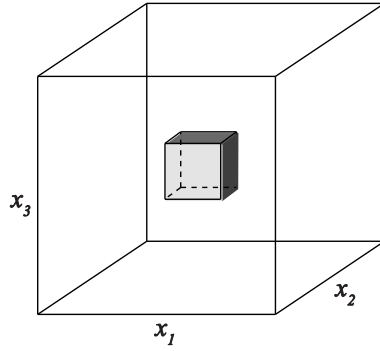
Figure A.1. Orientation of the cube for H-tensor calculations

$$
\text{(a)}\quad
\begin{bmatrix}
2.095 & -0.231 & -0.231 & 0 & 0 & 0 \\
-0.231 & 2.095 & -0.231 & 0 & 0 & 0 \\
-0.231 & -0.231 & 2.095 & 0 & 0 & 0 \\
0 & 0 & 0 & 1.401 & 0 & 0 \\
0 & 0 & 0 & 0 & 1.401 & 0 \\
0 & 0 & 0 & 0 & 0 & 1.401
\end{bmatrix}
\qquad
\text{(b)}\quad
\begin{bmatrix}
2.087 & -0.306 & -0.306 & 0 & 0 & 0 \\
-0.306 & 2.087 & -0.306 & 0 & 0 & 0 \\
-0.306 & -0.306 & 2.087 & 0 & 0 & 0 \\
0 & 0 & 0 & 1.475 & 0 & 0 \\
0 & 0 & 0 & 0 & 1.475 & 0 \\
0 & 0 & 0 & 0 & 0 & 1.475
\end{bmatrix}
$$

$$
\text{(c)}\quad
\begin{bmatrix}
2.035 & -0.372 & -0.372 & 0 & 0 & 0 \\
-0.372 & 2.035 & -0.372 & 0 & 0 & 0 \\
-0.372 & -0.372 & 2.035 & 0 & 0 & 0 \\
0 & 0 & 0 & 1.519 & 0 & 0 \\
0 & 0 & 0 & 0 & 1.519 & 0 \\
0 & 0 & 0 & 0 & 0 & 1.519
\end{bmatrix}
\qquad
\text{(d)}\quad
\begin{bmatrix}
1.988 & -0.424 & -0.424 & 0 & 0 & 0 \\
-0.424 & 1.988 & -0.424 & 0 & 0 & 0 \\
-0.424 & -0.424 & 1.988 & 0 & 0 & 0 \\
0 & 0 & 0 & 1.562 & 0 & 0 \\
0 & 0 & 0 & 0 & 1.562 & 0 \\
0 & 0 & 0 & 0 & 0 & 1.562
\end{bmatrix}
$$

Figure A.2 Normalized H-tensor components of the cubical pore: (a) $v_0 = 0.1$; (b) $v_0 = 0.2$; (c) $v_0 = 0.3$; (d) $v_0 = 0.4$

Octahedron. Octahedral shape can be considered as a special case of a supersphere $(x^{2p} + y^{2p} + z^{2p} = 1)$ when $p = 0.5$.. The results for inhomogenities of this type were presented in Sevostianov et al. (2008) and Chen et al.(2015). However, the H-tensor for octahedral pore was not provided in the explicit form in the above

106

publications. The components calculated using FEA for matrix Poisson's ratio values $v_0 = 0.1, 0.2, 0.3, 0.4$ are given in

Figure A.3. Orientation of the octahedron for H-tensor calculations

$$
\begin{bmatrix}
2.139 & -0.225 & -0.400 & 0 & 0 & 0 \\
-0.225 & 2.139 & -0.400 & 0 & 0 & 0 \\
-0.400 & -0.400 & 2.314 & 0 & 0 & 0 \\
0 & 0 & 0 & 1.358 & 0 & 0 \\
0 & 0 & 0 & 0 & 1.183 & 0 \\
0 & 0 & 0 & 0 & 0 & 1.183
\end{bmatrix}
\qquad
\begin{bmatrix}
2.162 & -0.310 & -0.489 & 0 & 0 & 0 \\
-0.310 & 2.162 & -0.489 & 0 & 0 & 0 \\
-0.489 & -0.489 & 2.341 & 0 & 0 & 0 \\
0 & 0 & 0 & 1.417 & 0 & 0 \\
0 & 0 & 0 & 0 & 1.237 & 0 \\
0 & 0 & 0 & 0 & 0 & 1.237
\end{bmatrix}
$$

(a) (b)

$$
\begin{bmatrix}
2.149 & -0.389 & -0.563 & 0 & 0 & 0 \\
-0.389 & 2.149 & -0.563 & 0 & 0 & 0 \\
-0.563 & -0.563 & 2.326 & 0 & 0 & 0 \\
0 & 0 & 0 & 1.444 & 0 & 0 \\
0 & 0 & 0 & 0 & 1.271 & 0 \\
0 & 0 & 0 & 0 & 0 & 1.271
\end{bmatrix}
\qquad
\begin{bmatrix}
2.127 & -0.447 & -0.630 & 0 & 0 & 0 \\
-0.447 & 2.127 & -0.630 & 0 & 0 & 0 \\
-0.630 & -0.630 & 2.311 & 0 & 0 & 0 \\
0 & 0 & 0 & 1.473 & 0 & 0 \\
0 & 0 & 0 & 0 & 1.289 & 0 \\
0 & 0 & 0 & 0 & 0 & 1.289
\end{bmatrix}
$$

(c) (d)

Figure A. 4. Normalized H-tensor components of the octahedral pore: (a) $v_0 = 0.1$; (b) $v_0 = 0.2$; (c) $v_0 = 0.3$; (d) $v_0 = 0.4$

Tetrahedron. To the authors' knowledge, the **H**-tensor for a pore of tetrahedral shape has never been published. The components calculated using FEA for matrix Poisson's ratio values $v_0 = 0.1, 0.2, 0.3, 0.4$ are presented in Figure A.6.
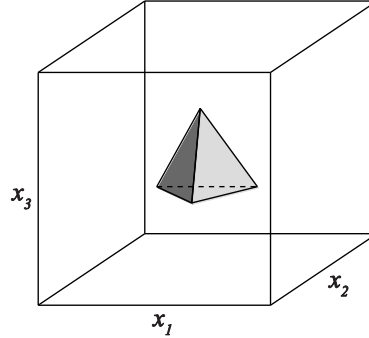

Figure A.5.Orientation of the tetrahedron for H-tensor calculations

$$
\begin{bmatrix}
2.597 & -0.347 & -0.295 & 0 & -0.073 & 0 \\
-0.347 & 2.596 & -0.295 & 0 & 0.072 & 0 \\
-0.295 & -0.295 & 2.545 & 0 & 0 & 0 \\
0 & 0 & 0 & 1.473 & 0 & -0.074 \\
-0.073 & 0.072 & 0 & 0 & 1.525 & 0 \\
0 & 0 & 0 & -0.074 & 0 & 1.526
\end{bmatrix}
$$

(a)

$$
\begin{bmatrix}
2.600 & -0.441 & -0.368 & 0 & -0.103 & 0 \\
-0.441 & 2.599 & -0.368 & 0 & 0.102 & 0 \\
-0.368 & -0.368 & 2.527 & 0 & 0 & 0 \\
0 & 0 & 0 & 1.522 & 0 & -0.104 \\
-0.103 & 0.102 & 0 & 0 & 1.594 & 0 \\
0 & 0 & 0 & -0.104 & 0 & 1.595
\end{bmatrix}
$$

(b)

$$
\begin{bmatrix}
2.570 & -0.525 & -0.430 & 0 & 0.130 & 0 \\
-0.525 & 2.569 & -0.430 & 0 & -0.137 & 0 \\
-0.430 & -0.430 & 2.474 & 0 & -0.002 & 0.001 \\
0 & 0 & 0 & 1.547 & 0 & 0.076 \\
0.130 & -0.137 & -0.002 & 0 & 1.642 & -0.001 \\
0 & 0 & 0.001 & 0.076 & -0.001 & 1.642
\end{bmatrix}
$$

(c)

$$
\begin{bmatrix}
2.502 & -0.596 & -0.479 & 0 & -0.163 & 0 \\
-0.596 & 2.501 & -0.480 & 0 & 0.162 & 0 \\
-0.479 & -0.480 & 2.387 & 0 & 0 & 0 \\
0 & 0 & 0 & 1.550 & 0 & -0.164 \\
-0.163 & 0.162 & 0 & 0 & 1.666 & 0 \\
0 & 0 & 0 & -0.164 & 0 & 1.667
\end{bmatrix}
$$

(d)

Figure A.6. Normalized H-tensor components of the tetrahedral pore: (a) $v_0 = 0.1$; (b) $v_0 = 0.2$; (c) $v_0 = 0.3$; (d) $v_0 = 0.4$

APPENDIX B: COMPARISON OF STIFFNESS CONTRIBUTION TENSORS

FOR DIFFERENT PARTILCE SHAPES

Table B.1 Comparison between stiffness contribution tensors calculated via direct FEA and obtained utilizing the replacement relation. Matrix material: $E_0 = 1GPa$ and $\nu_0 = 0.2$, particle material: $E_1 = 20GPa$, $\nu_1 = 0.2$

Shape	$\overline{N}_{1111}^{FEA}$	$\overline{N}_{1122}^{FEA}$	$\overline{N}_{1212}^{FEA}$	$\overline{N}_{1111}^{repl.}$	$\overline{N}_{1122}^{repl.}$	$\overline{N}_{1212}^{repl.}$	$\Delta\overline{N}_{1111}$ (%)	$\Delta\overline{N}_{1122}$ (%)	$\Delta\overline{N}_{1212}$ (%)	$\left\lVert \mathbf{N}^{FEA} - \mathbf{N}^{repl.} \right\rVert$
Sphere	2.011	0.502	0.754	2.011	0.502	0.754	0.00	0.00	0.00	0.000
Polyhedral Supersphere 1 (smooth)	2.012	0.505	0.758	2.010	0.505	0.757	0.10	0.01	0.11	0.002
Polyhedral Supersphere	2.054	0.506	0.777	2.031	0.506	0.767	1.15	0.13	1.32	0.024
Polyhedral Supersphere 2 (smooth)	2.029	0.505	0.766	2.017	0.505	0.762	0.56	0.06	0.64	0.012
Polyhedral Supersphere	2.068	0.506	0.785	2.036	0.507	0.771	1.54	0.19	1.86	0.033
Cube (smooth)	2.078	0.488	0.754	2.064	0.487	0.745	0.69	0.30	1.23	0.0174
Cube	2.336	0.477	0.824	2.201	0.477	0.765	5.78	0.10	7.17	0.136
Icosahedron	2.060	0.504	0.777	2.035	0.504	0.765	1.20	0.07	1.60	0.025
Truncated Octahedron	2.061	0.517	0.799	2.030	0.515	0.780	1.52	0.43	2.45	0.036
Cuboctahedron	2.129	0.491	0.779	2.081	0.492	0.760	2.24	0.34	2.54	0.049
Rhombic Dodecahedron	2.068	0.520	0.808	2.032	0.517	0.783	1.78	0.62	3.11	0.043
Octahedron (smooth)	2.059	0.532	0.8261	2.024	0.523	0.790	1.74	1.80	4.36	0.041
Octahedron	2.145	0.545	0.875	2.069	0.526	0.804	3.54	3.58	8.11	0.115

Shape	Tetrahedron (smooth)	Tetrahedron
$\overline{N}_{1111}^{FEA}$	2.1877	2.6230
$\overline{N}_{1122}^{FEA}$	2.1595	2.5115
$\overline{N}_{1212}^{FEA}$	0.4985	0.5155
$\overline{N}_{3333}^{FEA}$	0.5266	0.6269
$\overline{N}_{1133}^{FEA}$	0.8146	0.9411

Table B.1. Continued

Shape	Tetrahedron (smooth)	Tetrahedron
$\bar{N}_{1313}^{FEA}$	0.8427	1.0522
$\bar{N}_{1111}^{repl.}$	2.1058	2.2801
$\bar{N}_{1122}^{repl.}$	0.4731	0.4393
$\bar{N}_{1212}^{repl.}$	0.7497	0.7558
$\bar{N}_{3333}^{repl.}$	2.0407	2.1163
$\bar{N}_{1133}^{repl.}$	0.5381	0.6031
$\bar{N}_{1313}^{repl.}$	0.8145	0.9192
$\max\left(\Delta\bar{N}_{ijkl}(\%)\right)$	7.96	19.69
$\|\mathbf{N}^{FEA} - \mathbf{N}^{repl.}\|$	0.130	0.443

Table B.2. Comparison between stiffness contribution tensors calculated FEA directly and obtained utilizing replacement relation formula. Matrix material: $E_0 = 1GPa$ and $\nu_0 = 0.4$, particle material: $E_1 = 20GPa$, $\nu_1 = 0.2$

Shape	$\bar{N}_{1111}^{FEA}$	$\bar{N}_{1122}^{FEA}$	$\bar{N}_{1212}^{FEA}$	$\bar{N}_{1111}^{repl.}$	$\bar{N}_{1122}^{repl.}$	$\bar{N}_{1212}^{repl.}$	$\Delta\bar{N}_{1111}$ (%)	$\Delta\bar{N}_{1122}$ (%)	$\Delta\bar{N}_{1212}$ (%)	$\|\mathbf{N}^{FEA} - \mathbf{N}^{repl.}\|$
Sphere	2.721	1.259	0.730	2.721	1.259	0.730	0.00	0.00	0.00	0.000
Polyhedral Supersphere 1 (smooth)	2.719	1.262	0.736	2.717	1.262	0.733	0.07	0.02	0.12	0.002
Polyhedral Supersphere	2.761	1.259	0.755	2.738	1.262	0.744	0.82	0.23	1.44	0.026
Polyhedral Supersphere 2 (smooth)	2.735	1.262	0.744	2.724	1.263	0.739	0.39	0.10	0.69	0.012
Polyhedral Supersphere	2.773	1.260	0.765	2.742	1.263	0.749	1.10	0.30	2.07	0.034
Cube (smooth)	2.800	1.235	0.722	2.787	1.232	0.717	0.45	0.02	1.27	0.013
Cube	3.078	1.191	0.777	2.945	1.206	0.720	4.32	1.27	7.32	0.148
Icosahedron	2.768	1.256	0.754	2.744	1.259	0.741	0.85	0.23	1.75	0.027
Truncated Octahedron	2.755	1.274	0.783	2.727	1.275	0.762	1.04	0.03	2.69	0.029
Cuboctahedron	2.851	1.233	0.749	2.804	1.239	0.729	1.64	0.53	2.67	0.053

Table B.2. Continued

Shape	$\bar{N}^{FEA}_{1111}$	$\bar{N}^{FEA}_{1122}$	$\bar{N}^{FEA}_{1212}$	$\bar{N}^{repl.}_{1111}$	$\bar{N}^{repl.}_{1122}$	$\bar{N}^{repl.}_{1212}$	$\Delta\bar{N}_{1111}$ (%)	$\Delta\bar{N}_{1122}$ (%)	$\Delta\bar{N}_{1212}$ (%)	$\left\Vert \mathbf{N}^{FEA} - \mathbf{N}^{repl.} \right\Vert$
Rhombic Dodecahedron	2.760	1.277	0.792	2.728	1.277	0.765	1.17	0.01	3.46	0.033
Octahedron (smooth)	2.735	1.295	0.815	2.708	1.288	0.777	1.00	0.51	4.68	0.041
Octahedron	2.802	1.306	0.874	2.743	1.292	0.794	2.09	1.00	8.90	0.085

Shape	Tetrahedron (smooth)	Tetrahedron
$\bar{N}^{FEA}_{1111}$	2.8833	3.2665
$\bar{N}^{FEA}_{1122}$	1.2419	1.2262
$\bar{N}^{FEA}_{1212}$	0.7848	0.9041
$\bar{N}^{FEA}_{3333}$	2.8501	3.1522
$\bar{N}^{FEA}_{1133}$	1.2752	1.3405
$\bar{N}^{FEA}_{1313}$	0.8179	1.0179
$\bar{N}^{repl.}_{1111}$	2.8106	2.9684
$\bar{N}^{repl.}_{1122}$	1.2205	1.1747
$\bar{N}^{repl.}_{1212}$	0.7173	0.7123
$\bar{N}^{repl.}_{3333}$	2.7351	2.7849
$\bar{N}^{repl.}_{1133}$	1.2961	1.3582
$\bar{N}^{repl.}_{1313}$	0.7924	0.8950
$\max\left(\Delta\bar{N}_{ijkl}(\%)\right)$	8.60	21.22
$\Vert \mathbf{N}^{FEA} - \mathbf{N}^{repl.} \Vert$	0.136	0.385

LITERATURE CITED

Altendorf, H., & Jeulin, D. (2011). Random-walk-based stochastic modeling of three-dimensional fiber systems. *Physical Review E*, *83*(4), 041804. http://doi.org/10.1103/PhysRevE.83.041804

Argatov, I., & Sevostianov, I. (2011). Rigid toroidal inhomogeneity in an elastic medium. *International Journal of Engineering Science*, *49*(1), 61–74. http://doi.org/10.1016/j.ijengsci.2010.06.023

Asadi, E., Fariborz, S., & Ayatollahi, M. (2009). Analysis of multiple axisymmetric annular cracks. *Journal of Mechanics of Materials and Structures*, *4*.

Barber, J. R. (2003). Bounds on the electrical resistance between contacting elastic rough bodies. *Proceedings of the Royal Society of London A: Mathematical, Physical and Engineering Sciences*, *459*(2029), 53–66. http://doi.org/10.1098/rspa.2002.1038

Benveniste, Y. (1987a). A new approach to the application of Mori-Tanaka's theory in composite materials. *Mechanics of Materials*, *6*(2), 147–157. http://doi.org/10.1016/0167-6636(87)90005-6

Benveniste, Y. (1987b). A new approach to thea pplication of Mori-Tanaka's theory in composite materials. *Mechanics of Materials*, *6*(2), 147–157. http://doi.org/10.1016/0167-6636(87)90005-6

Benzley, S. E., Perry, E., Merkley, K., Clark, B., & Sjaardama, G. (1995). A Comparison of All-Hexahedral and All-Tetrahedral Finite Element Meshes for Elastic and Elasto-Plastic Analysis. In *Proceedings of 4th International Meshing Roundtable* (pp. 179–191). Sandia National Laboratories.

Beom, H. G., & Earmme, Y. Y. (1993). Analysis of a Flat Annular Crack under Shear Loading. *KSME Journal*, *7*(I), 35–47.

Bertei, A., Chueh, C.-C., Pharoah, J. G., & Nicolella, C. (2014). Modified collective rearrangement sphere-assembly algorithm for random packings of nonspherical particles: Towards engineering applications. *Powder Technology*, *253*, 311–324. http://doi.org/10.1016/j.powtec.2013.11.034

Bhowmick, S., Meĺndez-Martínez, J. J., & Lawn, B. R. (2007). Bulk silicon is susceptible to fatigue. *Applied Physics Letters*, *91*(20), 1–4. http://doi.org/10.1063/1.2801390

Böhm, H. J., Han, W., & Eckschlager, A. (2004). Multi-inclusion unit cell studies of reinforcement stresses and particle failure in discontinuously reinforced ductile matrix composites. *CMES: Computer Modeling in Engineering Science*, *5*, 5–20.

Böhm, H. J., & Rasool, A. (2016). Effects of particle shape on the thermoelastoplastic behavior of particle reinforced composites. *International Journal of Solids and Structures*, *87*, 90–101. http://doi.org/10.1016/j.ijsolstr.2016.02.028

Bristow J. R. (1960). Microcracks , and the static and dynamic ellastic constants of annealed and heady cold-worked metals. *British Journal of Applied Physics*, *11*(81), 81–85.

Buck, O., Skillings, B. J., & Reed, L. K. (1983). Simulation of Closure: Effects on Crack Detection Probability and Stress Distributions. *Review of Progress in Quantitative Nondestructive Evaluation*, *2A*, 345–352.

Byholm, T., Toivakka, M., & Westerholm, J. (2009). Effective packing of 3-dimensional voxel-based arbitrarily shaped particles. *Powder Technology*, *196*(2), 139–146. http://doi.org/10.1016/j.powtec.2009.07.013

Cai, Z. B., Gao, S. S., Zhu, M. H., Liu, J., Shen, H. M., Yu, H. Y., & Zhou, Z. R. (2011). Investigation of micro-cracking behaviors of human femur cortical bone during radial fretting. *Tribology International*, *44*(11), 1556–1564. http://doi.org/10.1016/j.triboint.2010.10.012

Cao, Y., Fan, J., Bai, L., Hu, P., Yang, G., Yuan, F., & Chen, Y. (2010). Formation of cubic Cu mesocrystals by a solvothermal reaction. *CrystEngComm*, *12*(11), 3894. http://doi.org/10.1039/c003554h

Chen, F. C., & Young, K. (1977). Inclusions of arbitrary shape in an elastic medium. *Journal of Mathematical Physics*, *18*(7), 1412. http://doi.org/10.1063/1.523438

Chen, F., Sevostianov, I., Giraud, A., & Grgic, D. (2015). Evaluation of the effective elastic and conductive properties of a material containing concave pores. *International Journal of Engineering Science*, *97*, 60–68. http://doi.org/10.1016/j.ijengsci.2015.08.012

Chen, F., Sevostianov, I., Giraud, A., & Grgic, D. (2017). Accuracy of the replacement relations for materials with non-ellipsoidal inhomogeneities. *International Journal of Solids and Structures*, *104-105*, 73–80. http://doi.org/10.1016/j.ijsolstr.2016.10.023

Choi, I., & Shield, R. T. (1981). A note on a flat toroidal crack in an elastic isotropic body. *International Journal of Solids and Structures*, *18*(6), 479–486.

Choren, J. A., Heinrich, S. M., & Silver-Thorn, M. B. (2013). Young's modulus and volume porosity relationships for additive manufacturing applications. *Journal of Materials Science*, *48*(15), 5103–5112. http://doi.org/10.1007/s10853-013-7237-5

Cifuentes, A. O., & Kalbag, A. (1992). A performance study of tetrahedral and hexahedral elements in 3D finite element analysis. *Finite Elements in Analysis and Design*, *12*, 313–318. http://doi.org/10.1016/0168-874X(92)90040-J

Clarke, R. R. (1921). Annular cracks: a discussion of the various theories accounting for their formation. *The Metal Industry*, *19*, 243–244.

Clements, D. L., & Ang, W. T. (1988). Stress intensity factors for the circular annulus crack. *International Journal of Engineering Science*, *26*(4), 325–329.

Cravillon, J., Schröder, C. a., Bux, H., Rothkirch, A., Caro, J., & Wiebcke, M. (2012). Formate modulated solvothermal synthesis of ZIF-8 investigated using time-resolved in situ X-ray diffraction and scanning electron microscopy. *CrystEngComm*, *14*(2), 492. http://doi.org/10.1039/c1ce06002c

David, E. C., & Zimmerman, R. W. (2011). Compressibility and shear compliance of spheroidal pores: Exact derivation via the Eshelby tensor, and asymptotic expressions in limiting cases. *International Journal of Solids and Structures*, *48*(5), 680–686. http://doi.org/10.1016/j.ijsolstr.2010.11.001

Donev, A., Cisse, I., Sachs, D., Variano, E. A., Stillinger, F. H., Connelly, R., … Chaikin, P. M. (2004). Improving the density of jammed disordered packings using ellipsoids. *Science (New York, N.Y.)*, *303*(5660), 990–3. http://doi.org/10.1126/science.1093010

Drach, A., Drach, B., & Tsukrov, I. (2014). Processing of fiber architecture data for finite element modeling of 3D woven composites. *Advances in Engineering Software*, *72*, 18–27. http://doi.org/10.1016/j.advengsoft.2013.06.006

Drach, B., Drach, A., & Tsukrov, I. (2014). Prediction of the effective elastic moduli of materials with irregularly-shaped pores based on the pore projected areas. *International Journal of Solids and Structures*, *51*(14), 2687–2695. http://doi.org/10.1016/j.ijsolstr.2014.03.042

Drach, B., Drach, A., Tsukrov, I., Penverne, M., & Lapusta, Y. (2014). Finite Element Models of 3D Woven Composites Based on Numerically Generated Micro-Geometry of Reinforcement. In *Proceedings of the American Society for Composites 2014 - 29th Technical Conference on Composite Materials*. San Diego, CA.

Drach, B., Tsukrov, I., Gross, T. S., Dietrich, S., Weidenmann, K., Piat, R., & Böhlke, T. (2011). Numerical modeling of carbon/carbon composites with nanotextured matrix and 3D pores of irregular shapes. *International Journal of Solids and Structures*, *48*(18), 2447–2457. http://doi.org/10.1016/j.ijsolstr.2011.04.021

Drach, B., Tsukrov, I., & Trofimov, A. (2016). Comparison of full field and single pore approaches to homogenization of linearly elastic materials with pores of regular and irregular shapes. *International Journal of Solids and Structures*, *0*, 1–16. http://doi.org/10.1016/j.ijsolstr.2016.06.023

Ekneligoda, T. C., & Zimmerman, R. W. (2006). Compressibility of two-dimensional pores having n-fold axes of symmetry. *Proceedings of the Royal Society A: Mathematical, Physical and Engineering Sciences*, *462*(2071), 1933–1947. http://doi.org/10.1098/rspa.2006.1666

Ekneligoda, T. C., & Zimmerman, R. W. (2008). Shear compliance of two-dimensional pores possessing N-fold axis of rotational symmetry. *Proceedings of the Royal Society A: Mathematical, Physical and Engineering Sciences*, *464*(2091), 759–775. http://doi.org/10.1098/rspa.2007.0268

El Moumen, A., Kanit, T., Imad, A., & El Minor, H. (2015). Effect of reinforcement shape on physical properties and representative volume element of particles-reinforced composites: Statistical and numerical approaches. *Mechanics of Materials*, *83*, 1–16. http://doi.org/10.1016/j.mechmat.2014.12.008

Eroshkin, O., & Tsukrov, I. (2005). On micromechanical modeling of particulate composites with inclusions of various shapes. *International Journal of Solids and Structures*, *42*(2), 409–427. http://doi.org/10.1016/j.ijsolstr.2004.06.045

Eshelby, J. D. (1957). The Determination of the Elastic Field of an Ellipsoidal Inclusion, and Related Problems. *Proceedings of the Royal Society A: Mathematical, Physical and Engineering Sciences*, *241*(1226), 376–396. http://doi.org/10.1098/rspa.1957.0133

Eshelby, J. D. (1959). The Elastic Field Outside an Ellipsoidal Inclusion. *Proceedings of the Royal Society of London Series A Mathematical and Physical Sciences*, *252*(1271), 561–569. http://doi.org/10.1098/rspa.1959.0173

Eshelby, J. D. (1961). Elastic inclusions and inhomogeneities. *Progress in Solid Mechanics*, *2*, 89–140.

Faivre, G. (1969). Déformations de cohérence d'un précipité quadratique. *Physica Status Solidi (b)*, *35*(1), 249–259. http://doi.org/10.1002/pssb.19690350124

Fan, X., Gitzhofer, F., & Boulos, M. (1998). Investigation of Alumina Splats Formed in the Induction Plasma Process. *Journal of Thermal Spray Technology*, *7*(2), 197–204. http://doi.org/10.1361/105996398770350936

Garboczi, E. J., & Douglas, J. F. (2012). Elastic moduli of composites containing a low concentration of complex-shaped particles having a general property contrast with the matrix. *Mechanics of Materials*, *51*, 53–65. http://doi.org/10.1016/j.mechmat.2012.03.009

Ghossein, E., & Lévesque, M. (2012). A fully automated numerical tool for a comprehensive validation of homogenization models and its application to spherical particles reinforced composites. *International Journal of Solids and Structures*, *49*(11-12), 1387–1398. http://doi.org/10.1016/j.ijsolstr.2012.02.021

Ghossein, E., & Lévesque, M. (2014). A comprehensive validation of analytical homogenization models: The case of ellipsoidal particles reinforced composites. *Mechanics of Materials*, *75*, 135–150. http://doi.org/10.1016/j.mechmat.2014.03.014

Glubokovskikh, S., Gurevich, B., Lebedev, M., Mikhaltsevitch, V., & Tan, S. (2016). Effect of asperities on stress dependency of elastic properties of cracked rocks. *International Journal of Engineering Science*, *98*, 116–125. http://doi.org/10.1016/j.ijengsci.2015.09.001

González, C., Segurado, J., & LLorca, J. (2004). Numerical simulation of elasto-plastic deformation of composites: evolution of stress microfields and implications for homogenization models. *Journal of the Mechanics and Physics of Solids*, *52*(7), 1573–1593. http://doi.org/10.1016/j.jmps.2004.01.002

Grechka, V., & Kachanov, M. (2006). Effective elasticity of rocks with closely spaced and intersecting cracks. *Geophysics*, *71*(3), D85. http://doi.org/10.1190/1.2197489

Grinchenko, V. T., & Ulitko, A. F. (1965). Tension of an elastic space weekend by a ring-shaped crack. *Applied Mechanics*, *1*, 61–64.

Gusev, A. A. (1997). Representative volume element size for elastic composites: A numerical study. *Journal of the Mechanics and Physics of Solids*, *45*(9), 1449–1459. http://doi.org/10.1016/S0022-5096(97)00016-1

Gusev, A. A. (2016a). Controlled accuracy finite element estimates for the effective stiffness of composites with spherical inclusions. *International Journal of Solids and Structures*, *80*, 227–236. http://doi.org/10.1016/j.ijsolstr.2015.11.006

Gusev, A. A. (2016b). Time domain finite element estimates of dynamic stiffness of viscoelastic composites with stiff spherical inclusions. *International Journal of Solids and Structures*, *88-89*, 79–87. http://doi.org/10.1016/j.ijsolstr.2016.03.021

Hashemi, R., Avazmohammadi, R., Shodja, H. M., & Weng, G. J. (2009). Composites with superspherical inhomogeneities. *Philosophical Magazine Letters*, *89*(7), 439–451. http://doi.org/10.1080/09500830903019020

Hashin, Z., & Shtrikman, S. (1963). A variational approach to the theory of the elastic behaviour of multiphase materials. *Journal of the Mechanics and Physics of Solids*, *11*(2), 127–140. http://doi.org/10.1016/0022-5096(63)90060-7

Hazanov, S., & Huet, C. (1994). Order relationships for boundary conditions effect in heterogeneous bodies smaller than the representative volume. *Journal of the Mechanics and Physics of Solids*, *42*(12), 1995–2011. http://doi.org/10.1016/0022-5096(94)90022-1

Hill, R. (1952). The Elastic Behaviour of a Crystalline Aggregate. *Proceedings of the Physical Society. Section A*, *65*(5), 349–354. http://doi.org/10.1088/0370-1298/65/5/307

Hill, R. (1963). Elastic Properties of Reinforced Solids: Some Theoritical Principles. *Journal of the Mechanics and Physics of Solids*. http://doi.org/10.1016/0022-5096(63)90036-X

Hill, R. (1965). A self-consistent mechanics of composite materials. *Journal of the Mechanics and Physics of Solids*, *13*(4), 213–222. http://doi.org/10.1016/0022-5096(65)90010-4

Horii, H., & Nemat-Nasser, S. (1983). Overall moduli of solids with microcracks: Load-induced anisotropy. *Journal of the Mechanics and Physics of Solids*, *31*(2), 155–171. http://doi.org/10.1016/0022-5096(83)90048-0

Huet, C. (1990). Application of variational concepts to size effects in elastic heterogeneous bodies. *Journal of the Mechanics and Physics of Solids*, *38*(6), 813–841. http://doi.org/10.1016/0022-5096(90)90041-2

Jasiuk, I. (1995). Cavities vis-a-vis rigid inclusions: Elastic moduli of materials with polygonal inclusions. *International Journal of Solids and Structures*, *32*(3-4), 407–422. http://doi.org/10.1016/0020-7683(94)00119-H

Jasiuk, I., Chen, J., & Thorpe, M. (1994). Elastic moduli of two dimensional materials with polygonal and elliptical holes. *Applied Mechanics Reviews*, *47*(1), 18–28.

Kachanov, M. L. (1980). Continuum model of medium with cracks. *Journal of the Engineering Mechanics Division*. Retrieved from http://cedb.asce.org/cgi/WWWdisplay.cgi?5015750

Kachanov, M. L. (1992). Effective Elastic Properties of Cracked Solids: Critical Review of Some Basic Concepts. *Applied Mechanics Reviews*. http://doi.org/10.1115/1.3119761

Kachanov, M., & Sevostianov, I. (2005). On quantitative characterization of microstructures and effective properties. *International Journal of Solids and Structures*, *42*(2), 309–336. http://doi.org/10.1016/j.ijsolstr.2004.06.016

Kachanov, M., & Sevostianov, I. (2012). Rice ' s Internal Variables Formalism and Its Implications for the Elastic and Conductive Properties of Cracked Materials , and for the Attempts to Relate Strength to Stiffness. In *Journal of Applied Mechanics* (Vol. 79, pp. 1–10). http://doi.org/10.1115/1.4005957

Kachanov, M., Shafiro, B., & Tsukrov, I. (2003). *Handbook of Elasticity Solutions*. Kluwer Academic Publishers.

Kachanov, M., Tsukrov, I., & Shafiro, B. (1994). Effective Moduli of Solids With Cavities of Various Shapes. *Applied Mechanics Reviews*, *47*(1S), S151. http://doi.org/10.1115/1.3122810

Kachanov, M., Tsukrov, I., & Shafiro, B. (1994). Effective moduli of solids with cavities of various shapes. *Applied Mechanics Reviews*, *47*(1S), S151. http://doi.org/10.1115/1.3122810

Kanit, T., Forest, S., Galliet, I., Mounoury, V., & Jeulin, D. (2003). Determination of the size of the representative volume element for random composites: statistical and numerical approach. *International Journal of Solids and Structures*, *40*(13-14), 3647–3679. http://doi.org/10.1016/S0020-7683(03)00143-4

Khachiyan, L. G. (1996). Rounding of Polytopes in the Real Number Model of Computation. *Mathematics of Operations Research*, *21*(2), 307–320. http://doi.org/10.1287/moor.21.2.307

Korsunsky, a M., & Hills, D. a. (2005). Solution of axisymmetric crack problems using distributed dislocation ring dipoles. *The Journal of Strain Analysis for Engineering Design*, *35*(August 1999), 373–382. http://doi.org/10.1243/0309324001514143

Kröner, E. (1958). Berechnung der Elastischen Konstant des Vielkristalls aus den Konstant des Einkristalls. *Zeitschrift Für Physik*, *151*, 504–518.

Kudinov, V. V. (1977). Plasma sprayed coatings. *Moscow: Nauka.(In Russian.)*.

Kunin, I. A., & Sosnina, E. G. (1971). Ellipsoidal inhomogeneity in the elastic medium. *Sov Phys Dokl*, *16*, 571–574.

Kushch, V. I., & Sevostianov, I. (2015). Effective elastic moduli of a particulate composite in terms of the dipole moments and property contribution tensors. *International Journal of Solids and Structures*, *53*, 1–11. http://doi.org/10.1016/j.ijsolstr.2014.10.032

Lind, P. G. (2009). Sequential random packings of spheres and ellipsoids. In *AIP Conference Proceedings* (Vol. 219, pp. 219–222). AIP. http://doi.org/10.1063/1.3179897

Lubachevsky, B. D., Stillinger, F. H., & Pinson, E. N. (1991). Disks vs. spheres: Contrasting properties of random packings. *Journal of Statistical Physics*, *64*(3-4), 501–524. http://doi.org/10.1007/BF01048304

Maxwell, J. C. (1873). *A Treatise on Electricity and Magnetism*. Oxford: Clarendon Press.

McCartney, L. N., & Kelly, A. (2008). Maxwell's far-field methodology applied to the prediction of properties of multi-phase isotropic particulate composites. *Proceedings of the Royal Society A: Mathematical, Physical and Engineering Sciences*, *464*(2090), 423–446. http://doi.org/10.1098/rspa.2007.0071

McMillan, P. F. (2003). Chemistry of materials under extreme high pressure-high-temperature conditions. *Chemical Communications*, 919–23. http://doi.org/10.1039/b300963g

Menon, S. K., & Martin, P. L. (1986). Determination of the anisotropy of surface free energy of fine metal particles. *Ultramicroscopy*, *20*(1-2), 93–98. http://doi.org/10.1016/0304-3991(86)90174-9

Miyazawa, T., Aratake, M., & Onaka, S. (2012). Superspherical-shape approximation to describe the morphology of small crystalline particles having near-polyhedral shapes with round edges. *Journal of Mathematical Chemistry*, *50*(1), 249–260. http://doi.org/10.1007/s10910-011-9909-1

Mogilevskaya, G., & Nikolskiy, D. V. (2015). The shape of Maxwell's equivalent inhomogeneityand "strange" properties of regular polygons and other symmetric domainss. *Quarterly Journal of Mechanics and Applied Mathematics*, *68*(4), 363–385. http://doi.org/10.1093/qjmam/hbv012

Mori, T., & Tanaka, K. (1973). Average stress in matrix and average energy of materials with misfitting inclusions. Acta Metall.

Moss, L. W., & Kobayashi, A. S. (1971). Approximate analysis of axisymmetric problems in fracture mechanics with application to a flat toroidal crack. *International Journal of Fracture Mechanics*, *7*(1), 89–99. http://doi.org/10.1007/BF00236485

Mossakovski, V. I., & Rybka, M. T. (1964). Generalization of the Griffith-Sneddon criterion for the case of a nonhomogeneous body. *PMM (translation of Applied Mathematics and Mechanics)*, *28*, 1061–1069.

Moulinec, H., & Suquet, P. (1998). A numerical method for computing the overall response of nonlinear composites with complex microstructure. *Computer Methods in Applied Mechanics and Engineering*, *157*(1-2), 69–94. http://doi.org/10.1016/S0045-7825(97)00218-1

Moulinec, H., & Suquet, P. M. (1994). A fast numerical method for computing the linear and nonlinear properties of composites. *Comptes Rendus de l'Académie Des Sciences. Série II, Mécanique, Physique, Chimie, Sciences de L'univers, Sciences de La Terre*, *318*(11), 1417–1423.

MSC Software. (2012). MSC Marc 2012 User Documentation. Volume A: Theory and User Information. Santa Ana, CA, USA.

Nied, H. F. (1981). *Circumferentially cracked cylinders under extension or bending*.

Nied, H. F., & Erdogan, F. (1983). The elasticity problem for a thick-walled cylinder containing a circumferential crack. *International Journal of Fracture*, *22*(4), 277–301. http://doi.org/10.1007/BF01140157

Niu, W., Zheng, S., Wang, D., Liu, X., Li, H., Han, S., … Xu, G. (2009). Selective synthesis of single-crystalline rhombic dodecahedral, octahedral, and cubic gold nanocrystals. *Journal of the American Chemical Society*, *131*(2), 697–703. http://doi.org/10.1021/ja804115r

Nozaki, H., & Taya, M. (2001). Elastic Fields in a Polyhedral Inclusion With Uniform Eigenstrains and Related Problems. *Journal of Applied Mechanics*, *68*(3), 441–452. http://doi.org/10.1115/1.1362670

Okabe, H., & Blunt, M. J. (2005). Pore space reconstruction using multiple-point statistics. *Journal of Petroleum Science and Engineering*, *46*(1-2), 121–137. http://doi.org/10.1016/j.petrol.2004.08.002

Onaka, S. (2001). Averaged Eshelby tensor and elastic strain energy of a superspherical inclusion with uniform eigenstrains. *Philosophical Magazine Letters*, *81*(4), 265–272. http://doi.org/10.1080/09500830010019031

Onaka, S. (2006). Simple equations giving shapes of various convex polyhedra: the regular polyhedra and polyhedra composed of crystallographically low-index planes. *Philosophical Magazine Letters*, *86*(3), 175–183. http://doi.org/10.1080/09500830600603050

Onaka, S. (2016). Extended Superspheres for Shape Approximation of Near Polyhedral Nanoparticles and a Measure of the Degree of Polyhedrality. *Nanomaterials*, *6*(2), 27. http://doi.org/10.3390/nano6020027

Onaka, S., Kobayashi, N., Fujii, T., & Kato, M. (2003). Energy analysis with a superspherical shape approximation on the spherical to cubical shape transitions of coherent precipitates in cubic materials. *Materials Science and Engineering A*, *347*(1-2), 42–49. http://doi.org/10.1016/S0921-5093(02)00559-2

Onaka, S., Sato, H., & Kato, M. (2002). Elastic states of doughnut-like inclusions with uniform eigenstrains treated by averaged Eshelby tensors. *Philosophical Magazine Letters*, *82*(1), 1–7. http://doi.org/10.1080/09500830110100642

Park, K. H., Jang, K., Kim, H. J., & Son, S. U. (2007). Near-monodisperse tetrahedral rhodium nanoparticles on charcoal: The shape-dependent catalytic hydrogenation of arenes. *Angewandte Chemie - International Edition*, *46*(7), 1152–1155. http://doi.org/10.1002/anie.200603961

Perram, J., & Wertheim, M. (1985). Statistical mechanics of hard ellipsoids. I. Overlap algorithm and the contact function. *Journal of Computational Physics*, *58*, 409–416.

Pierard, O., González, C., Segurado, J., LLorca, J., & Doghri, I. (2007). Micromechanics of elasto-plastic materials reinforced with ellipsoidal inclusions. *International Journal of Solids and Structures*, *44*(21), 6945–6962. http://doi.org/10.1016/j.ijsolstr.2007.03.019

Radi, E., & Sevostianov, I. (2016). Toroidal insulating inhomogeneity in an infinite space and related problems. *Proceedings of the Royal Society A: Mathematical, Physical and Engineering Sciences*, *472*(2187). http://doi.org/10.1098/rspa.2015.0781

Rasool, A., & Böhm, H. J. (2012). Effects of particle shape on the macroscopic and microscopic linear behaviors of particle reinforced composites. *International Journal of Engineering Science*, *58*, 21–34. http://doi.org/10.1016/j.ijengsci.2012.03.022

Rice, J. R. (1975). Continuum Mechanics and Thermodynamics of Plasticity and Relation to Microscale Deformation Mechanisms. *Chapter 2 of Constitutive Equations in Plasticity*, 23–79.

Rodin, G. (1996). Eshelby's inclusion problem for polygons and polyhedra. *Journal of the Mechanics and Physics of Solids*, *44*(12), 1977–1995.

Saxena, N., & Mavko, G. (2014). Exact equations for fluid and solid substitution. *Geophysics*, *79*(3). http://doi.org/10.1190/geo2013-0187.1

Segurado, J., & Llorca, J. (2002). A numerical approximation to the elastic properties of sphere-reinforced composites. *Journal of the Mechanics and Physics of Solids*, *50*(10), 2107–2121. http://doi.org/10.1016/S0022-5096(02)00021-2

Selvadurai, A. P. S., & Singh, B. M. (1985). The annular crack problem for an isotropic elastic solid. *Quarterly Journal of Mechanics and Applied Mathematics*, *38*(2), 233–243. http://doi.org/10.1093/qjmam/38.2.233

Seo, D., Ji, C. P., & Song, H. (2006). Polyhedral gold nanocrystals with Oh symmetry: From octahedra to cubes. *Journal of the American Chemical Society*, *128*(46), 14863–14870. http://doi.org/10.1021/ja062892u

Sevostianov, I. (2003). Explicit relations between elastic and conductive properties of materials containing annular cracks. *Philosophical Transactions. Series A, Mathematical, Physical, and Engineering Sciences*, *361*(1806), 987–999. http://doi.org/10.1098/rsta.2003.1176

Sevostianov, I. (2006). Thermal conductivity of a material containing cracks of arbitrary shape. *International Journal of Engineering Science*, *44*(8-9), 513–528. http://doi.org/10.1016/j.ijengsci.2006.04.001

Sevostianov, I. (2014). On the shape of effective inclusion in the Maxwell homogenization scheme for anisotropic elastic composites. *Mechanics of Materials*, *75*, 45–59. http://doi.org/10.1016/j.mechmat.2014.03.003

Sevostianov, I., Chen, F., Giraud, A., & Grgic, D. (2016). Compliance and resistivity contribution tensors of axisymmetric concave pores. *International Journal of Engineering Science*, *101*, 14–28. http://doi.org/10.1016/j.ijengsci.2015.12.005

Sevostianov, I., & Giraud, A. (2012). ON the compliance contribution tensor for a concave superspherical pore. *International Journal of Fracture*, *177*(2), 199–206. http://doi.org/10.1007/s10704-012-9754-7

Sevostianov, I., & Kachanov, M. (1999). Compliance tensors of ellipsoidal inclusions. *International Journal of Fracture*, *96*(1), 3–7. http://doi.org/10.1023/A:1018712913071

Sevostianov, I., & Kachanov, M. (2001). Elastic Compliance of an Annular Crack. *International Journal of Fracture*, *110*, L51–L54. http://doi.org/10.1017/CBO9781107415324.004

Sevostianov, I., & Kachanov, M. (2002a). Explicit cross-property correlations for anisotropic two-phase composite materials. *Journal of the Mechanics and Physics of Solids*, *50*(2), 253–282. http://doi.org/10.1016/S0022-5096(01)00051-5

Sevostianov, I., & Kachanov, M. (2002b). On elastic compliances of irregularly shaped cracks. *International Journal of Fracture*, *114*(3), 245–257. http://doi.org/10.1023/A:1015534127172

Sevostianov, I., & Kachanov, M. (2007). Relations between compliances of inhomogeneities having the same shape but different elastic constants. *International Journal of Engineering Science*, *45*(10), 797–806. http://doi.org/10.1016/j.ijengsci.2007.05.004

Sevostianov, I., & Kachanov, M. (2008). On approximate symmetries of the elastic properties and elliptic orthotropy. *International Journal of Engineering Science*, *46*(3), 211–223. http://doi.org/10.1016/j.ijengsci.2007.11.003

Sevostianov, I., & Kachanov, M. (2011). Elastic fields generated by inhomogeneities: Far-field asymptotics, its shape dependence and relation to the effective elastic properties. *International Journal of Solids and Structures*, *48*(16-17), 2340–2348. http://doi.org/10.1016/j.ijsolstr.2011.04.014

Sevostianov, I., & Kachanov, M. (2012). Is the concept of "average shape" legitimate, for a mixture of inclusions of diverse shapes? *International Journal of Solids and Structures*, *49*(23-24), 3242–3254. http://doi.org/10.1016/j.ijsolstr.2012.06.018

Sevostianov, I., & Kachanov, M. (2013). *Effective Properties of Heterogeneous Materials* (Vol. 193). http://doi.org/10.1007/978-94-007-4282-6

Sevostianov, I., Kachanov, M., & Drach, B. (2014). On the effect of interactions of inhomogeneities on the overall elastic and conductive properties. *International Journal of Solids and Structures*, *51*(25–26), 4531–4543. http://doi.org/http://dx.doi.org/10.1016/j.ijsolstr.2014.08.029

Sevostianov, I., Kachanov, M., & Zohdi, T. (2008). On computation of the compliance and stiffness contribution tensors of non ellipsoidal inhomogeneities. *International Journal of Solids and Structures*, *45*(16), 4375–4383. http://doi.org/10.1016/j.ijsolstr.2008.03.020

Shibuya, T., Nakahara, I., & T., K. (1975). The Axisymmetrie Distribution of Stresses in an Infinite Elastic Solid Containing a Flat Annular Crack under Internal Pressure. *ZAMM - Journal of Applied Mathematics and Mechanics / Zeitschrift Für Angewandte Mathematik Und Mechanik*, *55*, 395–402.

Smetanin, B. I. (1968). The problem of extension of an elastic space containing a plane annular slit. *Journal of Applied Mathematics and Mechanics / Zeitschrift Für Angewandte Mathematik Und Mechanik, 55*, 395–402.

Smith, P., & Torquato, S. (1988). Computer simulation results for the two-point probability function of composite media. *Journal of Computational Physics*, *76*(1), 176–191. http://doi.org/10.1016/0021-9991(88)90136-2

Song, C., Wang, P., & Makse, H. A. (2008). A phase diagram for jammed matter. *Nature*, *453*(7195), 629–632. http://doi.org/10.1038/nature06981

Sun, S., & Yang, Z. (2014). Recent advances in tuning crystal facets of polyhedral cuprous oxide architectures. *RSC Adv.*, *4*(8), 3804–3822. http://doi.org/10.1039/C3RA45445B

Sundquist, B. E. (1964). A direct determination of the anisotropy of the surface free energy of solid gold, silver, copper, nickel, and alpha and gamma iron. *Acta Metallurgica*, *12*(1), 67–86. http://doi.org/10.1016/0001-6160(64)90055-0

Suquet, P. M. (1987). *Elements of Homogenization Theory for Inelastic Solid Mechanics*. (E. Sanchez-Palencia & A. Zaoui, Eds.)*Homogenization Techniques for Composite Media*. Berlin: Springer–Verlag. http://doi.org/10.1007/3-540-17616-0_15

Todoroki, A., Kobayashi, H., & Nakumura, H. (1988). Effect of partial crack surface contact on fatigue crack growth in residual stress fields. *Proceedings of the Second International Conference on Residual Stresses, Nancy, France*, 84–89.

Torquato, S. (1998). Effective stiffness tensor of composite media : II. Applications to isotropic dispersions. *Journal of the Mechanics and Physics of Solids*, *46*(8), 1411–1440. http://doi.org/10.1016/S0022-5096(97)00083-5

Torquato, S., & Stell, G. (1982). Microstructure of two-phase random media. I. The n-point probability functions. *The Journal of Chemical Physics*, *77*(4), 2071. http://doi.org/10.1063/1.444011

Tsukrov, I., & Novak, J. (2002). Effective elastic properties of solids with defects of irregular shapes. *International Journal of Solids and Structures*, *39*(6), 1539–1555. http://doi.org/10.1016/S0020-7683(01)00285-2

Tsukrov, I., & Novak, J. (2004). Effective elastic properties of solids with two-dimensional inclusions of irregular shapes. *International Journal of Solids and Structures*, *41*(24-25), 6905–6924. http://doi.org/10.1016/j.ijsolstr.2004.05.037

Walpole, L. J. (1969). On the overall elastic moduli of composite materials. *Journal of the Mechanics and Physics of Solids*, *17*(4), 235–251. http://doi.org/10.1016/0022-5096(69)90014-3

Wang, Z. L. (2000). Transmission Electron Microscopy of Shape-Controlled Nanocrystals and Their Assemblies. *The Journal of Physical Chemistry B*, *104*(6), 1153–1175. http://doi.org/10.1021/jp993593c

Weng, G. J. (1990). The theoretical connection between Mori-Tanaka's theory and the Hashin-Shtrikman-Walpole bounds. *International Journal of Engineering Science*, *28*(11), 1111–1120. http://doi.org/10.1016/0020-7225(90)90111-U

Weng, G. J. (2010). A dynamical theory for the Mori-Tanaka and Ponte Castaneda-Willis estimates. *Mechanics of Materials*, *42*, 886–893. http://doi.org/10.1016/j.mechmat.2010.06.004

Widom, B. (1966). Random Sequential Addition of Hard Spheres to a Volume. *The Journal of Chemical Physics*, *44*(10), 3888. http://doi.org/10.1063/1.1726548

Wu, L., & Du, S. (1995). The Elastic Field Caused by a Circular Cylindrical Inclusion. *Journal of Applied Mechanics*, *62*(3), 579–584.

Wu, T. Te. (1966). The effect of inclusion shape on the elastic moduli of a two-phase material. *International Journal of Solids and Structures*, *2*(1), 1–8. http://doi.org/http://dx.doi.org/10.1016/0020-7683(66)90002-3

Zeon Han, S., Kim, K. H., Kang, J., Joh, H., Kim, S. M., Ahn, J. H., … Han, B. (2015). Design of exceptionally strong and conductive Cu alloys beyond the conventional speculation via the interfacial energy-controlled dispersion of γ-Al2O3 nanoparticles. *Scientific Reports*, *5*(October), 17364. http://doi.org/10.1038/srep17364

Zimmerman, R. W. (1986). Compressibility of Two-Dimensional Cavities of Various Shapes. *Journal of Applied Mechanics*, *53*(3), 500–504. http://doi.org/10.1115/1.3171802

Zimmerman, R. W. (1991). *Compressibility of Sandstones*. Elsevier.

Zimmermann, E. A., Busse, B., & Ritchie, R. O. (2015). The fracture mechanics of human bone: influence of disease and treatment. *BoneKEy Reports*, *4*(SEPTEMBER), 743. http://doi.org/10.1038/bonekey.2015.112

Zohdi, T. I. (2012). On the relationship between the H-tensor and the concentration tensor and their bounds. *International Journal of Fracture*, *177*(1), 89–95. http://doi.org/10.1007/s10704-012-9749-4

Zou, W., He, Q., Huang, M., & Zheng, Q.-S. (2010). Eshelby's problem of non-elliptical inclusions. *Journal of the Mechanics and Physics of Solids*, *58*(3), 346–372. http://doi.org/10.1016/j.jmps.2009.11.008